

# A Macaque Model of Motor Neurone Disease

*Rachael Heather Anne Jones*

Thesis submitted for the degree of  
*Doctor of Philosophy*

Institute of Biosciences  
Faculty of Medical Sciences  
Newcastle University

Supervisors:

Prof Stuart Baker

Dr Mark Baker

May 2022



## Abstract

Motor Neurone Disease (MND) is a rapidly progressive and ultimately fatal neurodegenerative disease, characterised by the loss of upper and lower motor neurons. The primary proteinopathy found in approximately 97% of all cases involves cytoplasmic mislocalisation and aggregation of the ubiquitous nuclear protein, TDP-43. Despite the identification of many implicated genes during the last few decades, our understanding of the mechanisms involved in the onset and propagation of pathology have advanced very little.

Translatable advancements have likely been limited due a lack of reliable animal models which accurately recapitulate this complex disorder. No model has been created to date which replicates the progressive motor weakness; characteristic histopathologies; extended pre-symptomatic phase and subsequent rapid deterioration. Rodents have been the dominant species in MND research; however, their anatomy and genetic profile differs fundamentally to humans. Crucially, they lack the direct monosynaptic connection between the upper and lower motor neurons, unique to primates.

We have harnessed a novel intersectional genetics approach to induce the overexpression of the human TDP-43 protein in a selective spinal motoneuron population in two Rhesus macaques. This caused to a focal denervation event in the targeted muscle, followed by signs of ongoing denervation and reinnervation in other muscles. *In vivo* monitoring techniques were selected based on their clinical applications and their ease of use and adaptation for primate research. Comparable sequences of change were detected using MRI, EMG and nerve stimulation, providing compelling evidence for a shared MND-like pathogenesis occurring in both animals.

Focal overexpression of TDP-43 in a spinal motor pool was sufficient to induce the expression of pathological phosphorylated TDP-43 throughout the cervical spine and motor cortex. The detection of this histopathology in the distant giant cells of Betz in the primary motor cortex supports the idea of an axon mediated ‘prion-like’ spread, likely involving the corticospinal tract.

*For Malibu and Midori*

## Acknowledgements

This work presented in this thesis would not have been possible without the help, support and encouragement of a number of people. Firstly, I would like to thank my supervisors Stuart Baker and Mark Baker, for their unrelenting optimism and enthusiasm. I am very grateful to have worked with them on such an interesting and rewarding project.

I would also like to extend my gratitude to my funders, The William Leech Charity, for their exceptional generosity. This project would not have been possible without the inspired late Roy Leech, and the continuing support of Richard Leech and the trustees.

This project would not have been possible without the unwavering support from the CBC technical and veterinary staff and tireless commitment of the BakerLab ‘Monkey people’. Special mentions must go to Terri Jackson and Andrew Atkinson, who the lab could not function without; and Norman Charlton and Nathan Cassie for their engineering innovations. Thank to Annie Poll for the regular sanity checks and teaching me the way of the post-doc.

I would also like to acknowledge the wider members of the motor group and ‘cheese and wine’ community who have been wonderful colleagues and friends during this experience, never short of MATLAB advice or time for a quick North Terrace trip.

I would like to thank Alessandro del Vecchio, who it has been a pleasure to collaborate with and learn from. Within Newcastle, huge thanks go to Fabien Balezeau and Ian Schofield for their help in the design and day to day running of the MRI scanning protocols, and to Fabien in particular for helping me to hit the ground running with the analysis. I must also thank the histology lab users, with special mentions to Gavin Clowry for his endless tips and tricks, Dominic Simpson for his support and encouragement in my early lab days, and Caroline McCardle for her relentless positivity in the face of elusive antibody labelling.

I hope my friends and family accept this thesis as my apology for the cancelled plans and unreturned calls. I am extremely grateful for their support and encouragement of everything I strive to achieve. My final thank you goes to my wonderful boyfriend, Oscar, for keeping me so well fed in my time of need.

Lastly, I would like to pay my respects to the two animals involved in this project, both of whom made the last few years such a rewarding experience. I feel very grateful to have shared such a bond with them.

# Contents

Abstract.....	i
Acknowledgements.....	iii
List of figures.....	viii
Abbreviations.....	ix
Publications.....	xi
Papers.....	xi
Abstracts – Poster presentations.....	xi
CHAPTER I. Introduction.....	1
Motor Neurone Disease.....	1
Clinical features and diagnosis.....	1
Aetiology.....	3
Proteinopathies.....	3
Mechanism of spread.....	4
Frontotemporal Lobar Degeneration.....	5
Animal models of MND.....	5
Viral transfection.....	6
TDP-43 Expressing Models.....	8
Thesis Objective.....	9
CHAPTER II. General Methods.....	11
Animals.....	11
Surgical Preparation.....	11
Behavioural Task.....	12
In vivo assessments.....	13
Virus injection.....	13
Post-mortem assessment.....	15
CHAPTER III. Application of Magnetic Resonance Imaging to Identify Onset of Viral Vector Mediated Spinal Motoneuron Loss in a Non-Human Primate Model of MND.....	16
Introduction.....	16
Methods.....	20
Animals.....	20
MRI acclimatisation.....	20
Structural MRI.....	20

Post processing .....	21
Analysis of signal intensity.....	21
Results .....	23
MRI signal intensity .....	23
Discussion .....	30
Methodological considerations.....	30
Differences between the two animals.....	31
Source of signal change.....	32
CHAPTER IV. Investigating Limb-wide Changes in Voluntary EMG Following a TDP-43 Overexpression Event in a Focal Spinal Motor Pool in Two NHPs.....	34
Introduction .....	34
Methods.....	37
Animals.....	37
Electrophysiological Recordings.....	37
Task Analysis .....	37
Results .....	40
Discussion .....	51
CHAPTER V. Validation of <i>in vivo</i> Measures of the Health of Spinal Motoneurons in NHPs .....	55
Introduction .....	55
Methods.....	59
Animals.....	59
Electrophysiological Recordings.....	59
Nerve cuff stimulation and recording.....	60
Compound Muscle Action Potential (CMAP).....	60
Motor unit decomposition .....	61
Motor unit number estimation (MUNE).....	61
Statistical analysis.....	62
Results .....	63
Compound Muscle Action Potential (CMAP).....	63
Motor unit number estimation (MUNE).....	72
Discussion .....	83
CHAPTER VI. Histopathological Changes in the Spinal Cord of a NHP Model of MND ....	88
Introduction .....	88

Methods.....	91
Animals.....	91
Immunohistochemistry .....	91
Fluorescent viral tag .....	91
Functional TDP-43 .....	92
Phosphorylated TDP-43 .....	92
Motoneuron labelling .....	93
Microscopy and Quantification .....	94
Statistical analysis.....	94
Results .....	95
Viral Tag.....	95
Evidence of Motoneuron Loss.....	95
TDP-43 .....	98
Discussion .....	103
Detection of transfected motoneurons.....	103
Degeneration of spinal cord MNs.....	103
TDP-43 pathology is widespread throughout the cervical spinal cord.....	104
CHAPTER VII. Histopathological Changes in the Primary Motor Cortex of a NHP Model of MND .....	108
Introduction .....	108
Methods.....	112
Animals.....	112
Immunohistochemistry .....	112
Functional TDP-43 .....	112
Phosphorylated TDP-43 .....	113
Neuron labelling .....	113
Microscopy and Quantification .....	114
Statistical analysis.....	114
Results .....	115
Discussion .....	121
CHAPTER VIII. General Discussion .....	124
MRI.....	125
Electromyography .....	126
Nerve stimulation .....	126

Histopathology .....	127
Time course of severity .....	129
Future Directions.....	131
References.....	133

## List of figures

Figure 2.1. Virus Injections .....	14
Figure 3.1 T2 scans and nerve regeneration .....	18
Figure 3.2 MRI set up .....	22
Figure 3.3 MRI RARE scans .....	24
Figure 3.4 Monkey Mi signal change .....	26
Figure 3.5 Monkey Ma signal change.....	27
Figure 3.6 Conserved spatiotemporal spread of signal.....	29
Figure 4.1 Task set up.....	42
Figure 4.2 Monkey Mi RHS EMG changes .....	43
Figure 4.3 Monkey Ma RHS EMG Changes .....	47
Figure 4.4 Monkey Ma LHS EMG changes .....	48
Figure 4.5 Conserved pattern of EMG reduction.....	49
Figure 5.1 Collecting CMAP scans .....	64
Figure 5.2 Monkey Mi R-BR CMAP scan steps .....	65
Figure 5.3 Monkey Mi RHS CMAP amplitude.....	67
Figure 5.4 Monkey Mi LHS CMAP amplitude .....	68
Figure 5.5 Monkey Ma RHS CMAP amplitude .....	70
Figure 5.6 Monkey Ma LHS CMAP amplitude.....	71
Figure 5.7 MUAPs.....	73
Figure 5.8 Monkey Mi RHS MUNE.....	76
Figure 5.9 Monkey Ma RHS MUNE.....	79
Figure 5.10 Monkey Ma LHS MUNE .....	82
Figure 6.1 Loss of MNs .....	97
Figure 6.2 Spinal TDP-43 pathology .....	100
Figure 6.3 Spinal pTDP-43 pathology .....	101
Figure 6.4 pTDP-43+ MN counts .....	102
Figure 7.1 M1 TDP-43 pathology.....	117
Figure 7.2 M1 pTDP-43 pathology.....	118
Figure 7.3 pTDP43+ Betz cell counts.....	119

## Abbreviations

<b>1DI</b>	First dorsal interosseous
<b>AAV</b>	Adeno-associated virus
<b>ACh</b>	Acetylcholine
<b>ADM</b>	Abductor digiti minimi
<b>APB</b>	Abductor pollicis brevis
<b>AV</b>	Adenovirus
<b>BH</b>	Benjamini Hochberg
<b>BR</b>	Brachioradialis
<b>ChAT</b>	Choline acetyl transferase
<b>CM</b>	Corticomotoneuron
<b>CMAP</b>	Compound muscle action potential
<b>CSF</b>	Cerebrospinal fluid
<b>CST</b>	corticospinal tract
<b>ECR</b>	Extensor carpi radialis
<b>EDC</b>	Extensor digitorum communis
<b>EMG</b>	Electromyography
<b>FCR</b>	Flexor carpi radialis
<b>FDS</b>	Flexor digitorum superficialis
<b>FTLD</b>	Frontotemporal lobar degeneration
<b>FUS</b>	Fused in sarcoma
<b>HD-sEMG</b>	High-density surface EMG
<b>ICT</b>	Incremental counting technique
<b>LMN</b>	Lower motor neuron
<b>M1</b>	Primary motor cortex
<b>MN</b>	$\alpha$ -motoneuron
<b>MND</b>	Motor Neurone Disease (also Amyotrophic Lateral Sclerosis)
<b>MPS</b>	Multiple point stimulation
<b>MRI</b>	Magnetic resonance imaging
<b>MU</b>	Motor unit
<b>MUAP</b>	Motor unit action potential
<b>MUNE</b>	Motor unit number estimation

<b>MUNIX</b>	Motor unit number index
<b>NCS</b>	Nerve conduction studies
<b>NHP</b>	Non-human primate
<b>pTDP-43</b>	Phosphorylated TDP-43
<b>RARE</b>	Rapid acquisition with relaxation enhancement
<b>RF</b>	Radiofrequency
<b>SOD1</b>	Superoxide Dismutase 1
<b>STIR</b>	Short tau inversion recovery
<b>TDP-43</b>	Trans-active response DNA-binding protein 43
<b>UMN</b>	Upper motor neuron

## Publications

### *Papers*

DEL VECCHIO, A., **JONES, R. H. A.**, SCHOFIELD, I. S., KINFE, T. M., IBÁÑEZ, J., FARINA, D. & BAKER, S. N. 2021. Interfacing Spinal Motor Units in Non-Human Primates Identifies a Principal Neural Component for Force Control Constrained by the Size Principle. *bioRxiv*, 2021.12.07.471592. (in review, *JNeurosci*)

### *Abstracts – Poster presentations*

**Jones, RHA** & Baker, SN. Neurochemical and morphological classification of the pontomedullary reticular formation in Rhesus Macaques. *Society for Neuroscience*, Chicago, 2019.

# CHAPTER I. Introduction

## Motor Neurone Disease

### *Clinical features and diagnosis*

Motor neurone disease (MND) is a rapidly progressive and devastating, adult-onset, neurodegenerative disorder affecting around 2 in 100,000 people in the UK (Alonso et al., 2009). Over 90% of cases occur sporadically in patients with no family history of the disease (Gao et al., 2018). There are variable presentations of MND which originate in different focal sites, however the predominant form of the disease is primarily characterised by the degeneration of both upper motor neurons of the motor cortex, otherwise known as corticomotoneuronal (CM) cells, and  $\alpha$ -motoneurons (MNs) of the spinal cord and bulbar cranial nerve nuclei, referred to clinically as lower motor neurons (Ragagnin et al., 2019). For patients diagnosed with this form of MND, mean life expectancy is reduced to 2-3 years from the first onset of symptoms (Rowland and Shneider, 2001). The clinical features of MND include motor weakness and muscle atrophy, without sensory disturbance, with heterogeneous progression. Despite the disparities in disease presentation and development between patients diagnosed with different focal sites of onset, relatively conserved patterns of muscle weakness have been detected, and are often related to sites of pathological inclusions (Brettschneider et al., 2013, Ludolph et al., 2020). Cognitive impairments are also commonly seen alongside MND, with a sub-set of patients developing frontotemporal lobar degeneration (Strong et al., 2017).

While many genes and proteins implicated in MND have been identified over the last couple of decades, there have been no real breakthroughs in terms of treatment. The only pharmacological agent thought to affect and slow disease progression, currently available on the NHS is Riluzole (Bensimon et al., 1994). This drug is primarily thought to act as a glutamate antagonist, and thus a neuroprotective agent against excitotoxicity (Cheah et al., 2010, Cifra et al., 2011). Analysis of the original trial data found Riluzole to have a limited impact on the rate of disease progression, increasing life expectancy of patients by an average of three months, and without any real effect on symptom severity (Bensimon et al., 1994, Miller et al., 2007). Recent retrospective analysis of clinical trials has in fact suggested that this drug acts mainly in lengthening the late stage of the disease rather than slowing the overall time course of disease progression (Fang et al., 2018), although it has

since been postulated that the therapeutic benefits of Riluzole may depend on the stage of disease at which it is administered (Geevasinga et al., 2016).

Due to an absence of effective and reliable biomarkers of the disease and methods in which to record them, most diagnoses are made by clinical examination and application of the El Escorial criteria with Gold Coast revision (Shefner et al., 2020). The lack of biomarkers often leads to a delay in diagnosis and exclusion of patients from clinical trials. Electrophysiological techniques, such as electromyography (EMG) and nerve conduction studies (NCS) are currently used to facilitate diagnosis and exclude other diseases. Motor unit number index (MUNIX) and estimation (MUNE) assessments approximate the number and size of motor units in a muscle and can be used as an indicator of lower motor neuron health. Needle EMG recordings, with or without ultrasound, can be used to detect spontaneous discharges from the muscles, known as fasciculation potentials, which are a common feature of MND and demonstrate ongoing denervation (Joyce and Carter, 2013, Tsugawa et al., 2018). These techniques provide supportive evidence for diagnosis rather than the diagnosis itself, and do not consider the role of upper motor neuron degeneration. The loss of intramuscular beta-band coherence, detected using EMG, has been proposed as a marker for upper motor neuron health, however further validation is required (Fisher et al., 2012). In addition to these electrophysiological methods, neuroimaging techniques are gaining popularity. A great deal of effort has been put into developing these and other related techniques due to their potential as objective markers of therapeutic success in clinical trials.

Magnetic resonance imaging (MRI), while usually limited to discounting other disease pathology, is increasingly utilised to detect changes in signal intensity in the cortex and corticospinal tract (CST) using diffusion tensor imaging, thought to reflect changes in the tissue organisation (Ciccarelli et al., 2006). Structural differences in the motor cortices recorded by MRI have also been used to distinguish MND patients from healthy controls (Ferraro et al., 2017). T2-weighted changes, which detect fluid alterations, in this case thought to be representative of denervation, have also been used to characterise changes in the musculature of MND patients (Kamath et al., 2008). These scans have been applied in longitudinal studies alongside MUNIX analysis and have identified that muscle T2 signal becomes enhanced progressively alongside muscle weakness and reductions in MUNIX values (Jenkins et al., 2020).

## ***Aetiology***

The genetic aetiology of MND is yet to be fully elucidated. The genetic contribution to the familial MND cases, which are thought to make up approximately 10% of all cases, is much better understood than that of the sporadic cases. Of the familial cases, 40% are due to hexanucleotide repeat expansions of the *C9orf72* gene. The normal function of this gene and how its mutation leads to such disastrous neurodegenerative conditions is yet to be fully elucidated, however, it is thought that these repeat expansions may interfere in some way with RNA processing and metabolism (Renton et al., 2014). The *C9orf72* ‘pathogenic expansions’ have also been found to account for ~7% of sporadic MND cases and ~25% of familial FTLD cases, providing the first clear genetic link between the two commonly co-occurring disorders (Lomen-Hoerth et al., 2002, Renton et al., 2011, Majounie et al., 2012). The second most common genetic cause of familial MND relate to mutations of the gene encoding the protein SOD1 (Rosen et al., 1993, Shaw et al., 1997). These mutations were the first to be identified and linked to the onset of MND, and account for 20% of familial and 3% of sporadic cases. This discovery led to many transgenic rodent studies, however in recent years it has become clear that SOD1-MND is separate in its pathology and severity from other MND varieties (Mackenzie et al., 2007). For example, this subtype lacks the distinctive TDP-43 pathology seen in the majority of MND cases. Other mutations, such as of the *TARDBP* and *FUS* gene, while accounting for only 2-5% and 4% of familial cases respectively, demonstrate the importance of RNA metabolism control in the maintenance of neurons (Sreedharan et al., 2008, Yokoseki et al., 2008, Vance et al., 2009, Kwiatkowski et al., 2009). Both genes encode RNA binding proteins located primarily in the nuclear compartment; TAR DNA-binding protein 43 (TDP-43) and the fused in sarcoma (FUS) protein.

## ***Proteinopathies***

Misfolded, protein-rich inclusions which spread in characteristic patterns throughout particular neuronal populations are a molecular hallmark of neurodegenerative disorders. The most common MND proteinopathy, found in approximately 97% of all cases, sporadic and familial, involves TDP-43, a highly conserved DNA and RNA binding protein involved in transcription, pre-mRNA splicing and translation control (Buratti and Baralle, 2008). Other proteins, for example SOD1 and FUS, have been implicated to a lesser extent, and primarily in familial cases in which the genes encoding these proteins have mutated. In the disease state, TDP-43 is lost from the nucleus and becomes mislocalised in the cytoplasm

of upper and lower motor neurons, as well as in neurons and occasionally glial cells within the frontal and temporal cortices, where it forms into aggregates (Arai et al., 2006, Neumann et al., 2006). These aggregates have been shown to be made up of hyperphosphorylated TDP-43 (pTDP-43) (Inukai et al., 2008). The histopathology and disease symptoms seem to spread between functionally connected regions rather than directly connected, neighbouring regions.

Interestingly, the presentation of pathology differs between the two primarily involved cell types. The large  $\alpha$ -MNs present with obvious cytoplasmic mislocalisation of TDP-43, followed by the formation of pTDP-43 skein-like and dense aggregates (Neumann et al., 2009). Conversely, within the CM cells, comprising giant cells of Betz and smaller pyramidal cells alike, pathology is more likely to present as sequestering of TDP-43 away from the nucleus, without the appearance of dense cytoplasmic pTDP-43 aggregates (Braak et al., 2017). In fact, the pathology is thought to be primarily exhibited in the long descending axons of these cells (Fallini et al., 2012).

### ***Mechanism of spread***

The question remains of how these proteinopathies spread between the affected cells. One theory to explain this phenomenon is a prion-like transmission of the pathological protein. This phenomena of self-sustaining aggregation and spreading of disease state proteins is thought to be a common feature of the histopathologies of many of the most common neurodegenerative diseases (Kanouchi et al., 2012). Along with determining how the disease spreads between cells, there is also the question of in which direction it spreads. There are three main theories regarding this, referred to as the ‘dying forward,’ ‘dying backward’ and ‘dying outward’ hypotheses. These hypotheses suggest that MND begins in the cortex and moves down, recruiting the lower motor neurons of the spinal cord, the opposite or an integration of the previous two hypotheses respectively. Other theories have been proposed which suggest a key role of the peripheral muscles and neuromuscular junction (Fischer et al., 2004).

There is a major body of evidence supporting a corticofugal model of spread, which directly implicates the long axons of the corticospinal and corticobulbar tracts in the propagation of MND pathology. The direct synapse between the CM cells of the motor cortex and spinal and bulbar  $\alpha$ -MNs has long been thought to play a key role in the dissemination of pathology. This theory is supported by the identification of pTDP-43 pathology in these

distinct and remote neural populations in the first pathological ‘stage’ of disease, identified in post-mortem tissue samples by Brettschneider et al. (2013). Additionally, characteristic sequences of muscle weakness are often observed in patients with similar MND presentations, in which the muscles with the strongest CM inputs are disproportionately affected (Weber et al., 2000, Khalaf et al., 2019, Ludolph et al., 2020). This model is consistent with the functional sparing of the extraocular muscles, as the oculomotor motoneurons receive only indirect cortical input (Horn and Leigh, 2011, Iwatsubo et al., 1990). This theory of trans-synaptic spread mediated by the CM axons does not account for the independent level of degeneration which has been recorded to occur in the upper and lower motor neuronal populations (Kiernan and Hudson, 1991). It is therefore unlikely that one model of spread can account for all MND phenotypes, but rather that multiple pathways are involved simultaneously.

### ***Frontotemporal Lobar Degeneration***

MND and FTLN have long been linked. 50% of MND patients go on to exhibit cognitive and behavioural impairments during the course of the disease, and 15% of patients with MND are also diagnosed with FTLN. In these patients, FTLN can be either the primary or secondary disorder of the two to be diagnosed. FTLN, a condition associated with degeneration of neurons and glia within the frontal and temporal lobes, classically manifests as a progressive dementia exhibiting mainly behavioural changes and aphasia. Both diseases are predominantly classified as displaying pTDP-43 pathology, albeit in distinct cortical neuronal populations, and both disorders have been highly linked to mutations in the *C9orf72* gene (Cairns et al., 2007, DeJesus-Hernandez et al., 2011). It has therefore been accepted for some time that these diseases exist at either end of a spectrum.

### **Animal models of MND**

Animal models of disease allow a unique opportunity to study the progression of disease pathogenesis from a spatially and temporally controlled epicentre. Models of MND may aid in the discovery of disease biomarkers, and be used for the development of future diagnostic tools and pharmaceutical interventions. These developments require a suitable model animal which recapitulates as closely as possible the unique pathology and phenotype associated with the disease. Genetic profile and anatomy play an important role in the selection of the model animal, as without conserved gene expression or the correct anatomical pathways, there is less guarantee of transferability of results.

In order to investigate MND pathogenesis and test novel treatments and applications, an effective and reliable animal model of the condition is required. The majority of current studies use rodents as their model animal, however the rodent motor system differs fundamentally from that of humans. Their lack of direct, monosynaptic connection between upper and lower motor neurons in the cortex and spinal cord in fact make rodents very poor models of this complex condition. In addition, the majority of historic MND models are derived from mutant mouse lines overexpressing SOD1 to different degrees. As in patients with SOD1 mutations, the transgenic mice display a phenotype devoid of TDP-43 proteinopathies and with little evidence of cortical motor neuron involvement (Deng et al., 2006, Ozdinler et al., 2011). These factors have likely contributed to the lack of translatable interventions derived from rodent models.

In an effort to better recapitulate the overarching disease pathology, mouse models involving the overexpression or knockout of TDP-43 can be used. Conditional overexpression is often implemented due to known issues with embryonic lethality, and can be used to temporally limit gene expression with the use of flox sites, or to limit the expression to regions targeted in disease by the action of specific promoters, such as the Prion Promotor (PrP) (Kraemer et al., 2010, Xu et al., 2010). Mice overexpressing human wild-type TDP-43 develop pTDP-43 ubiquitinated aggregates in the cytoplasm, progressive weakness in their limbs in combination and also loss of both spinal motoneurons and CST axons (Wegorzewska et al., 2009, Wils et al., 2010). While these models recapitulate many aspects of the pathophysiology, in most cases they do not replicate the presymptomatic phase, or gradual progression of symptoms due to the commonly aggressive phenotypes presented in these models.

## **Viral transfection**

Altering gene expression in NHPs is a less straight forward task than in rodents. On-going developments in viral vector technology provide the opportunity to control gene expression in select neuronal sub-populations, study neuronal connectivity and show increasing promise in clinical gene therapies. Adeno-associated viruses (AAVs) in particular have a number of features which make them ideal candidates for such uses. While other viruses, such as herpes simplex virus (HSV) and rabies virus (RABV) have clear applications in mapping of neuronal circuitry due to their ability to replicate and transfer between cells trans-synaptically, the AAVs are unable to replicate without the addition of a ‘helper virus’, for example an adenovirus (AV). AAVs present an ideal option for controlled and focal

transfection, as they induce gene expression in only the initially infected cells. These viruses have also been shown to be relatively stable long-term, causing less immunoreactivity than other viral vectors. For these reasons AAVs are often the first choice in clinical trials.

Eleven natural AAV serotypes have been discovered, each displaying different levels of neuronal tropism and transduction efficacy. Recombinant AAVs have been created by altering the AAV capsid proteins, merging select features of more than one serotype to modify and enhance tropism and transduction. This process is referred to as pseudotyping, and has been used to create vectors such as rAAV2, the most commonly used recombinant AAV. In addition to individual tropisms, different serotypes are predisposed to favour either retrograde or anterograde axonal transport (Salegio et al., 2013, San Sebastian et al., 2013). Anterograde transduction tends to be favoured by AAVs, however this can be overcome with the use of complementary promoters to enhance transportation at sites such as the axonal terminals or synapses (Li et al., 2018, Kugler et al., 2003). Additionally, the rAAV2 capsid gene has been specifically modified to produce rAAV2-retro with enhanced retrograde transmission capabilities (Tervo et al., 2016).

Further selectivity and efficacy of cell transfection can be controlled by the site of the AAV injections. The most classically effective methods of delivery into target neurons involve invasive measures, such as intracerebral and intrathecal injections directly into the brain or spinal cord. Intravenous administration is also commonly used, especially with the AAV9 serotype, known to cross the blood brain barrier (Duque et al., 2009). These methods in and of themselves often lead to widespread transgene expression throughout the CNS, rather than within a targeted cell population. Again, promoters aid with selectivity however these are often not sufficient to prevent gene expression in undesired locations (Bevan et al., 2011, Samaranch et al., 2012). Intramuscular delivery of AAVs has been used to target the subset of spinal MNs innervating the transfected muscles in non-human primates (Toromanoff et al., 2008, Towne et al., 2010). This technique also has its limitations, with evidence of gene expression in the injected muscle and viral particles transported away from the injection site to the liver. Promoters, such as the neuron-specific promoter hSyn, can be used to restrict transgene expression to the targeted neuronal population (Song et al., 2002, Greig et al., 2014). Furthermore, the injection site within the muscle can aid the preferential transduction of spinal MNs over myocytes. Tosolini and Morris (2016) found

that injecting the virus at the motor end plates greatly improved spinal MN transduction. If suitably performed, IM delivery may present the gold standard for spinal MN targeting.

Our own preliminary studies (unpublished) have demonstrated that intramuscular administration of various AAVs (rAAV2-retro, AAV6, AAV8 and AAV9) does not provide robust or reliable transgene expression in spinal motoneuron pools of non-human primates, with only a limited number of transfected cells identified in the few successful efforts. These issues are likely explained by insufficient concentrations of viral particles per kg of the animal's weight (Jackson et al., 2015), and well documented local immune response and subsequent formation of neutralising antibodies following intramuscular administration of AAVs (Chirmule et al., 2000, Song et al., 2002). These two limitations often combine, as higher vector doses are associated with increased immune responses (Arruda et al., 2004). Higher doses are better tolerated with intrathecal injections, which lead to extensive transfection throughout the CNS (Gray et al., 2013).

Multiple viruses utilising recombination enzymes can be used in combination to increase efficiency of gene transduction while maintaining the specificity of transfection site. The cre-loxP recombination system is an example of this inducible, site-specific recombination. The FLEx switch tool operates this system to trigger inversion and excision of the DNA sequence between the specific lox sites in the presence of Cre recombinase, allowing for its transcription. This tool can be incorporated into two viral vectors, confining the expression of the gene of interest to cells that contain the anti-sense DNA sequence, flanked by lox sites, from the first virus and the site specific recombinase from the second (Saunders et al., 2012). A similar dual virus technique has been used to elucidate propriospinal contributions to dextrous hand movements in macaques by selectively targeting and reversibly blocking the propriospinal neurons (Kinoshita et al., 2012).

### ***TDP-43 Expressing Models***

AAV mediated gene transfer has been previously implemented, with varying outcomes, to create non-human primate models of MND. To date, these models have been created with the overexpression of wild type human TDP-43 throughout the CNS following widespread intrathecal or intravenous administration of either the AAV1 or AAV9 serotypes. Replicating the protocol for TDP-43 overexpression in rats, Jackson et al. (2015) induced mild dose-dependent motor deficits and cytoplasmic TDP-43 histopathology in neonatal macaques. This model however, lacked any evidence of neuronal degeneration and no

discernible muscle wasting, as was present in the rodent model (Wang et al., 2010). Aberrant pTDP-43 was not inspected in this NHP model, however expression of other histopathological markers, such as p62 or ubiquitin, were identified in the spinal cord MNs. The authors of this study have proposed that a higher dose is required in order to enhance gene expression to clinically relevant levels.

A further group have succeeded in recapitulating the classical MND phenotype in adult macaques following intrathecal administration of the viral vector. These animals display progressive muscle weakness, with onset in the distal muscles of the hand, electrophysiological changes such as fasciculation potentials and also cytoplasmic pTDP-43 inclusions (Uchida et al., 2012). This model demonstrates that an over-expression of TDP-43 throughout the CNS is sufficient to produce system-wide MND-like symptoms and pathology. The widespread viral transduction and corresponding gene expression prevents investigation of the role of TDP-43 in the disease pathogenesis, as the progressive decline could be due to spread of virus rather than intrinsic spreading of pathology. Muscles from both the ipsi- and contralateral upper limbs displayed significant wasting 4 weeks after the virus injections and the animals were ultimately terminated no later than 7 weeks after the virus injections, at which point complete muscle paralysis had been recorded in the hand muscles of a subset of the animals. This rapid progression does not replicate the pre-symptomatic phase of the disease and additionally prevents the application and trialling of longitudinal measures in this model.

## **Thesis Objective**

The aim of this thesis was to develop a novel non-human primate model of MND in which to study the involvement of the ubiquitously expressed protein, TDP-43, in the propagation of neuropathology from a focal spinal motor pool.

Building on previously developed models, but with the application of dual virus recombination technology, we investigated the local and system-wide effects of a focal TDP-43 overexpression event. Using one virus, carrying Cre recombinase, to target spinal motoneurons throughout the rostrocaudal axis of the spinal cord, and a second retrograde virus administered intramuscularly, transduction could theoretically be limited to an individual motor pool. Temporally and spatially controlled transfection allowed us to track and characterise any progressive changes in the virus targeted muscle, as well as in neighbouring and functionally connected muscles within the ipsi- and contralateral limb.

The generation of this model enabled the assessment and validation of *in vivo* measures, such as MR imaging and electrophysiology, for the detection and tracking of virus mediated degeneration and denervation. Simultaneously, these techniques were used to appraise the validity of the model.

The detection of abnormal TDP-43 expression, alongside the presence of a fluorescent viral marker, in a subset of spinal MNs would be taken to indicate successful transfection, and the detection of TDP-43 proteinopathies, and the locations within which they were found indicated the propagation potential of this protein. For example, pTDP-43 limited to the transfected motor pool would demonstrate the occurrence of a local pathological event, whereas pTDP-43 in additional motor pools, and possibly cortical neurons, would reveal a 'prion-like' spreading capability of this protein. Ultimately, with this model we addressed the question of whether a focal overexpression of TDP-43 in a spinal MN population was sufficient to induce widespread MND-like changes in a motor system very similar to humans.

## CHAPTER II. General Methods

### *Animals*

Recordings were performed from two chronically implanted adult female awake behaving Monkeys (*M. mulatta*; Monkeys Mi and Ma, age 6 years, weight 6.1 and 6.9kg at outset). All animal procedures were performed under appropriate licences issued by the UK Home Office in accordance with the Animals (Scientific Procedures) Act (1986) and were approved by the Animal Welfare and Ethical Review Board of Newcastle University.

### *Surgical Preparation*

After behavioural training and MRI acclimatisation were complete, both Monkeys underwent a sterile implant surgery. After initial sedation with ketamine ( $10\text{mg}\cdot\text{kg}^{-1}$  IM), anaesthesia was induced with medetomidine ( $3\ \mu\text{g}\cdot\text{kg}^{-1}$  IM) and midazolam ( $0.3\text{mg}\cdot\text{kg}^{-1}$  IM). The animal was then intubated and anaesthesia maintained using inhalation of sevoflurane (2.5-3.5% in 100% O<sub>2</sub>) and IV infusion of alfentanil ( $0.4\ \mu\text{g}\cdot\text{kg}^{-1}\cdot\text{min}^{-1}$ ). Methylprednisolone was infused to reduce oedema ( $5.4\text{mg}\cdot\text{kg}^{-1}\cdot\text{hr}^{-1}$  IV). Blood-oxygen saturation, heart rate, arterial blood pressure (using a non-invasive blood pressure cuff on the leg), core and peripheral temperature and end-tidal CO<sub>2</sub> were monitored throughout; ventilation was supported with a positive pressure ventilator. Hartmann's solution was infused to prevent dehydration (total infusion rate including drug solutions 5–10  $\text{ml}\cdot\text{kg}^{-1}\cdot\text{h}^{-1}$ ). Body temperature was maintained at 37°C using a thermostatically controlled heating blanket and also a source of warmed air. Intraoperative prophylactic antibiotics (cefotaxime  $20\text{mg}\cdot\text{kg}^{-1}$  IV) and analgesia (carprofen  $5\ \text{mg}\cdot\text{kg}^{-1}$  SC) were given.

Nerve cuff electrodes (Microprobe, Gaithersburg, MD, USA) were implanted around the median and deep radial nerves bilaterally, and secured with the integral sutures. Each cuff contained eight contacts, arranged as two sets of four wires placed radially around the inner circumference. A plastic, MRI compatible headpiece (TECAPEEK MT CF30, Ensinger, Nufringen, Germany) was manufactured based on a structural MRI scan to fit the skull, and fixed using ceramic bone screws (Thomas Recording Inc, Giessen, Germany) and dental acrylic. During the same surgery, intramuscular electrodes comprising Teflon-insulated stainless-steel wires were implanted in eight arm and forearm muscles bilaterally for gross electromyography (EMG) recording. Each EMG electrode was custom made and consisted of a pair of insulated steel wires, bared for 1-2mm at their tips, which were sewn into the

muscles using silk sutures. The EMG and nerve cuff wires were tunnelled subcutaneously to connectors fixed to the headpiece.

Post-operative care included a full programme of antibiotic (co-amoxiclav, dose as above) and analgesics (meloxicam, 0.2mg kg<sup>-1</sup> oral plus a single dose of buprenorphine 0.02mg kg<sup>-1</sup> IM). Nine weeks after the first implant surgery in Monkey Mi, several wires connected to the deep radial nerve cuffs bilaterally were broken, and stimulation through these cuffs was no longer possible. Replacement cuffs (with three contacts each) were then implanted on the radial nerve in the arm bilaterally in a further brief surgery, again with wires tunnelled subcutaneously to the head.

### ***Behavioural Task***

The Monkeys were trained to perform an isometric elbow flexion task with their right arm. Monkey Ma was also trained to perform this task with her left arm. The forearm was placed into a rigid plastic cast. This was 3D printed from a digital model of the forearm made using a laser scanner (Go!Scan, Creaform 3D, Levis, Quebec, Canada), ensuring a close but comfortable fit. A further support held the upper arm; the supports were attached to the training cage to fix the elbow in 90° flexion, and the forearm in semi-pronation so that the radius and ulnar were oriented in a vertical plane. A load cell (LC703-25; OMEGA Engineering Inc., Norwalk, CT, USA) attached to the forearm cast registered elbow flexion torque. The force (kgF) applied to the load cell was recorded as a voltage signal by a custom designed task programme. A calibration factor was determined which allowed for the conversion of the voltage signal back into kilogram force (kgF) at a later stage. To determine the torque (N·m) produced by the animals, the recorded kilogram force was gravity corrected and converted into Newtons (N) and secondly multiplied by the distance between the load cell sensor and the elbow pivot joint (0.08m). The Monkey initiated a trial by contracting elbow flexors to place the torque within a set window (1.65-3.30 N·m). This torque window was kept constant in all sessions, with one exception when the window was widened to (1.41-3.30 N·m) to allow Monkey Ma to complete successful trials. The torque had to be held in this window for 1 s before releasing to obtain a food reward. Auditory cues were used to indicate to the Monkey that the exerted force was within the required window, or else that it was too high. Auditory feedback was also given to mark the end of the hold period.

### ***In vivo assessments***

Both Monkeys underwent weekly awake MRI scanning of their left and right forelimbs and awake electrophysiological recordings. The animals were trained to perform an isometric elbow flexion task, Monkey Mi just with the right arm and Monkey Ma with both left and right arms. The animals performed this task 3 times a week while intramuscular implanted EMG electrodes recorded the activity of their muscles. After the task sessions, the radial and median nerves in either the right or left arm (depending on which arm the animal was performing the task with that day) were stimulated while the intramuscular EMG electrodes and a HD-EMG surface electrode grid recorded signals from the stimulated muscles. These *in vivo* assessments were collected every week for a total duration of 7 months following the injection of the viruses.

### ***Virus injection***

While anaesthetised and under sterile conditions, Monkey Mi and Ma received an intrathecal injection of AAV9-EF1a-FLEX-FLAG\_TDP-43-WPRE ( $5.71 \times 10^{13}$ vg/ml in 1ml) into the subarachnoid space of the lumbar thecal sac at the fifth lumbar level following palpation of spinal landmarks. This injection was followed by an epidural blood patch to minimise the risk of a CSF leak. The animal was moved from the lateral decubitus position into the Trendelenburg position, in which the animal lies in a supine position with its head facing downwards at a 15-30° angle for 10 minutes. This position has been shown to improve transduction efficacy of cervical motor neurons following intrathecal administration of AAVs (Meyer et al., 2015). While in this position, the animal was injected with rAAV2-retro-pAAV-hSyn-CRE-tdTomato ( $8.96 \times 10^{12}$  vg/ml in 500ul) over 5 sites in the right BR muscle. These injections were performed at the motor end plates identified through electrical stimulation of the muscle (Figure 2.1).

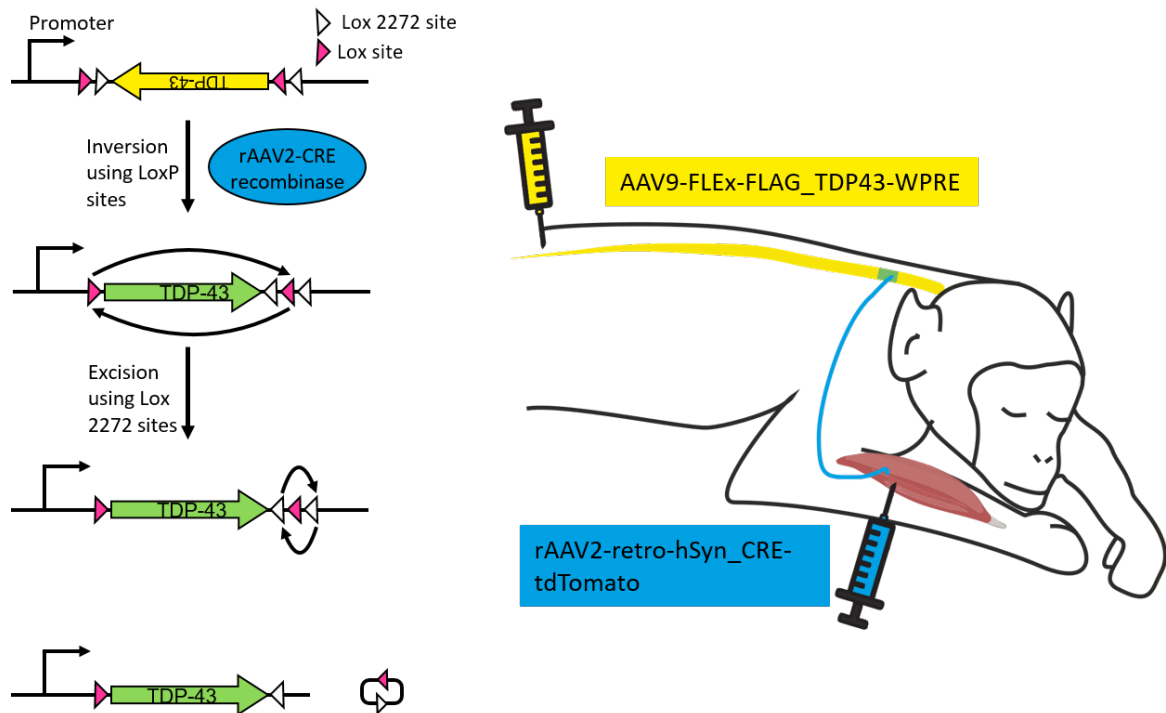


Figure 2.1. An intersectional genetics approach was used to overexpress TDP-43 in an individual spinal motor pool of two rhesus macaques. (A) The FLEX system exploits Cre recombinase to trigger the inversion and excision of the gene of interest from between two loxP sites, thus 'flipping' the gene into an active configuration. (B) The inactive human wild-type TDP-43 protein was injected with an AAV9 vector via lumbar puncture into the lumbar thecal sac. The animals were placed in the Trendelenburg position for 10 minutes after this injection to facilitate rostral spread of the virus to the cervical segments (Meyer, 2015). Simultaneously, a second virus, rAAV2 retro, was injected into the right brachioradialis muscle. Cre recombinase was encoded in this vector, and thus, the TDP-43 gene would be switched into the active, readable state in any cells expressing both viruses. In this way, transduction was limited to the motoneurons innervating the right brachioradialis muscle.

### ***Post-mortem assessment***

Following the completion of the study, the animals were anaesthetised to a lethal level by administering intravenous propofol. The animals were perfused through the heart with phosphate buffered saline (PBS) followed by 10% neutral buffered formalin (NBF). The cortex, cerebellum, brainstem and spinal cord were removed and immersed in 10% NBF for 16 hours at 4°C before progressing through ascending concentrations of PBS sucrose (10%, 20%, 30%) for cryoprotection. A freezing sledge microtome (8000-01, Bright Instruments Co. Ltd, United Kingdom) connected to a solid state freezer (53024-01, Bright Instruments Co. Ltd, United Kingdom) was used to cut the spinal cord and brainstem into 40µm coronal sections, and primary motor cortex (M1) into 60µm parasagittal sections. All sections were stored free floating in PBS at 4°C until further processing.

# **CHAPTER III. Application of Magnetic Resonance Imaging to Identify Onset of Viral Vector Mediated Spinal Motoneuron Loss in a Non-Human Primate Model of MND**

## **Introduction**

Muscle denervation is typically diagnosed based on clinical examination and needle electromyography (EMG). Clinical applications of EMG, however, can be invasive and may not allow for detection of denervation in small or deep muscles (Greenman et al., 2005). Magnetic resonance imaging (MRI) findings have been documented to parallel electrophysiological changes following denervation and throughout the course of muscle atrophy or reinnervation (Kullmer et al., 1998, Kamath et al., 2008), and have been used both alongside the classical techniques as well as independently to diagnose nerve trauma (acute axonal nerve lesions), neuropathies and neuromuscular disorders with diagnostic accuracy comparable to the gold standard of clinical and electrophysiological examination (Bendszus et al., 2004, Wessig et al., 2004). MRI provides a visual representation of the denervated muscles, allowing the exact level and extent of the injury to be defined. It can also provide valuable information about the duration of muscle denervation. A recent study used MRI as a tool for differentiating denervated from reinnervated muscles and also for monitoring motor nerve regeneration (Viddeleer et al., 2016).

Denervated muscles exhibit signal intensity changes on MRI, characteristic to the stage of the denervation process. Several clinical and experimental studies have demonstrated elevated signal intensity and T2 prolongation in acute and sub-acutely denervated muscles on fluid sensitive pulse sequences such as short tau inversion recovery (STIR) or T2-weighted spin-echo based techniques (for example, rapid acquisition with relaxation enhancement (RARE) sequences) with no signal changes on T1-weighted MRI images (Norris, 2007, West et al., 1994, Fischbein et al., 2001). Abnormal signal changes have been reported as early as 24 hours after injury in animal studies and within 4 days in clinical studies (West et al., 1994, Bendszus et al., 2002). Chronic denervation has been characterised in MRI by muscle atrophy, fatty infiltration and high signal intensity on T1 weighted sequences, but showing no change in T2 prolongation (Bredella et al., 1999, Kim et al., 2011). This prolongation of T2 relaxation time in acutely denervated muscles was first described by Polak et al. (1988). By comparing the muscle signal intensities of

unaffected and affected muscles over time, it is possible to differentiate between spared, denervated and reinnervated muscles. STIR and RARE sequences can therefore be used for the diagnosis and tracking of motor denervation (Figure 3.1). Fat saturation methods applied to these sequences improve the identification of signal abnormalities and remove any fatty infiltration related artefacts, but may limit their usefulness for detection of chronic denervation (Viddeleer et al., 2016).

Individual tissues have different associated T2 relaxation times due to their distinct compositions and relative proportions of water, fat and protein macromolecules. Fluids, for example, water or CSF, with few macromolecules to bind free water, have long T2 relaxation times and their signal will appear bright. In tissue such as healthy skeletal muscle, where the protons are more tightly bound, the T2 relaxation time is shorter and so the MR images appear dark (Mitchell et al., 1987). However, when muscle is denervated, the contractile apparatus begins to degenerate and the protons in the muscle tissue become less bound. This results in an elongation of the T2 relaxation time and so higher signal in the affected muscles. The T2 relaxation time thus provides information about proton density within the scanned environment (Yang et al., 2020).

The enlargement of the capillary bed is thought to be the predominant pathophysiological basis for the prolongation in T2 relaxation time in denervated muscles. Enlarged capillaries are the first identifiable histopathological change in denervated muscles and have been identified as early as 48 hours after denervation, and changes in mean capillary area correlate with the variation in T2 relaxation time following injury. In addition, there is an increase in extracellular fluid within the denervated muscles. These findings suggest that an increase in blood volume and extracellular fluid spaces contributes to the increased freedom of protons within the muscle, causing the prolongation of T2 relaxation and appearance of enhanced signal in the affected muscles on fluid-sensitive MRI sequences (Wessig et al., 2004).

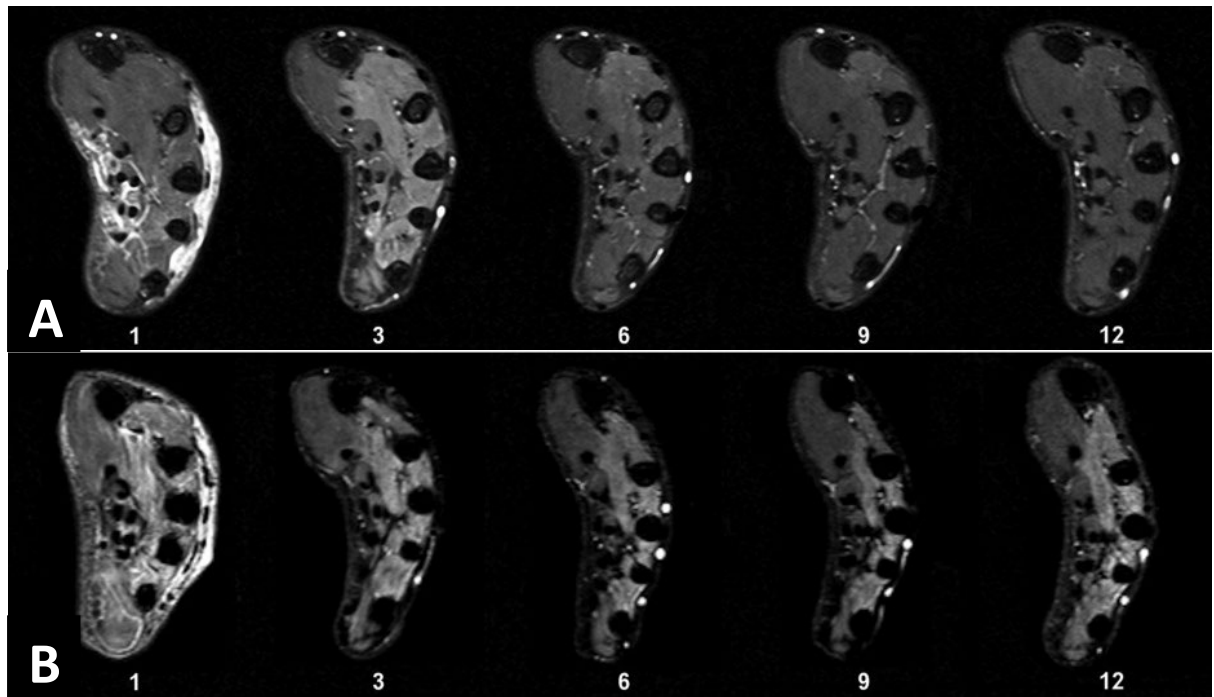


*Figure 3.1. T2-weighted STIR-MRI scans for tracking regeneration in patients with acute denervation. Previous research has been undertaken to assess the validity of using STIR MRI techniques to track the regenerative process of transected and surgically repaired peripheral nerves in the forearms of human patients. All patients in this study had undergone surgical nerve repair within 48 hours of either a median, ulnar or median and ulnar transection. Patients underwent regular scanning to assess their post-op recovery and gain of function. (A) Scans of the affected hand taken at 1, 3, 6, 9 and 12 months show gradual normalisation of hyperintense signal in a patient who had good functional recovery. (B) STIR-MRI scans detect elevated signal intensity in multiple muscles of the affected hand for 12 months following nerve repair surgery in a patient with poor functional recovery (Viddeleer et al., 2016).*

The aim of this study was to determine if T2-weighted RARE-MRI scans could identify the onset of muscle denervation in a muscle whose spinal motoneurons were transfected to overexpress the protein TDP-43, hypothesised to be the active agent in the disease pathway of motor neurone disease (MND). A novel dual virus system was employed in two female rhesus macaques, designed to cause overexpression of the disease protein, TDP-43, in only the motoneurons that supply one particular forearm muscle, the right brachioradialis (BR). By comparing the signal changes in the transfected muscle over the course of 32 weeks to that of the adjacent muscles in the same limb and the same muscles in the control (left) limb, we aimed to determine whether we could identify the occurrence of a viral-vector mediated denervation event in this muscle, as well as assessing the time point and duration of denervation. Using this technique, we also hoped to detect any spread of the denervation into surrounding muscles in the affected limb indicative of spread of disease pathology to adjacent or functionally connected motoneuron pools. To our knowledge, this is the first attempt to apply this technique to tracking the onset of a viral vector mediated muscle denervation event in non-human primates.

## **Methods**

### ***Animals***

Recordings were performed from two adult female Monkeys (*M. mulatta*; Monkeys Mi and Ma, age 6 years, weight 6.1 and 6.9kg at outset). All animal procedures were performed under appropriate licences issued by the UK Home Office in accordance with the Animals (Scientific Procedures) Act (1986) and were approved by the Animal Welfare and Ethical Review Board of Newcastle University.

### ***MRI acclimatisation***

Both animals were acclimated to magnetic resonance imaging (MRI) techniques and procedures using positive reinforcement training. Scans were performed while the Monkeys were awake and behaving. The animals were trained to enter into a specially designed MRI compatible training chair, and raise their head through an opening in the ceiling of the chair which could be closed and secured around their neck to allow for a loose but secure neck-plate restraint. The forearm was placed into a rigid plastic cast 3D printed from a digital model of the forearm made using a laser scanner (Go!Scan, Creaform 3D, Levis, Quebec, Canada), ensuring a close but comfortable fit. The cast was slid into a cylindrical cuff attached to the MRI chair door. This cuff provided support for the forearm and also housed the custom radiofrequency (RF) coil. This allowed the coil to be placed directly over the region of interest in the forearm. The cast slotted into the rigid cuff, fixing the elbow in 90° flexion, and the forearm in semi-pronation so that the radius and ulnar were oriented in a vertical plane. The orientation of the forearm was thus kept fixed in a consistent position throughout and between each session, allowing for routine scanning to study progressive changes. This set up was repeated with right and left arms on different days (Figure 3.2A). A camera was attached to the MRI chair for all scans to provide a view of the Monkey's face at all times, and allow for constant monitoring of behaviour. The Monkeys were trained to accept fluid rewards while in the bore of the scanner through a pump system operated by the investigator. The Monkeys were also trained to accept atraumatic head-fixation during scans using posts attached to their implanted headpieces (see General Methods).

### ***Structural MRI***

The MRI scans were acquired using a vertical 4.7 Tesla research MRI scanner (Bruker BioSpin, Ettlingen, Germany). A custom transmit and receive coil housed in a cuff around

the forearm was used in the scans. T2 weighted Rapid Acquisition with Relaxation Enhancement (RARE) scans were used in this experiment. A fat-selective radiofrequency pulse was used to reduce signal artefacts produced by fat in the subcutaneous fat layer, bone marrow and surrounding the muscles of the forearm. Repetition time (TR) was 7900ms, and echo time (TE) was 57.3ms. The scans were acquired with axial slices with a resolution of 0.55mm, a 128x128 in-plane matrix, and 64 slices with a slice thickness of 1.88mm. 8 scans were acquired in 18min and combined with a median averaging to improve signal to noise ratio and reduce motion induced artefacts.

### ***Post processing***

Raw Bruker scans were pre-processed, segmented and filtered (median and Gaussian) in Fiji ImageJ (NIH). Each scan was then realigned and registered using the `mrregister` function on MRtrix3 (Tournier et al., 2019). Scans from each session were ordered by date and concatenated. Each image was normalised against a Gaussian filtered region of interest (ROI) measured in the flexor compartment, an area not expected or shown to display virus-related signal change. The signal intensity was measured from ROIs respectively drawn in the brachioradialis (BR) muscle (Figure 3.2B). For all slices along the proximo-distal axis (Monkey Mi: 34 slices; Monkey Ma: 40 slices), the brachioradialis muscle was demarcated with a hand-drawn contour within which signal intensity measurements were taken. Mean signal intensity was computed, by averaging all voxels within the obtained BR ROI. Intramuscular blood vessels were masked to remove signal artefacts. Both left and right arm scans were analysed using identical methodology.

### ***Analysis of signal intensity***

Data were analysed using custom scripts written in the MATLAB environment (R2020a, MathWorks). Mean signal intensity in the proximo-distal z slices was smoothed with a moving window of 5 z slices. Windows of z slices were tested against their respective baseline sessions. A total of nine scans spanning sessions prior to and immediately following the virus injections contributed towards the baseline period for the left and right arms of both animals. The mean signal intensity was collected for the baseline sessions. All statistical tests were performed using custom MATLAB scripts. The Benjamini Hochberg procedure was performed to correct for false positives discovered in multiple comparisons (Benjamini and Hochberg, 1995).

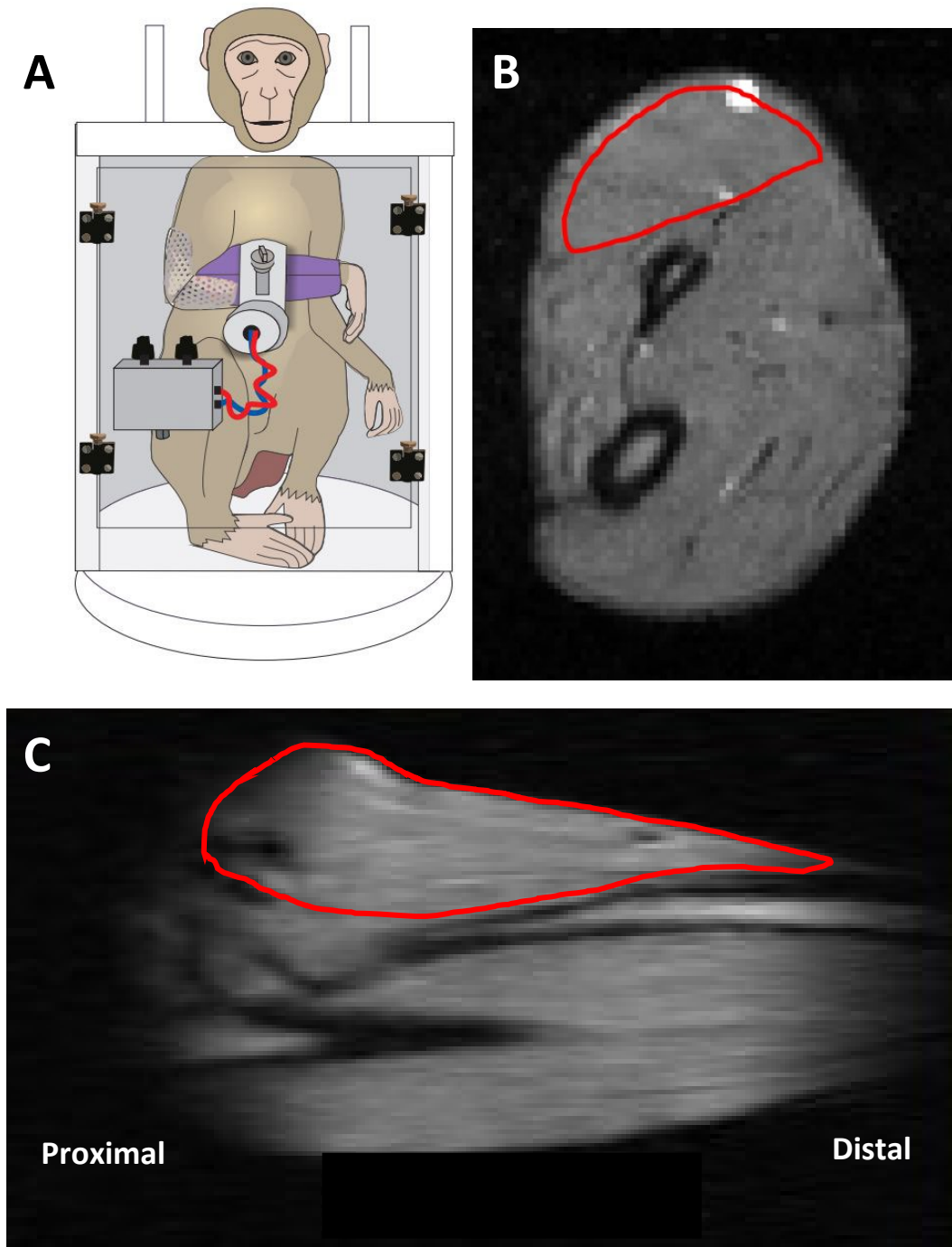


*Figure 3.2. Experimental framework. (A) Macaques were trained to sit in an upright, MRI compatible training cage with their head raised through a neck plate to allow for atraumatic head fixation. The forearm was placed into a closely-fitting rigid plastic cast, which slides into rigid cylinder, providing support for the forearm and also housing the custom RF coil. The coil was connected to a tuning box held on the outer door of the cage. (B) Mean signal intensity was measured within a hand-drawn contour around the BR muscle in all axial slices along the proximo-distal extent of the muscle. (C) The proximo-distal axis of the forearm is displayed in a coronal RARE image. The BR muscle extends from the cubital fossa to the wrist.*

## Results

### *MRI signal intensity*

The animals' left and right arms were scanned on different days, every week for the seven months following the injection of a pair of viral vectors designed to induce the overexpression of the protein TDP-43 in the motor pool of the right brachioradialis (BR) muscle. The right BR muscle in both animals showed an increase in signal in T2-weighted RARE scans at nine and thirteen weeks, respectively, following the virus injections. The progression of signal intensity changes recorded during RARE-MRI scans in the right and left arms of Monkey Mi and Ma are demonstrated in Figure 3.3. Equivalent axial slices from left and right forearm scan images taken from different scans in the same week (2 days apart) are displayed (Monkey Mi: Figure 3.3A-D; Monkey Ma: Figure 3.3E-H). Figure 3.3A and E show scans taken prior to virus injection. Signal intensity appeared constant throughout the muscles of the forearm, including the BR muscle which has been demarcated in red, in all scans at this time point except for in Monkey Mi where the signal in the extensor compartment and BR muscle appeared ubiquitously hyperintense. The radial nerve of Monkey Mi was injured prior to the outset of the experiments during a nerve cuff implantation surgery. This caused a short term reduction in functionality of the right forearm, recognised as a one month decrease in EMG activity and compound muscle action potential (CMAP) from the muscles supplied by this nerve, including the wrist and finger extensors and BR. An increase in signal intensity was observed in RARE-MRI scans, and was seen to decrease progressively over the course of six weeks until there was no noticeable difference. Using this scanning technique we were able to track the recovery and reinnervation of the extensor muscles, including the BR, and thus guide our time frame of injecting the virus and so beginning the intervention phase of the project.

This hyperintense signal in the right BR and extensor compartment in Monkey Mi normalised, and no further signal variations were noticed in any muscle group of the two Monkeys at six and four weeks post-virus injection (Figure 3.3B and F). Eight and fourteen weeks after the viral transfection, bands of high signal began to appear throughout the BR muscle and subsequently increased until week twelve and sixteen, at which point the signal peaked and began to normalise (Figure 3.3C and G). The elevated signal patterns persisted for a total of eight weeks in both animals, after which the BR muscle signal became indistinguishable from that in the surrounding muscles or from baseline sessions (Figure 3.3D and H). No other scanned muscles displayed this abnormal pattern of signal.

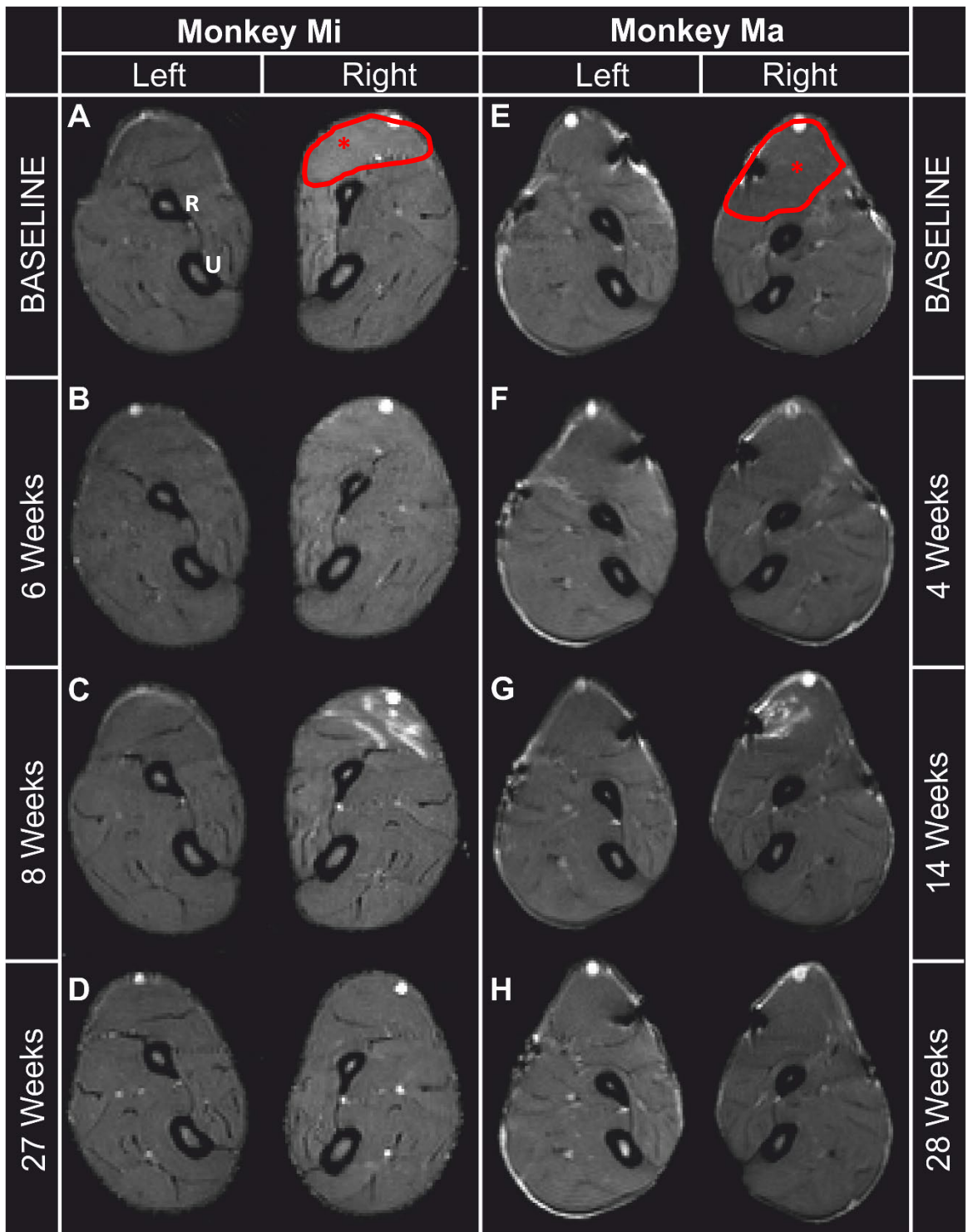


Figure 3.3. Muscle signal intensity from T2-weighted Rapid Acquisition with Relaxation Enhancement (RARE) scans following the injection of a combination of retrograde adeno-associated viruses targeting the right ventral horn brachioradialis motor pool. (A, E) images of the left and right arms taken prior to viral transfection. The brachioradialis muscle is demarcated with a red boundary. (B, F) No signal abnormalities are seen 6 and 4 weeks after virus injections. (C, G) Bands of hyperintense signal have begun to spread lengthways throughout the BR muscle. No other muscles displayed these changes. (D, H) Signal abnormalities normalised after 8 weeks in both animals.

Mean signal intensity was collected from within the hand-drawn boundaries demarcating the BR in every proximo-distal axial slice along the z axis of the muscle. Mean signal intensity in the right BR significantly increased compared to the respective mean baseline BR signal intensity nine and fifteen weeks after viral transfection in Monkeys Mi (Figure 3.4A) and Ma (Figure 3.5A) (Monkey Mi:  $P=0.00034$ ; Monkey Ma:  $P=0.0000021$ ). Signal intensity remained significantly elevated for six and seven weeks in Monkey Mi and Ma, respectively, before returning to non-statistically significant levels. These data are represented by the calculated t-score values in Figure 3.4A-B for Monkey Mi and Figure 3.5A-B for Monkey Ma. The dotted lines indicate when  $t=0.05$ ,  $0.01$ ,  $0.005$  and  $0.001$ . Benjamini Hochberg (BH) multiple comparison correction was applied to the data to control for false positives. The increased signal intensity in the right-BR muscle of both animals passed the BH correction, and so was assessed as statistically significant.

Interestingly, the signal intensity recorded from the right BR muscle in Monkey Mi showed not only this increase in signal intensity, but a later decrease in signal intensity (Figure 3.4A). This decrease did not pass the BH correction for multiple comparisons ( $P=0.0009$ , BH threshold  $P=0.0005$ ). A decrease in mean signal intensity was evident in the left BR of Monkey Mi ten weeks after viral injection, seven weeks earlier than the reduction in right BR signal intensity (Figure 3.4B). This decrease also failed to pass the correction for multiple comparisons ( $P=0.0011$ , BH threshold  $P=0.00063$ ). No significant increase in signal intensity occurred in the left BR in either animal (Figure 3.4B, Figure 3.5B).

Figure 3.4C and Figure 3.5C spatially illustrate the t-score values of Monkey Mi and Ma, with the y axis representing the distal to proximal axis along the BR. These plots indicate a temporospatial relationship to the signal abnormalities, with the signal increase occurring in proximal slices first and progressing distally in later weeks. The significant signal intensity increase in the right BR muscle of Monkey Mi was first recorded nine weeks after the viral transfection (indicated by the dotted line at time point zero) in only a proximal region of the muscle (23-26<sup>th</sup> smoothed z slices). This increase was followed by two high signal peaks, the first occurring proximally (20-25<sup>th</sup> z slices, ten weeks post-injection) and the second occurring two weeks later more distally (15-24<sup>th</sup> z slices, twelve weeks post-injection). As the signal began to decrease from these peaks, it continued to move distally along the BR axis, at which point it was no longer present in the z slices where it was initially recorded (13-20<sup>th</sup> z slice, fourteen weeks post-injection).

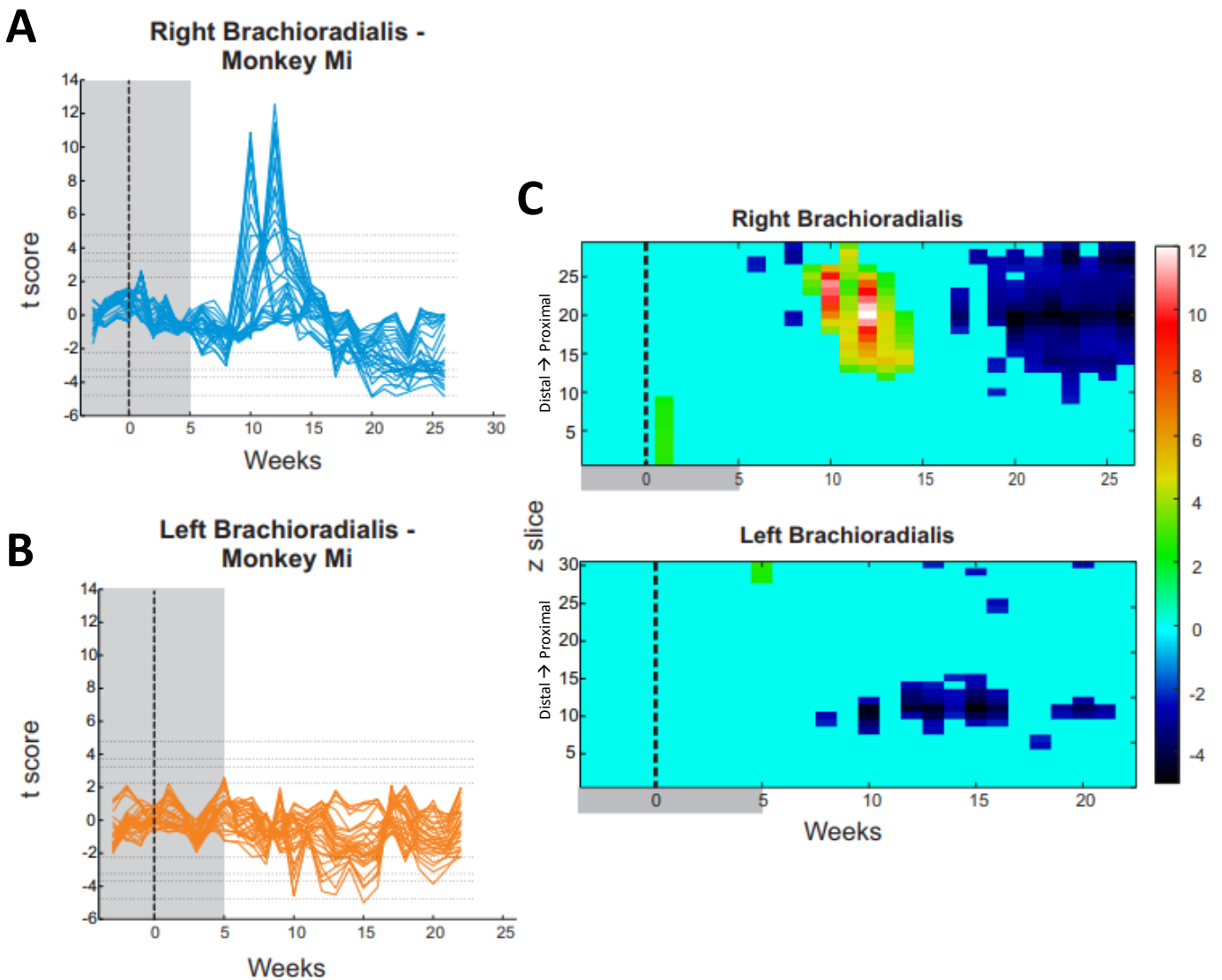


Figure 3.4: RARE-MRI scans recorded changes in signal intensity in the BR muscles of monkey Mi following intramuscular administration of AAVs into the right BR. (A) A significant increase in mean signal intensity compared to baseline was measured right BR of monkey Mi 9 weeks after the virus injections. This increase lasted for 6 weeks before normalising. 2 weeks later the signal intensity decreased and remained below baseline signal intensity. (B) No significant changes were recorded in the left BR of monkey Mi, however a downward trend in signal intensity was noted intermittently from 10 weeks post-injection onwards. (C) Colour maps of these data show a spatiotemporal aspect, with 2 independent peaks in signal intensity in the right arm as well as a gradual progression from proximal to more distal z slices. The reduction in signal intensity in the right BR was clearly limited to the z windows in which a previous increase was noted. A decrease in mean signal intensity was evident in the left BR of monkey Mi ten weeks after viral injection, seven weeks earlier than the reduction in right BR signal intensity. The reduced signal was intermittently present in a more distal region of the left BR than the right. The baseline period is indicated in all plots by a grey shaded area, the time point of virus injection is indicated by the vertical dotted line.

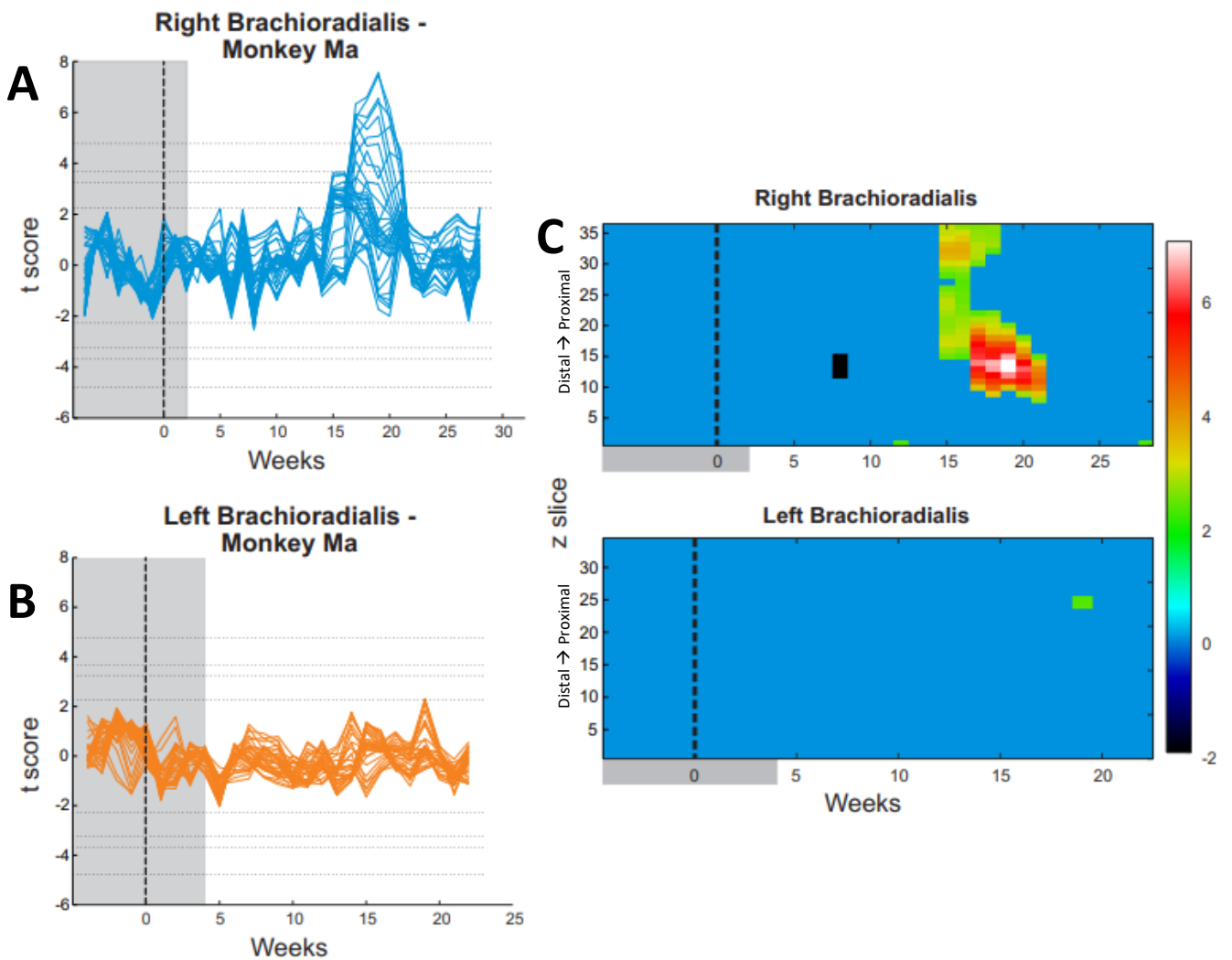


Figure 3.5: RARE-MRI scans recorded changes in signal intensity in the BR muscles of monkey Ma following intramuscular administration of AAVs into the right BR. (A) A significant increase in signal intensity was also recorded in the right BR of monkey MA following the injection of AAVs, however this increase occurred 15 weeks post-injection. This change occurred 6 weeks later than that recorded in monkey Mi. This signal increase lasted 7 weeks in monkey Ma, and once normalised remained at baseline level without any observed reductions in signal intensity. (B) Signal intensity remained unaltered in the left BR for the duration of the study. (C) The temporospatial plots again show 2 independent peaks or regions of altered intensity in the proximo-distal axis of the monkey. The signal increase occurred first in the proximal half of the z windows and increased over the course of 7 weeks while propagating distally. The baseline period is indicated in all plots by a grey shaded area, the time point of virus injection is indicated by the vertical dotted line.

This trend is true for both Monkeys. Two distinct increases in signal intensity were evident in the right BR of Monkey Ma (Figure 3.5C). One peak occurred in the most proximal slices and decreased within five weeks (28-36<sup>th</sup> z slices, fifteen weeks post-injection). A second discrete zone of high signal intensity was recorded in the same week as the former, but in more distal slices (15-26<sup>th</sup> z slices, fifteen weeks post-injection). Over the next five weeks, the second region continued to increase in signal intensity while moving distally along the BR muscle, peaking nineteen weeks after the viral transfection. As in Monkey Mi, the signal increase in the right BR of Monkey Ma was recorded in almost entirely different z slices in final week as compared to the initial week of the signal change event, with the signal remaining constantly elevated in only one z slice throughout that time.

The decrease in signal intensity in the right and left BR of Monkey Mi appeared in clusters of z slices over a period of weeks (Figure 3.4C). Two weeks after the signal in the right BR returned to levels equivalent to baseline, a decrease was recorded in the proximal half of the muscle. This decrease eventually extended throughout 20 z slices (60% of the scanned muscle) and did not recover. The reduced signal was intermittently present in a more distal region of the left BR, beginning ten weeks after viral transfection and lasting for a further eleven weeks.

The spatiotemporal characteristic of the signal intensity increase in the right BR is clearly visible in Figure 3.6A and B for Monkeys Mi and Ma. The proximo-distal z slices were split evenly into four groups: most-proximal, mid-proximal, mid-distal and most-distal. These groups are displayed in an example coronal slice through the arm of Monkey Mi (Figure 3.6C). The mean signal intensity and standard deviation were calculated and plotted as a percentage of the deviation from baseline signal for each group (Figure 3.6). The grey shaded area in the plots again indicates the sessions included within the baseline measurements, and the dotted line represents the time of virus injections. In both animals, the signal intensity increased to the greatest extent and first in the mid-proximal group, where it then spread to the most-proximal slices before progressing distally. The most-distal group displayed very little deviation from baseline in both animals.

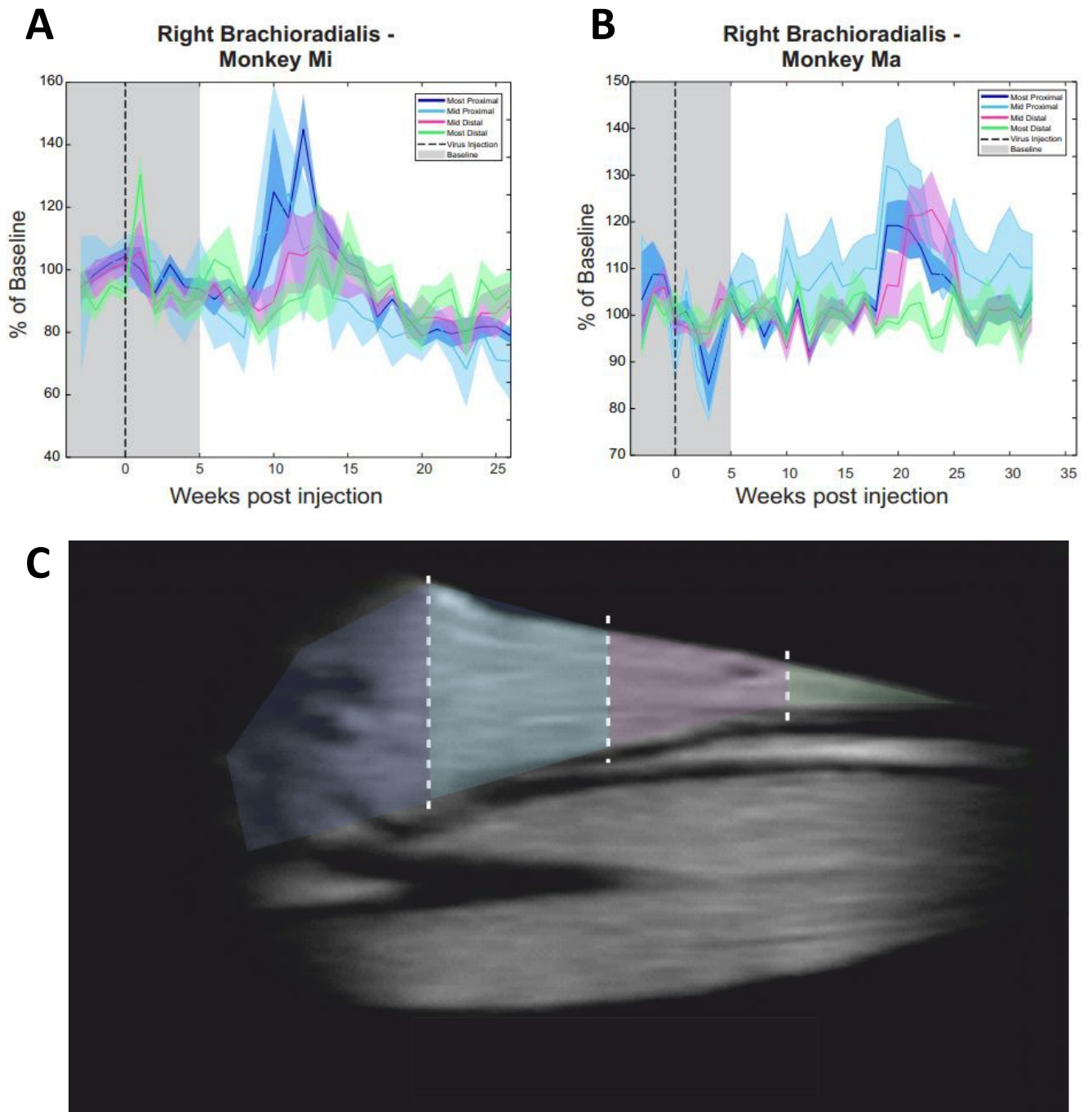


Figure 3.6: Signal intensity increased in a spatiotemporal pattern in both animals. (A, B) The signal intensity within the BR first increased in the mid proximal quarter (indicated by the light blue region in (C)). From this area, the signal first moved into the most proximal area (indicated by the dark blue region) before moving distally towards the wrist. The signal intensity in the most distal quarter (coloured in green) remained largely unchanged.

## **Discussion**

The current study demonstrates that T2-weighted RARE scans can be used to detect the onset of a focal denervation event in the BR muscle following adeno-associated virus vector mediated gene transfer in spinal cord motoneurons of non-human primates.

### ***Methodological considerations***

The signal decreases in Monkey Mi pose some questions and considerations regarding the validity of these measurements as it is possible that this reflects a change in recording conditions. A degradation of the RF coil over time may produce such an effect. The signal decrease was not consistent in both arms however, with a seven week difference in onset between right and left. Furthermore, this decrease did not affect all proximo-distal slices of the arm evenly, as might be expected for a technical artefact. These points may suggest a physiological explanation for this decrease in Monkey Mi.

The acute nerve injury experienced by Monkey Mi prior to the start of the experiments caused a diffuse hyperintense signal throughout the muscles supplied by the damaged radial nerve. This signal looked very similar to other examples of signal intensity following acute trauma picked up by T2-weighted scans (Figure 3.1) (Bendszus et al., 2004). The signal in these muscles remained elevated for seven weeks following the injury before normalising. The recovery of this signal guided our virus injection schedule, however due to time constraints an optimal number of baseline scans were not able to be collected. One month of scans taken post-injection were added to the baseline for analysis, however the three weeks of scans prior to injection may have raised the mean baseline signal intensity measurements, causing the appearance of a reduction several weeks later once the signal had normalised to true baseline.

Fatty infiltration occurring in chronically denervated muscles may cause a reduction in the recorded signal intensity in T2-weighted scans, such as RARE, due to the fat-suppression module (Kim et al., 2011). As such, it is possible that the decrease in the right BR is an indication of the chronic nature of this injury. The decrease noted on the left arm raises further questions, however, of the stability of the nerve cuffs. Monkey Mi underwent two implant surgeries, the second to replace the first set of radial cuffs which had broken, and retained these cuffs for five months longer than Monkey Ma. There is a possibility that this prolonged implantation and multiple surgical implantations could have caused a long-term

inflammatory response around the nerve, leading to chronic denervation on the left radial nerve, marked by a decrease in signal. As the decrease is not observed in Monkey Ma, it's unlikely to be related to the virus action.

The week-by-week signal intensity was normalised using signal from a reference muscle prior to the collection of measurements. For this analysis, a flexor muscle was used as the reference. If the TDP-43 pathology initiated by the viruses was to spread in a prion-like manner to adjacent or functionally connected motoneuron pools within the ventral horn, muscles nearby to the BR may be denervated. Imperceptible signal intensity fluctuations or increases in the surrounding muscles, including the flexor reference, could therefore skew the results of the signal normalisation. To combat this, as in Viddeleer et al. (2016), fluid references could be used in future to ensure a stable reference.

### ***Differences between the two animals***

There are key similarities and differences between the signal abnormalities recorded in right BR muscle of the two macaques. The time at which the bands of hyperintense signal first emerged varied in the animals. The first signal increases were detected visually at nine and thirteen weeks and reached statistical significance at ten and fifteen weeks for the respective animals, giving a difference of four to five weeks between the animals depending on the method of detection. Though the development of these signal abnormalities differed, the progression and duration were highly comparable. In both animals, the increased signal began in the mid proximal region of the BR muscle and spread outwards, first further proximally before advancing distally. An identical pattern of progression along a proximo-distal gradient was seen in both animals (Figure 3.6). The elevated signal remained detectable in the scans themselves for eight weeks in both animals, however when quantified and averaged was evident for only six and seven weeks in Monkey Mi and Ma. These findings may prove useful for monitoring the progression of pathology in virus targeted motoneurons.

Little is known regarding the dose-response relationship of AAV vectors in nonhuman primates (NHPs), with countless disparities in transduction efficacy reported depending on dosage, routes of administration and even body position (Meyer et al., 2015, Bey et al., 2020, Liguore et al., 2019). The two animals in this study were dosed with the same viral genome number based on an average weight of 5kg. Monkeys Mi and Ma weighed 6.1 and 6.9kg at the time of virus injection, which may have contributed to the variability in

transduction efficacy in the animals, exhibited by the four to five week delay in response to the TDP43 expression. Additionally, it is unclear whether the regenerative processes occurring in the nerve around the time of the virus injection may have influenced the efficacy of virus uptake in any way. We cannot be sure of the extent of the injury to the right radial nerve in Monkey Mi and its impact in regards to viral uptake efficacy at the motor endplates.

### ***Source of signal change***

Denervated muscles are thought to display higher signal intensities and a prolongation of T2 relaxation time compared to normal muscle due to various histochemical changes, including increases in the proportions of extracellular fluid and mean capillary bed area (Wessig et al., 2004). The progression and appearance of bands of discrete high signal throughout the right BR muscle recorded in this study differed from previously published characteristics of denervated muscles (Figure 3.1) (Viddeleer et al., 2016), and also from the broad and unspecific increase in signal seen in the muscles supplied by the acutely injured radial nerve in Monkey Mi (Figure 3.3A). These bands of high signal first appeared in the mid-proximal quarter of the muscle, at which point they spread further proximally and into the mid-distal region. The signal intensity in the most distal part of the muscle remained largely unchanged in both animals. It is possible that the macaque BR is organised similarly to the human BR, which has been shown to have multiple endplate zones along the proximo-distal axis and a series-fibered architecture rather than simple parallel organisation of fibres (Christensen, 1959, Lateva et al., 2010, Yang et al., 2017) This type of fibre organisation causes the grouping of motor units (MUs) in different proximo-distal bands, innervated from different sites.

It is possible that the virus was taken up at an endplate zone located in this mid-proximal region, targeting that specific subset of BR motoneurons and thus the fibres specifically innervated by these cells. The spreading of hyperintense signal lengthways along the muscle is analogous to the orientation and morphology of BR muscle fibres and could indicate the propagation of pathophysiological changes throughout the affected motor units in response to focal denervation. Park et al. (2015) have recorded similar hyperintense signal patterns from T2-weighted MRI scans in leg muscles of their rodent model of muscular dystrophy, and shown that these areas correspond to pathological changes identified histologically. The similarity of the signal patterns in the NHP model presented in this study compared to the rodent muscular dystrophy model, and dissimilarity to the

signal seen following acute nerve injury, suggests that the virus has caused biological changes in specific motoneurons and so specific motor units only, rather than the entirety of the muscle. The location specificity of the signal intensity changes demonstrated in this study seems to indicate that the viral vector mediated denervation event is not only limited to the injected muscle, but also to a precise subset of motor units presumably supplied by the transfected motoneurons.

Tracking the gradual reduction in diffuse hyperintense muscle signal following acute nerve trauma has proven effective for monitoring regeneration in animal and clinical studies (Bendszus et al., 2002, Bendszus et al., 2004). It is possible that the timeline of the formation, progression and normalisation of the bands of hyperintense signal following viral targeting of motoneurons, allows us to track motor unit remodelling and compensatory action that occurs following more precise motoneuron loss.

# **CHAPTER IV. Investigating Limb-wide Changes in Voluntary EMG Following a TDP-43 Overexpression Event in a Focal Spinal Motor Pool in Two NHPs**

## **Introduction**

The direct corticomotoneuronal (CM) connection between the motor cortex and  $\alpha$ -motoneurons that exists in primates, and is especially developed in humans, is thought to be the key driver in the development of fine and dextrous movement. Various studies in humans and non-human primates have revealed a preferential connection of the CM pathway to particular upper limb muscles (Phillips and Porter, 1964, Palmer and Ashby, 1992, McKiernan et al., 1998). Evidence of larger post-spike facilitation in a graded pattern along the proximodistal axis of the upper limb indicates that CM cells display a greater tendency to terminate onto motoneurons (MNs) innervating the more distal muscles (McKiernan et al., 1998). Limb muscles are commonly grouped dependent upon the joint around which they act, with distal muscles acting around the hand and wrist, and proximal muscles around the elbow and shoulder.

MNs supplying intrinsic hand muscles, in particular the thenar and interossei, receive the strongest CM inputs, followed by forearm muscles involved in finger movements, such as the ECR (Palmer and Ashby, 1992, Weber et al., 2000). The greater cortical representation of these muscles is linked to their functional role in dextrous movements. The most distal muscles are not all facilitated equally however, as particular muscles, such as those making up the thenar complex are favoured over the hypothenars. Uneven distributions of CM inputs are also present more proximally in the upper limb of humans and non-human primates (NHPs). Early examination of post spike effects found extensor muscles to receive greater facilitation than flexors (Fetz and Cheney, 1980, McKiernan et al., 1998), however more recent analysis performed by Park et al. (2004) identified more comparable facilitation effects in extensors and flexors in simultaneous EMG recorded during a macaque reaching task. Furthermore, there are examples of flexors with larger cortical representations than extensors. The flexor, the biceps brachii, and its extensor counterpart, the triceps brachii are key examples of this finding (Brouwer and Ashby, 1990).

Discrepancies in the CM input between functionally related muscles groups are highlighted in disorders like Motor Neurone Disease (MND). A ‘split hand syndrome’ is often observed at the time of diagnosis (70% of patients), or if not, almost always emerges during the

course of the disease (Wilbourn, 2000, Menon et al., 2015). This phenomenon is characterised by a preferential loss of CM input to the abductor pollicis brevis (APB) and first dorsal interosseous (1DI) muscles, characterised by weakness, while the more medial abductor digiti minimi (ADM) muscle remains relatively spared (Kuwabara et al., 2008, Fang et al., 2016). This disconnected pattern of degeneration is also observed more proximally in the upper limb, in the case of the ‘split elbow’ in which the biceps brachii degenerates to a greater degree than the triceps brachii (Khalaf et al., 2019, Vucic, 2019). There is a clear tendency of muscles whose MNs receive the greatest CM contribution to degenerate selectively in the earlier stages of disease, and the impairment of these muscles contributes to the losses of dexterity characteristic of these early stages.

The imbalance in muscle degeneration contributes not only to the impairment of hand dexterity, but also to gait and possibly also speech abnormalities (Barthelemy et al., 2011, Eisen et al., 2017). These progressive symptoms, along with functional deficits in strength, are often the first signs of disease identified by patients and their clinicians. Due to a lack of disease biomarkers, clinical features described by the revised El Escorial criteria have been classically used in isolation to diagnose or otherwise exclude alternative disorders of the motor system (Brooks et al., 2000). The more recently defined Awaji-Shima and subsequent Gold Coast consensus criteria have clarified the importance of electrophysiological tests in the diagnosis of MND, in particular the use of EMG and nerve conduction studies (de Carvalho et al., 2008, Shefner et al., 2020). Where clinical biomarkers are lacking, with further validation, electrophysiological biomarkers may facilitate earlier diagnosis. Already the identification of fasciculation potentials using needle electromyography (EMG), and the application of nerve conduction studies (NCS) for motor unit number estimation (MUNE) techniques are used routinely in clinics, however they are not sufficient as yet to provide a diagnosis in isolation (de Carvalho et al., 2018). The most effective time during the disease onset and progression for such tests, and later for interventions, is as yet unknown.

In this study, we were able to track the average EMG recorded from eight muscles of the upper limb in two macaques during the performance of an isometric elbow flexion task. The brachioradialis (BR) muscle of the right limb was selected as the experimental muscle in this project. A combination of viruses triggered an overexpression of the protein implicated in MND propagation, TDP-43, in the MN pool innervating this muscle. The tracking of EMG allowed us to define patterns of change in the right-BR over a seven

month period following the virus administration, allowing us to categorise the series of events and timeline of impairments. We recorded from several muscles in the limb simultaneously in order to identify any similar abnormalities and to ascertain whether any spread of disease occurred into neighbouring or distant motor pools.

The brachioradialis (BR) presented a number of advantages as the experimental muscle. As previously mentioned, the CM connection is known to be more developed in the muscles involved most in hand and wrist extension. The BR, while primarily considered to be an elbow flexor, is part of the radial extensor compartment of the forearm and plays a role in wrist pronation in particular postures (Boland et al., 2008, Kleiber et al., 2015). This muscle also has a great deal of redundancy, which was important in the design of the project so as to allow the animals to lead a functionally normal life in the event of severe degeneration.

## **Methods**

### ***Animals***

Recordings were performed from two adult female awake behaving Monkeys (*M. mulatta*; Monkeys Mi and Ma, age 6, weight 6.2 and 6.7 kg respectively). All animal procedures were performed under appropriate licences issued by the UK Home Office in accordance with the Animals (Scientific Procedures) Act (1986) and were approved by the Animal Welfare and Ethical Review Board of Newcastle University.

See General Methods for details regarding the isometric hold task, surgical preparation and details of virus administration and vector contents.

### ***Electrophysiological Recordings***

Recordings were made from pairs of intramuscular electromyography (EMG) electrodes implanted in eight muscles of the left and right forearms (anterior deltoid, biceps brachii, brachialis, extensor carpi radialis, extensor digitorum communis, brachioradialis, flexor carpi radialis, flexor digitorum superficialis). Additional recordings (not considered in this chapter) were made from the brachioradialis muscle using a high-density surface EMG grid (GR04MMI305, OT Bioelettronica, Turin, Italy) with 64 electrodes (spacing 4mm). Standard surface adhesive electrodes (Neuroline 720; Ambu A/S, Ballerup, Denmark) were placed over the flexor and extensor tendons at the wrist to act as reference and ground for the surface grid. The surface grid electrode was connected to a custom printed circuit board containing a 64-channel amplifier (gain 192; bandwidth 30Hz - 2 kHz) and an analogue-to-digital convertor (RHD2164; Intan Technologies LLC, Los Angeles, CA, USA). An implanted nerve cuff electrode was used as the ground for the intramuscular electrodes. The intramuscular EMG electrodes were connected to a second analogue-to-digital converter (Intan Technologies) via a connector mounted onto the headpiece. Digitized signals were sent over a serial peripheral interface (SPI) cable to an RHD USB interface board (also Intan Technologies). This allowed data to be captured to a computer hard disc (5 kSamples/s) along with the elbow torque signal and digital markers signalling the phases of task performance and stimulus timing. Voluntary brachioradialis activity was recorded from the intramuscular and grid electrodes during performance of the behavioural task.

### ***Task Analysis***

All analysis was performed offline using custom software written in MATLAB. Triggers recorded at the beginning and end of the 1s trial window were used to isolate EMG signals

during this period. Data were smoothed over a 150ms window. These signals were rectified and an average EMG trace for each muscle was calculated. The mean of this averaged trial EMG provided a measure of the average EMG activity recorded per muscle during the task contractions in each session. Average EMG from each session following the virus injection was normalised against a group of baseline sessions, to provide a percentage deviation from baseline EMG across the 7 months following. All baseline sessions were collected prior to the injection of the viruses in Monkey Ma. During a nerve cuff replacement surgery performed in Monkey Mi, the right radial nerve was injured. The deficits caused by this injury can be noted in Figure 4.2. Time limitations meant we had to go ahead with the virus injections immediately after the EMG signals had recovered to baseline. Due to this, baseline sessions for Monkey Mi were taken as the first 10 sessions immediately following the injection, after the EMG signals had recovered to baseline. A two-tailed t-test was performed on each data point post-injection against the group of baseline averages. Data which reached the alpha significance level set at 0.05 were marked in black and regarded as ‘discovery P values.’ Multiple comparisons were corrected within each Monkey using a Benjamini-Hochberg (BH) correction with a false discovery rate of 5%; any data which passed this more stringent significance criterion was marked in red (see Results) (Benjamini and Hochberg, 1995).

Additionally, t scores were generated from the mean EMG signals of each sampled muscle of the working limb and summated to give a Z score, as described in Eq (4.1) and (4.2):

$$t_{n,ch} = \frac{D_{n,ch} - \text{mean}(b_{ch})}{\text{std}(b_{ch})} \quad (4.1)$$

where the mean of the baseline EMG for each muscle ( $ch$ ) was subtracted from  $D$ , which represents the percentage deviation of the mean EMG from the baseline ( $b$ ) for each session ( $n$ ) and each muscle ( $ch$ ). This value was then divided by the standard deviation ( $std$ ) of the baseline to give a t score for each muscle per session.

$$Z = \sum \frac{t}{\sqrt{ch}} \quad (4.2)$$

The t score was divided by the square root of the number of muscles involved, and summated to give the Z score.

This Z score was used to determine any overarching trends in the EMG activity of the muscles. These results were analysed with the same two-tailed t-test and subsequent BH multiple comparisons correction described above.

The average torque produced during each trial was examined in a similar way to the intramuscular EMG with the goal of determining whether the Monkeys produced differing levels of force over time. This measurement also provided a visual interpretation of whether any increases or decreases in recorded EMG signals synchronised with changes in torque.

## Results

Two animals were trained to perform an isometric elbow flexion task within a set torque range (1.65-3.30 N·m), equivalent to 2-4kgF, primarily designed to engage the brachioradialis muscle. Using this task we were able to track any changes in muscle activity through the use of chronically implanted intramuscular and surface electromyography (EMG) electrodes. Both Monkeys were trained to perform this task with their right arms, but only Monkey Ma was additionally trained to perform this task with her left arm. A schematic of the experimental set up is displayed in Figure 4.1A.

Chronic intramuscular EMG electrodes recorded signals from eight muscles of the training arm (anterior deltoid, biceps brachii, brachialis, ECR, EDC, brachioradialis, FCR and FDS) during the task performance. An average rectified EMG trace for each muscle was generated per session from the EMG recorded during each task trial (Figure 4.1B). An average of  $109\pm 44$ ,  $135\pm 53$  and  $124\pm 52$  trials (mean $\pm$ SD) were performed each session by Monkey Mi with her right arm, and by Monkey Ma with both right and left arms. The mean of the average trace during the hold period was calculated and this value was tracked over the course of the project for all eight muscles per training arm (Figures 4.2 – 4.4). The average torque produced during a session was measured in the same way (Figure 4.1C). The animals performed this task with their training arms, either right arm only or both right and left arms, each week for the duration of the project.

Recordings from eleven sessions were collected for both right and left arms for Monkey Ma and averaged to provide a baseline EMG signal for each muscle (indicated within the grey shading in Figures 4.2 – 4.4). The pair of viral vectors, designed to induce a focal overexpression of TDP-43 in spinal motoneurons (MNs), were injected into the intrathecal space and in the right brachioradialis muscle, respectively, once the baseline period was complete (indicated by the red dotted line in Figures 4.2 – 4.4). Monkey Mi suffered an injury to her right radial nerve during the implantation of a replacement radial stimulating cuff. This injury caused a six-week reduction in the average EMG recorded from the right BR and EDC muscles, and a shorter term impairment of the right ECR muscle (Figure 4.2A). At this time, the signals from the anterior deltoid, biceps, brachialis and FCR muscles increased presumably to compensate for the deficit in the radial innervated muscles in order to allow the animal to continue to perform the task. The signal from each implanted radial innervated muscle recovered after six weeks, and this recovery was used to direct the beginning of the intervention phase of the project, marked by the delivery of the viral

vectors. Due to this injury, the ten sessions immediately following the virus injections were taken as a baseline period for Monkey Mi (as marked in grey in Figures 4.2 – 4.4).

Following the virus injections and baseline period, significant changes occurred in all implanted muscles in the right limb of Monkey Mi except for the R-deltoid and R-FCR. Average EMG signals recorded from the R-BR and R-ECR decreased to 46 and 64% of baseline respectively in one session five weeks after the virus injections, however these changes did not pass the BH correction for multiple comparisons. One month later, the R-ECR again dropped to 65% of baseline, and the average EMG from the biceps increased to 243%. The biceps EMG increased twice more in irregular sessions without following any clear trend ( $P < 0.05$ ). Twenty one weeks after the virus injections, EMG signals from the R-EDC, Biceps, BR and FDS all increased to over 200% of their respective baseline signals. The elevation in the BR was the only change to pass the BH correction for multiple comparisons. After this two week long increase, the signals equilibrated in these muscles after which point the EMG recorded from the R-ECR and brachialis decreased to around 50% of baseline. The R-ECR remained decreased for 4 weeks ( $P < 0.05$ ).

In order to pull out limb-wide trends in the EMG signals, the  $t$  scores from each muscle of Monkey Mi's right limb were summated to give a limb wide Z score (Figure 4.2B). Decreases in the sum lined up with those seen in the BR and ECR muscles following the virus injections, which when taken together passed the BH multiple comparisons correction. These decreases outweighed the increases seen in the biceps which occurred at an overlapping time. The summated Z score showed a statistically significant increase, passing the BH correction for multiple comparisons, at the time of the rise in the BR, EDC, FDS and Biceps. Immediately following this, the summated Z scores were reduced for the duration of 5 weeks, before normalising shortly before the termination of the project. The drop in the Z score passed the BH correction. The torque produced by Monkey Mi during this task decreased 2.5 months following the injection of the virus and remained at the lower limit of the range allowed for successful task completion for the entire duration of the project (Figure 4.2C). The prolonged reduction in torque passed the BH correction. Torque was not recorded prior to or during the nerve injury recovery due to an error in the recording system.

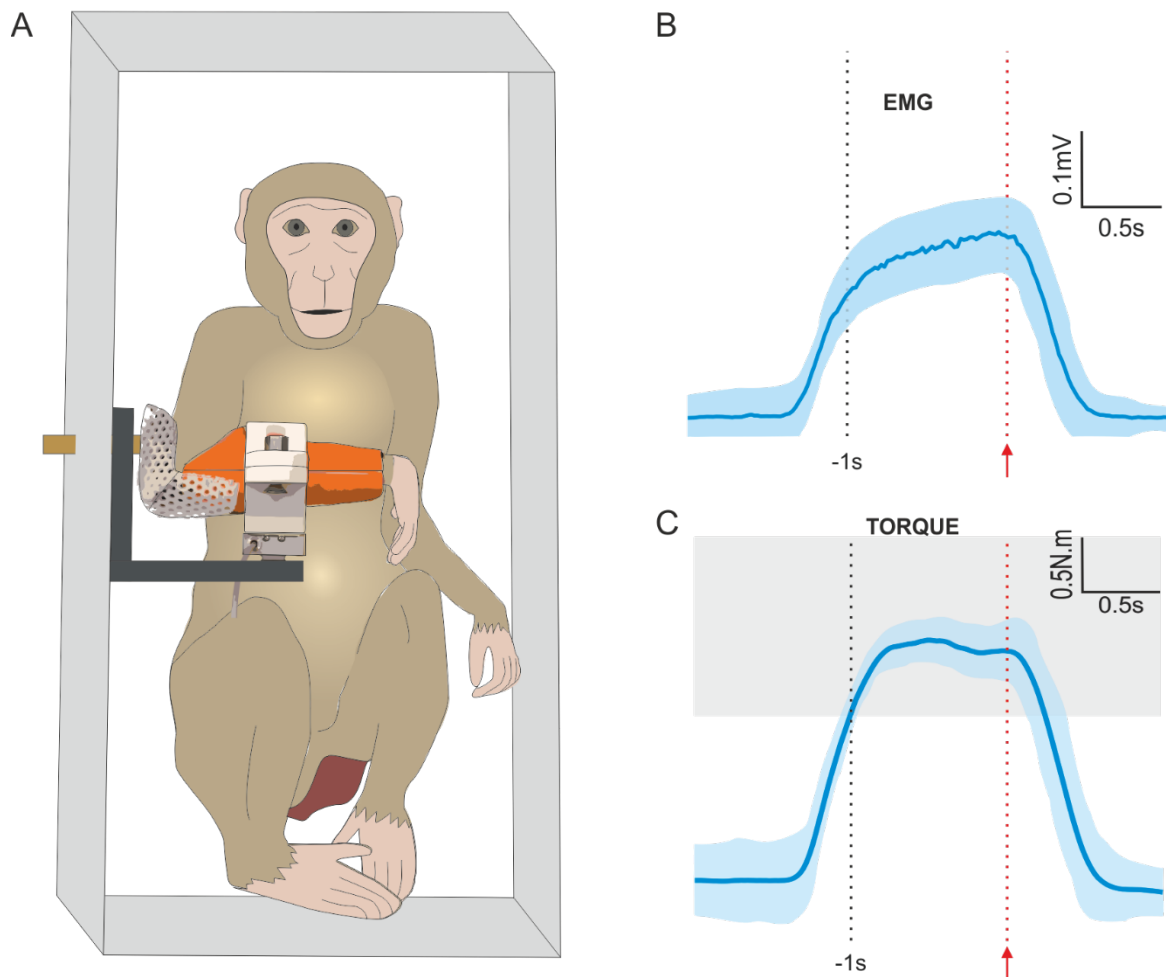


Figure 4.1. Two animals were trained to perform an isometric elbow flexion task with a 1 second hold within a set torque range. (A) The animals were trained to place their training arm into a rigid plastic cast, 3D printed from a digital model of their forearm, which held their forearm in a constant posture between sessions. A load cell connected to the base of the cast detected applied torque during the task movement (see Methods for details). (B) EMG signals recorded during each trial window were rectified and averaged. The solid blue line represents the average trial EMG ( $n=200$  trials), with the standard deviation represented as the shading. EMG signals from the 1s hold period were aligned to the end hold marker, indicated in red, and extracted for analysis. (C) The torque produced by the animals was measured by the load cell and recorded as a voltage signal by a custom designed task programme. The solid blue line indicates the mean torque produced during one session ( $n=200$  trials), with the standard deviation represented by the shaded area. The defined torque range that the Monkey had to hold within is indicated by the grey box.

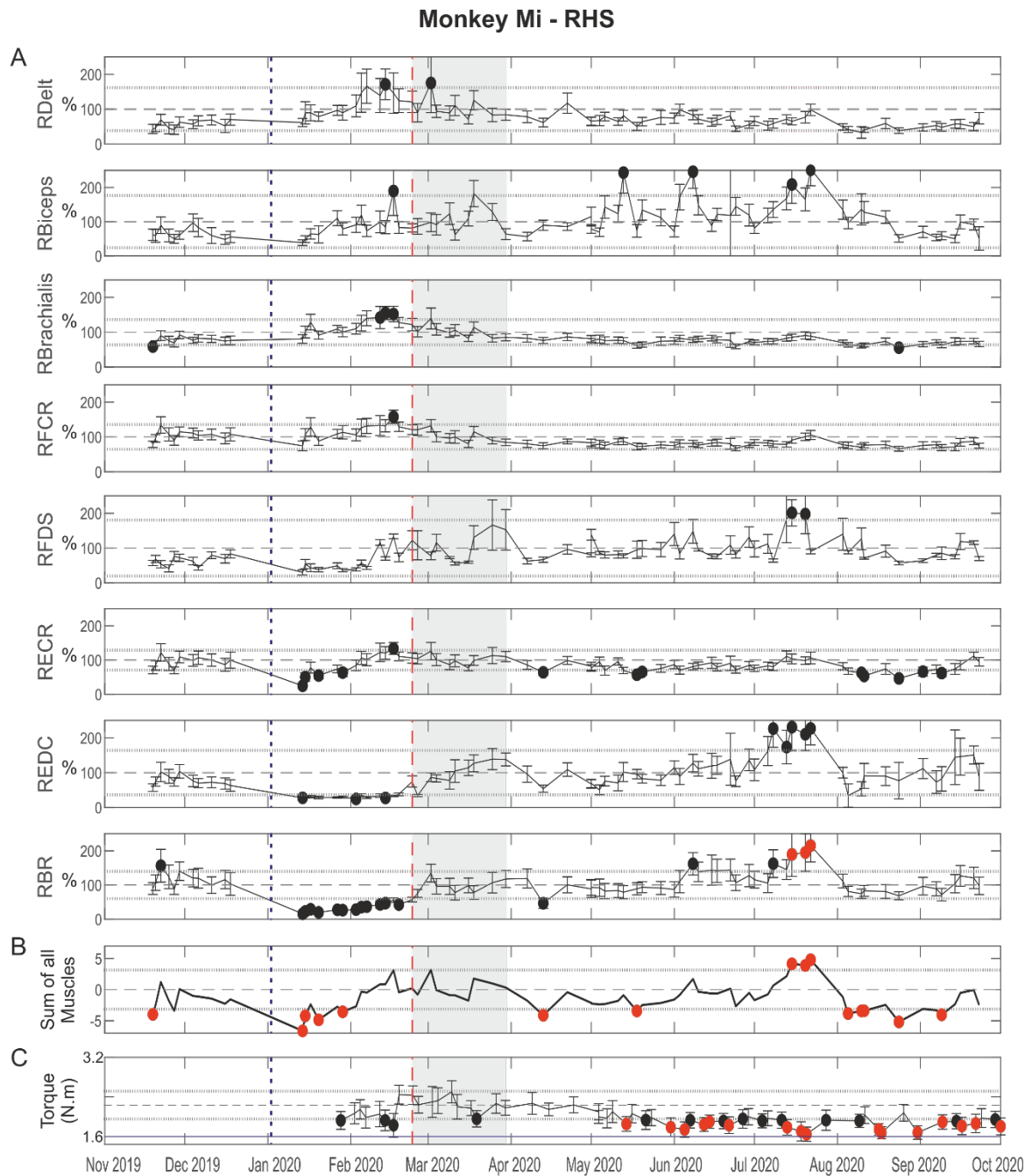


Figure 4.2. Average values per session, measured as a percentage of baseline, of the EMG produced by eight muscles of the right arm of Monkey Mi during the performance of an elbow flexion task. Due to an accidental injury to the right radial nerve during an implant surgery (time of injury indicated by blue dashed vertical line), the baseline period (grey shaded area) was collected retrospectively after the virus injections (red vertical line). (A) The deficits in the radial innervated muscles, the ECR, EDC and BR, can be seen clearly prior to the virus injections, in addition to an increase in activity of the more proximal muscles and FDS, presumably to compensate for this temporary weakness. The ECR and BR were the first muscles to deviate from baseline (64 and 46%, 5 weeks post injections). These reductions met the alpha level of 5%, indicated by black markers, but did not pass BH corrections. The next collective change in individual muscle EMG occurred 21 weeks after virus injections, when the biceps, FDS, REDC and BR all increased to over 200% of

baseline. Only the increase in the BR passed the BH correction, indicated by red markers. After this increase, the brachialis and ECR were reduced ( $P < 0.05$ ). (B) The Z score for the right limb identified three periods of change; the first an intermittent reduction in average EMG, the second an increase and finally a limb wide reduction which appeared to normalise to baseline in the final week of the study. (C) The average torque produced by Monkey Mi during each session was reduced 2.5 months after the virus injections and remained at the lower limit of the set window for the duration of the project. The increase in EMG did not correspond to an increase in torque. The horizontal dashed line indicated the baseline mean, and dotted lines 2 standard deviations (SD) of the baseline. The lower torque limit is marked in blue (C).

Only the EMG signals from the R-deltoid of Monkey Ma's right arm increased to statistically significant levels passing the BH correction for multiple comparison (Figure 4.3A). The signals from this muscle were increased to over 130% of the average baseline EMG for the first five months after the virus injections, at which point they became marginally lower than baseline. Six weeks post injection, the R-brachialis and R-FDS EMG signals increased to 147 and 133% of baseline for one week, although these changes only met the discovery significance limit of 0.05, and did not pass the BH test. Eighteen weeks after the virus injections, the EMG recorded from multiple muscles (R-biceps, R-BR, R-FCR and R-FDS) decreased to between 38-73% of their respective baseline signals. This decrease was intermittent, with two distinct periods separated by at least three weeks when EMG was similar to the baseline period.

As before, the mean EMG amplitude from all muscles of Monkey Ma's right arm were summated to provide a Z score. Following the virus injections, the Z score of the right limb increased and passed BH multiple comparison correction (Figure 4.3B). The primary increase in the summated value corresponded with the increase recorded in the R-brachialis and FDS. A second increase was recorded three months following the injection of the viruses and remained for two weeks. Following this, the Z score decreased, reaching alpha significance levels (0.05) and passing BH correction. The summated EMG signals were reduced in two distinct time periods, the first of which occurred 18 weeks after the virus injection and the second at 24 weeks, as noted in the individual muscles, and did not recover. There were few changes of note in the average torque produced by Monkey Ma during her performance of the right arm task for the duration of the project, with a decrease to the lower limit of the range recorded in the first session post injection (Figure 4.3C). A further decrease was noted in one session, 25 weeks later. In this later session the torque window was widened to (1.413-3.295 N·m) to enable the animal to complete the trials successfully as she had been presenting difficulty in maintaining the torque within the pre-defined window.

As Monkey Ma was trained to perform this task with both arms, a direct comparison could be made between the transfected and non-transfected limb. No changes in the EMG signals recorded from each implanted muscle of the left arm passed the BH correction for multiple comparisons (Figure 4.4A). The signals from the L-deltoid and L-ECR increased to between 265-215% of baseline, and reached the alpha significance value of 0.05 at these time points. The increases in the L-deltoid EMG were limited to two sessions which

occurred ten weeks after the virus injections, while the L-ECR signals increased in three irregular sessions, occurring 3, 8 and 21 weeks post injection, in amongst a general downward trend. Only the L-brachialis showed other individual muscle EMG changes. One month after the viruses were injected in the contralateral limb, the signals decreased to between 30-41% of baseline. The signal remained reduced for the duration of the project, however none of these sessions passed BH multiple comparison correction.

The EMG signals of each implanted muscle of the left limb were summated to generate a Z score for the left arm, in order to identify an overall trend in the EMG signals. While few changes of note were identified in the individual muscle plots, when combined, clear trends were identified. Similar to the pattern of change recorded in the right limb, an initial increase was followed by a clear downward trend. This decrease began 13 weeks after the viruses targeting spinal MNs supplying the contralateral limb were injected, and extended for the duration of the project. The left arm Z score identified three distinct periods of EMG reduction. The latter two periods both occurred in the same weeks as the two periods of reduction recorded in the right limb (Figure 4.3B). The torque produced by the animal during the left arm task was significantly decreased at multiple points after the virus injections in the right arm, and in fact remained reduced compared to the torque exerted during the baseline period.

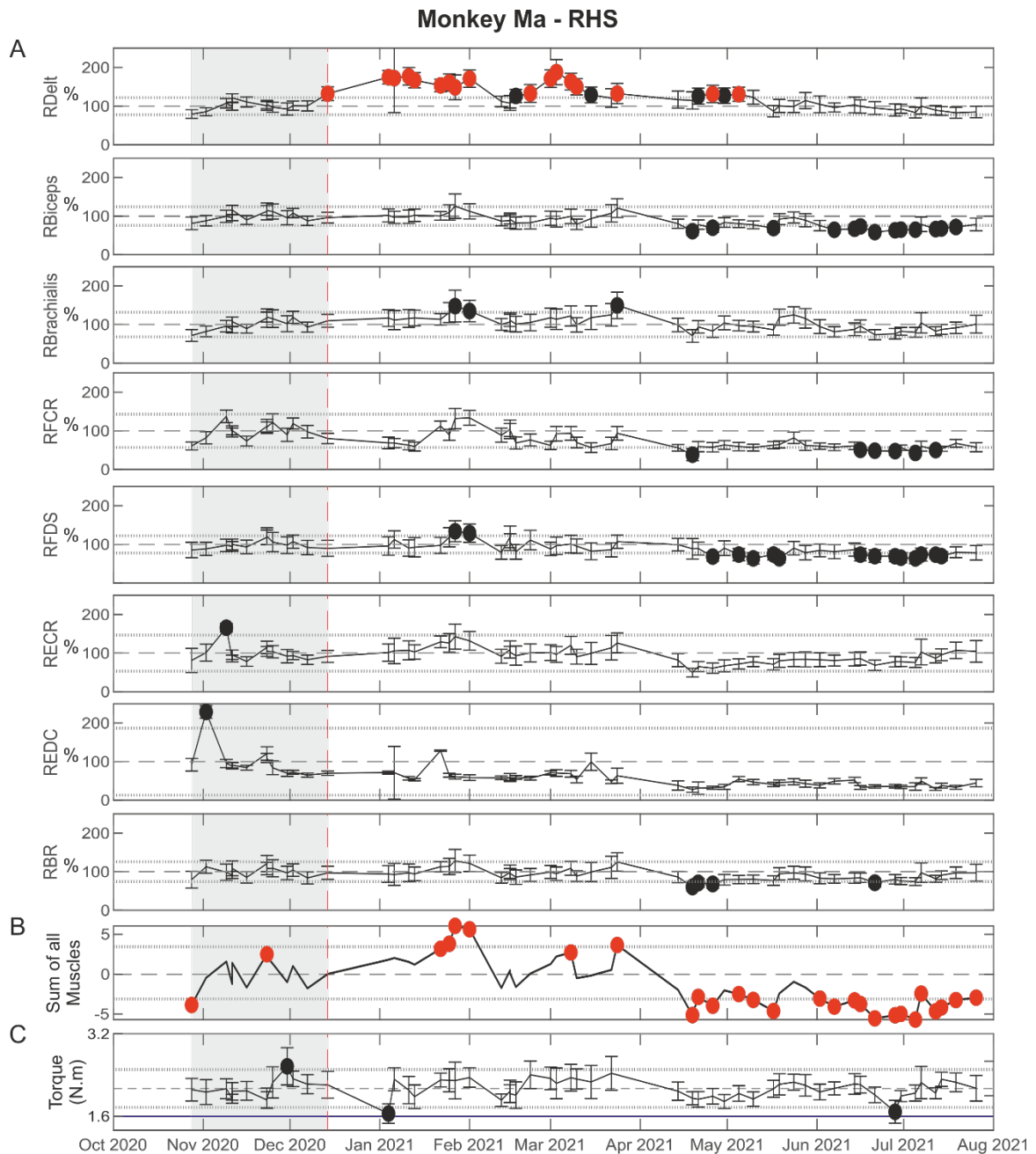
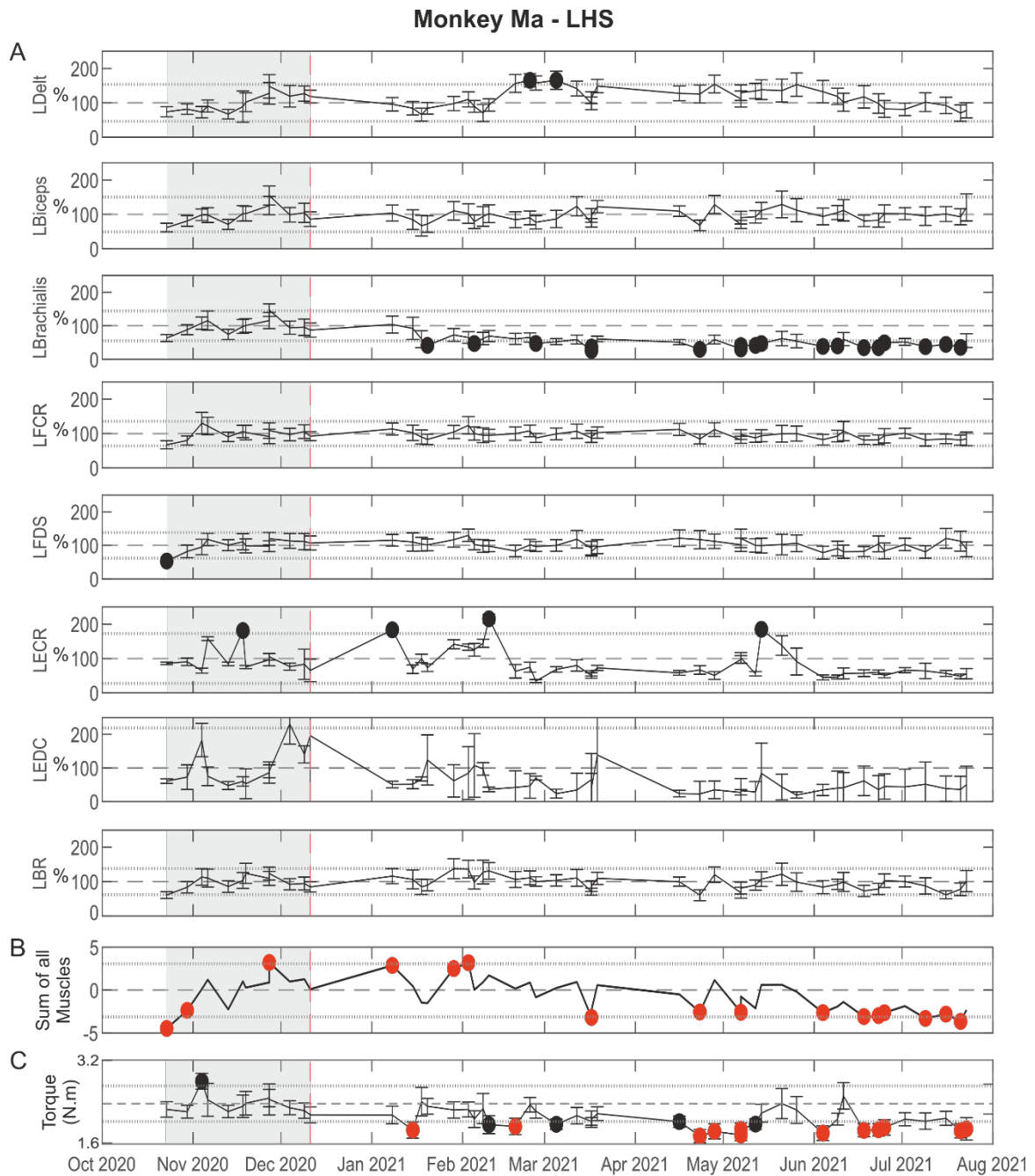


Figure 4.3. Average EMG per session, measured as a percentage of baseline, from eight muscles of the right arm of monkey Ma during the performance of an elbow flexion task. (A) EMG from all muscles, except the R-ECR and EDC, deviated from baseline ( $P < 0.05$ ), with sessions that reached the alpha level of 5% marked in black. Only the changes in the deltoid passed the BH correction; marked in red. The signals from the brachialis and FDS were elevated 6 weeks after the virus injections, but shortly normalised. 18 weeks after the virus injections, EMG signals from the biceps, forearm flexors and BR decreased to between 38-73% of baseline, with these individual changes reaching alpha levels ( $P < 0.05$ ). (B) The Z score for this limb indicated four phases of change. Two distinct increases were recorded followed by two more extended reductions. Periods of normalisation to baseline were identified between each phase. (C) The average torque produced was relatively unchanged from baseline during the study, with the exception of the first session after the virus injections, and a session 28 weeks post injection during which the lower torque limit was reduced to enable the monkey to complete successful trials ( $P < 0.05$ ). The horizontal dashed line indicated the baseline mean, and dotted lines 2 SDs of the baseline. The lower torque limit is marked in blue (C).



**Figure 4.4.** Average EMG per session, measured as a percentage of baseline, from eight muscles of the left arm of Monkey Ma during the performance of an elbow flexion task. (A) Fewer changes in individual muscles were recorded in the left arm of Monkey Ma than the right (Figure 4.3). Only deviations in EMG signal from baseline in the deltoid, brachialis and ECR reached the 5% alpha level, however these changes did not pass BH correction; marked in black. The baseline sessions (grey shaded area) were collected prior to the virus injections targeting the contralateral limb, indicated by the red dashed line. (B) The Z score for the left limb indicated four phases of change, as in the right arm, however only the first phase displayed an increase in EMG. The changes recorded in these phases passed the BH correction; marked in red. Again, each phase was separated by a return to baseline. (C) The average torque was reduced intermittently throughout the study, with many of these

changes surviving BH correction. The horizontal dashed line indicated the baseline mean, and dotted lines 2 SDs of the baseline. The torque limits extend the entire y axis (C).

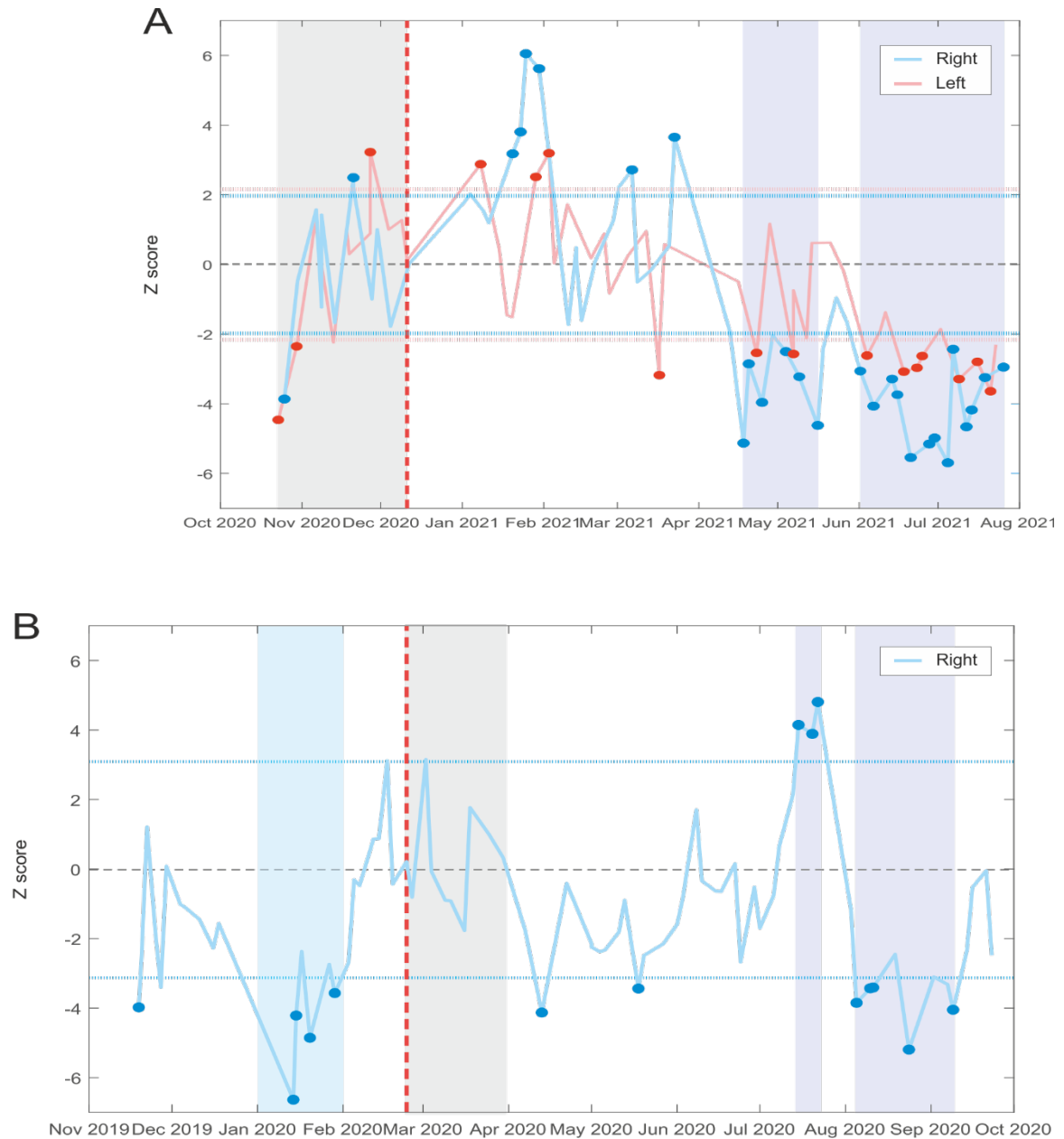


Figure 4.5. Distinct temporal patterns in the EMG changes are present and shared both between the two animals and between limbs. (A) Z scores from the right and left limbs of Monkey Ma display shared temporal components. The Z scores of the right (blue trace) and left arms (red trace), calculated by summing the EMG signals from all sampled muscles, both increase for 4 weeks, 1 month after the injection of a combination of AAVs designed to target the spinal MNs supplying the right BR muscle. More muscles contribute

*to the increased right limb Z score, and the increase is more prolonged in the right arm. Three distinct reductions in the left limb Z score are recorded after the baseline period (grey area), with the latter two aligned to the week that similar reductions occurred in the contralateral limb. Again, more muscles were involved in the reduction recorded in the right limb. Filled markers represent data that survived the BH correction for multiple comparisons. (B) Monkey Mi was unable to perform the isometric task with her left arm, and so no inter-limb comparisons can be made in her case. The limb-wide changes in EMG signals differed between the two animals, possibly due to ongoing re-innervatory processes as a result of the nerve injury sustained by Monkey Mi (initial effect indicated within the blue shading). Rather than increasing early after the virus injections, the Z score associated with Monkey Mi's right limb decreased. This reduction could be regarded as two separate phases due to the 5 week separation. Rather than two distinct periods of reduction, a period of increased EMG preceded a final decrease. This final reduction occurred an equivalent stage of the project to the final decrease recorded in the right arm of Monkey Ma. The two plots are aligned to their injection time, with equal distance per month in order to clarify the conserved temporal pattern. The dashed line indicated the baseline mean, and colour coordinated dotted lines 2 SDs of the baseline.*

There was temporal conservation of this phasic pattern in the Z scores of each limb even between animals. Three or four phasic changes were identified in each training limb, beginning around one month after the virus injections (Figure 4.5A, B). The first two of phases occurred in the first approximately four months of recordings, and appeared more disordered with less clear boundaries between changes and recovery to baseline. Differences in the direction of change between the two animals during this time may represent individual differences in task performance and muscle involvement. The final two phases, recorded approximately four months after the virus injections, with a two week delay in Monkey Mi, were temporally aligned both across animals and between experimental and control limbs. Both Monkeys also showed a similarly-timed reduction prior to the injections. In Monkey Mi this reduction was as a result of the nerve injury, however given the timeline for Monkey Ma it is likely a sign of recovery and re-learning of the task following the implant surgery which took place one month prior.

## Discussion

Two Monkeys were trained to perform an isometric elbow flexion task weekly for between seven and eight months after the injection of a combination of viral vectors designed to induce the overexpression of the protein TDP-43 in the spinal MNs supplying the right brachioradialis (R-BR) muscle. Chronically implanted intramuscular EMG electrodes allowed us to record from eight muscles per training arm, including both flexors and extensors. By comparing the average EMG signal from these muscles over time we were able to track any changes in the output from the transfected muscle, the R-BR, as well as surrounding and contralateral muscles.

Disturbances in the mean EMG amplitude were recorded in the R-BR of both animals following the virus injections. The changes in EMG output were not limited to the virus targeted muscle, but rather were also recorded in all muscles of the ipsilateral limb and even in muscles of the contralateral limb in Monkey Ma. The combinations of muscles with altered EMG signals differed in each limb investigated. In the right limb of Monkey Mi, the biceps, brachialis, FDS, ECR, EDC and BR all displayed variable deviations from baseline mean EMG, although the two week long increase recorded in the R-BR was the only change to pass the BH correction. The individual muscles displayed conflicting trends with reductions in mean EMG interspersed with increases. These variable trends in the individual muscles following the virus injections were recorded in both limbs of Monkey Ma. The mean EMG signals from the right deltoid, biceps, brachialis, FCR, FDS and BR and left deltoid, brachialis, and ECR increased or decreased at various intervals, with the R-FDS EMG first increasing before progressively decreasing.

Despite the individual muscle variability, when combined together to provide a score for the whole limb, similar trends were identified. While the direction of change was often reversed in the right arms of the two animals, the timeline of the changes was relatively conserved. In the experimental right limb of both animals, changes in more than one muscle first occurred six and eight weeks after the virus injections in Monkey Ma and Mi. During the first four months after the virus injections, the average EMG was variable, however after this time point a clear pattern was revealed. In the right arm of both animals, at 19 and 21 weeks for Monkey Ma and Monkey Mi respectively, limb wide changes became evident. Interestingly, the EMG did not progressively increase or decrease from this time point but rather changes were broken up into distinct periods. Three or four phases were identified in both animals, the latter two displaying the greatest temporal conservation. These latter

two phases were separated by a two to three week return of mean EMG to baseline. Interestingly, the direction of change in the first phase of the two animals differed, with the limb-wide mean EMG increasing in Monkey Mi and decreasing in Monkey Ma. Monkey Ma displayed this phasic reduction in mean EMG in both the left and right arms, with a one week delay in the onset of changes in the left arm as compared to the right.

The phasic change recorded in this study may be indicative of compensatory re-innervation, in which spared MNs increase their branching in order to supply muscle fibres which have lost their spinal innervation (Martineau et al., 2018). During this process of reorganisation it is possible that we may see phases of obvious change interspersed with periods of relative normalisation (Hansen and Ballantyne, 1978, Bromberg et al., 1993). The continuation of this phasic pattern up until the termination of the study may indicate that a degenerative process was ongoing at this time.

These changes, occurring within two weeks of one another in the experimental arms of the two animals, and with a one week delay for the left arm of Monkey suggest a system wide disturbance and similar trajectory of disorder occurring throughout the whole system of the two animals. The identical reduction in EMG in the left and right arms of Monkey Ma indicated the development of a simultaneous impairment. The difference in the direction of change recorded during the initial period in Monkey Mi is an important consideration, however the corresponding timeline to that seen in Monkey Ma suggests a comparable mechanism of action was occurring. It is possible that the nerve injury sustained by Monkey Mi prior to the virus injections lead to the altered outcome during the first period. If a degree of denervation had occurred due to this injury, it is possible that some MNs and the muscle fibres they innervate were already impaired. If this injury led to an irregular loss or reorganisation of MUs prior to the virus effects, the increase in mean EMG could be explained by altered amplitude cancellation or MU recruitment and rate coding (Day and Hulliger, 2001, Dideriksen and Farina, 2019).

The involvement of the whole limb, rather than just the injected muscle could provide evidence of some level of spread of TDP-43 related pathology to the motor pools of neighbouring muscles. The EMG changes do not seem to be limited to anatomically adjacent muscles, such as the ECR and FCR; functionally connected muscles, such as the other radial innervated extensor muscles; or to muscles known to have more CM input (McKiernan et al., 1998). Presumably the variability in task performance and adaptation to

mounting impairment in combination with possibly varied pathology contribute to the differences recorded at the individual muscle level. Changes were recorded in each muscle in at least one of the analysed limbs, therefore there was no clear sparing.

A larger negative Z score associated with the two phases of reduction recorded in the right arm of Monkey Ma was indicative of the fact that more muscles displayed changes in this limb than in the left. If these changes were in fact due to the spreading of TDP-43 pathology, these results could indicate that the pathology was able to propagate more rapidly to motor pools ipsilateral to the virally transfected pool than to others on the contralateral side of the cord. Again, the factors which led to the preference of particular muscles in the left limb is unclear. Only the deltoid, brachialis and ECR displayed individual changes in this arm, although none passed the BH correction individually.

It has been well documented that as force generated by a muscle increases, so too does the EMG signal (Moritani and Muro, 1987). Interestingly, the torque produced by the animals did not follow the same trends as recorded in the EMG. A progressive decline in torque was recorded in the right arm of Monkey Mi and left arm of Monkey Ma, however no significant changes were recorded in the right arm of Monkey Ma. The elbow flexion task used in this project, while specifically designed to activate the BR muscle, did not activate that muscle in isolation. We were unable to sample each muscle in the upper limb which may be involved in the task and it is possible that their compound activity masks the contribution of an individual muscle or selection of muscles in the generated force. Additionally, effects of training or small changes in posture may contribute to varying force levels exerted by each muscle, therefore the recorded torque should not necessarily be taken as a reliable measure of muscle or limb health in this case (Narici et al., 1996, Mogk and Keir, 2003, Roman-Liu and Bartuzi, 2013).

In this project, we were able to track the activity from eight upper arm muscles in order to identify any changing patterns as a result of a TDP-43 overexpression event in the right BR muscle. We identified a great deal of variability between muscles, but when taken in combination, limb wide trends were conserved between the transfected and control limb and even between the two animals. It is as yet unclear whether the changes recorded in the transfected muscle were in fact caused by pathological changes related to the TDP-43 overexpression, and in turn whether the limb-wide reductions in mean EMG were indicative of a spread of TDP-43 pathology to adjacent and distant spinal motor pools, or

perhaps as a result of disrupted processing within the spinal cord. The conserved timeline and phasic changes recorded in all three limbs provide compelling evidence for a shared pathogenesis in both animals.

# CHAPTER V. Validation of *in vivo* Measures of the Health of Spinal Motoneurons in NHPs

## Introduction

Accurately estimating the number of motor units (MUs) within a muscle is important to our understanding and assessment of the health of particular muscles during ageing and to characterise the progression of diseases such as MND. Since the development of the incremental counting technique (ICT) by McComas et al. (1971), used for collecting individual motor unit action potentials (MUAPs) to be used in the estimation of the number of MUs within a muscle, much work has been done to validate and advance the technique. The different variations of the motor unit number estimation (MUNE) technique all share a common theory based around the relationship between the maximal compound muscle action potential (CMAP) and an average motor unit action potential (MUAP). Collection of the CMAP is relatively straightforward, and involves supramaximal stimulation of the nerve. MUAP sampling, on the other hand, poses various challenges to the researcher. Different techniques and methods for collecting samples of MUAPs have been utilised for MUNE analysis, both clinically and in research animals, however each pose their own unique challenges for the researcher.

MUAPs can be sampled either via needle EMG, a laborious process which yields relatively few MUAPs, or more often in recent times by surface EMG electrodes. Individual bipolar electrodes and also high density surface EMG (HD-sEMG) electrode grids are used for the collection of the MUAPs and also the CMAP, elicited through supramaximal stimulation of the nerve proximal to the muscle. MUAP amplitudes are classically collected for MUNE analysis by multiple point stimulation (MPS) in which the nerve is stimulated at various points along its length. A low current is used in order to facilitate the detection of individual MUAPs, rather than clusters which fire at similar thresholds. The stimulation intensity is held constant until MU alternation has been ruled out in order to confirm the presence of only one active “all or none” MUAP, rather than a combination of MUs with overlapping depolarisation thresholds (DeForest et al., 2018). This process is repeated at multiple positions along the nerve until normally over 10 MUAPs are recorded at each site (McComas et al., 1971). The extensive sampling required along the length of the nerve limits this protocol to the more distal muscles, as the nerves are more easily accessible for

stimulation. When grid electrodes covering the surface of the muscle over the skin are used, MUAP identification and week-week tracking can be improved by the spatiotemporal 'fingerprint' of the MUAP. Each MUAP is shown to display individual characteristics, enabling their separation and decomposition from other MUAPs active at similar stimulus intensities (van Dijk et al., 2008, Peng et al., 2016).

Not only are these MPS or ICT techniques extremely time intensive, as well as invasive and uncomfortable when sampling is performed with a needle EMG, but studies have shown results to differ session to session due to differences in limb posture, making tracking of individual MUs rather challenging. The nature of the collection and MUAP isolation technique limits the sampling to lower threshold units with smaller amplitudes, potentially biasing any subsequent MUNE analysis. Furthermore, the introduction of any voluntary activity during the recording of the MUAPs prevents their identification (Maathuis et al., 2008, Boekestein et al., 2012).

Several research groups have worked to validate MUNE analysis using MUAPs decomposed from voluntary activity recorded while participants produce a range of set forces. The decomposition methods used in these studies allow for the detection of a wider range of MUAPs, including higher threshold units. These techniques are better able to isolate superimposed MUAPs than the incremental counting or multiple point stimulation methods which require MUAPs to be active in relative isolation. However, the results from these studies indicate that as the force produced increases, so too do the MUAP amplitudes sampled. The temporal-based decomposition algorithms are less able to detect the low amplitude MUAPs as the force produced increases, leading to a reduction in the representativeness of the MUAP sample (Peng et al., 2016). Higher forces therefore interfere with the MUNE, producing underestimations of the MU number (Boe et al., 2005).

More recently, a further method introduced by Nandedkar et al. (2004) removes the need for the stimulation and sampling of multiple MUAPs. The motor unit number index (MUNIX) gives reproducible results in healthy participants (Neuwirth et al., 2011) and has also been shown to detect MN degeneration as reliably as MUNE in MND patients, and in fact was more sensitive to MN loss (Boekestein et al., 2012, Neuwirth et al., 2015, Nandedkar et al., 2011). This approach is much faster than that of MUNE, and relies on the CMAP and surface interference potentials (SIPs) recorded while participants perform set movements at varying percentages of maximal contraction. An approximation of the

number of MUs contributing to the SIPs and CMAP is performed by a mathematical model (Nandedkar et al., 2010, Nandedkar et al., 2004).

The CMAP amplitude and area itself can provide information regarding the health of the muscle. The amplitude of the CMAP is lower in MND patients than in healthy controls (Argyriou et al., 2006), and these decreases have been shown to correlate with decreases in strength, as evaluated by the medical research council strength grade scale (de Carvalho et al., 2018). Additionally, the shape of the CMAP stimulus-response curve, referred to as the CMAP scan by Maathuis et al. (2013), has been used to track the advancement of disease in MND patients, with changes in amplitude and the appearance of ‘steps’ or breaks in the curve representing the loss of motor units and involvement of compensatory reinnervation. Recent work, however, has shown CMAP amplitude to be a less sensitive measure of MU health than MUNE and MUNIX techniques which are able to identify subtle changes in MU number prior to abnormalities in the CMAP amplitude (Gunes et al., 2021) and also have identified a sharper decline than that of the CMAP during progression of MND (Felice, 1997, Boekestein et al., 2012).

There is conflicting evidence for the use of the CMAP amplitude in tracking disease related changes. The amplitude of the CMAP is influenced by compensatory re-innervation which takes place alongside the MU degeneration occurring during MND and may contribute to the unreliability of this measure clinically, when tests occur fairly infrequently (Mccomas et al., 1971). It is possible that more regular collection of the CMAP amplitude may shine a light on this degeneration and re-innervation as it occurs. de Carvalho et al. (2018) have calculated a ‘Neurophysiological Index’, incorporating a number of measures related to motor conduction known to be involved in MND, including the CMAP amplitude but excluding MUNE or MUNIX. This index declines comparably to mean-MUNIX values in pre-symptomatic limbs of patients with MND, showing that the CMAP amplitude may be especially useful when looked at in combination with other factors of motor conduction (Escorcio-Bezerra et al., 2017). The benefit of using the CMAP amplitude either in isolation or within the Neurophysiological Index is that it is much less time consuming than multiple point stimulation or incremental counting technique MUNE, and unlike MUNIX, can be performed easily on muscles in late stages of disease where voluntary contractions can be difficult to produce.

While validation is on-going for the variations of the MUNE technique, there are hopes that in time they will be developed into lower motor neuron degeneration biomarkers (Benatar et al., 2016). Different methods may provide starkly different MUNE values, due to their individual technical limitations and biases. Without the knowledge of the true number of MUs to expect in these muscles it is difficult to verify the estimated numbers generated from these tests.

Understanding and monitoring changes in MU number in animal models of MND will be very important for the understanding of this complicated disease and for the development and testing of future therapeutic interventions. Various incremental counting and multiple point stimulation MUNE techniques have been trialled in rodent models of MND, confirming results seen in MND patients, for example that the MUNE values begin to decrease at an early stage in the course of disease, in some cases predicting disease onset (Shefner et al., 1999, Shefner et al., 2006). To our knowledge, no MUNE analysis has been performed in NHPs who share markedly similar neuromusculature to humans. In this project, we employed an adapted MUNE technique and tracked the MUNE values and the CMAP amplitude over the course of seven months in two NHPs virally induced to overexpress the protein TDP-43 in the spinal motoneurons which supply the right brachioradialis muscle. These assessments were used in order to validate and compare their *in vivo* applicability as a measure of MU health in a NHP model of MND.

## **Methods**

### ***Animals***

Recordings were performed from two adult female awake behaving Monkeys (*M. mulatta*; Monkeys Mi and Ma, age 6, weight 6.2 and 6.7 kg respectively). All animal procedures were performed under appropriate licences issued by the UK Home Office in accordance with the Animals (Scientific Procedures) Act (1986) and were approved by the Animal Welfare and Ethical Review Board of Newcastle University.

See General Methods for details regarding the isometric hold task, surgical preparation and details of virus administration and vector contents.

### ***Electrophysiological Recordings***

Recordings were made from pairs of intramuscular electromyography (EMG) electrodes implanted in two muscles supplied by the median nerve (FCR and FDS) bilaterally, and three muscles supplied by the radial nerve (extensor carpi radialis (ECR), extensor digitorum communis (EDC) and brachioradialis (BR)) bilaterally. Additional recordings were made from the brachioradialis muscle using a high-density surface EMG grid (GR04MMI305, OT Bioelettronica, Turin, Italy) with 64 electrodes (spacing 4mm). A bi-adhesive foam strip with holes aligned to the matrix was placed on the grid, and the holes filled with conductive paste (CC1, OT Bioelettronica, Turin, Italy). This assembly was then stuck to the skin over the muscle. To ensure good skin contact the forearm was shaved and cleansed with alcohol wipes. The location of the grid on the skin was marked each day with permanent marker pen to ensure reproducible placement from session to session. Standard surface adhesive electrodes (Neuroline 720; Ambu A/S, Ballerup, Denmark) were placed over the flexor and extensor tendons at the wrist to act as reference and ground for the surface grid. One of the unused nerve cuff electrodes was used as the ground for the intramuscular electrodes. The surface grid electrode was connected to a custom printed circuit board containing a 64-channel amplifier (gain 192; bandwidth 30Hz - 2 kHz) and an analogue-to-digital convertor (RHD2164; Intan Technologies LLC, Los Angeles, CA, USA). The intramuscular EMG electrodes were connected to a second analogue-to-digital converter (Intan Technologies) via a connector mounted onto the headpiece. Digitized signals were sent over a serial peripheral interface (SPI) cable to an RHD USB interface board (also Intan Technologies). This allowed data to be captured to a computer hard disc (5 kSamples/s) along with the elbow torque signal and digital markers signalling the phases

of task performance and stimulus timing. Voluntary brachioradialis activity was recorded from the intramuscular and grid electrodes during performance of the behavioural task. Involuntary contractions were recorded by the intramuscular electrodes and the grid electrode during the nerve stimulation protocol.

### ***Nerve cuff stimulation and recording***

Bipolar current pulses (0.2ms per phase) were delivered through the three contact radial and median cuffs with a bi-phasic constant current isolated stimulator (Model DS4, Digitimer, Hertfordshire, UK). A focal stimulus was delivered by shorting the first and third contacts and stimulating relative to the second contact. Stimulus current was delivered at supramaximal intensity to elicit a maximum M-wave and ramped down in decrements of 0.1 $\mu$ A until it was below threshold intensity. Left and right arms were stimulated in different sessions, following recordings of the motor task. Monkeys were gradually acclimated to the full length nerve stimulation protocol. No adverse behavioural effect to the radial and median nerve stimulation was recorded in either animal, however restlessness was noted during longer stimulation studies.

### ***Compound Muscle Action Potential (CMAP)***

During radial and median nerve stimulation, the intramuscular electrodes collected the M-wave at each stimulus intensity from the implanted muscles. The peak-peak amplitude of the CMAP was collected to produce CMAP amplitude plots, which were used to assess qualitatively the health of the stimulated muscle. An average was taken of the maximal CMAP amplitude recorded during the plateau period at supramaximal intensity (Figure 5.1B). This average maximum CMAP amplitude was tracked over the course of the project. In the case of radial stimulation, the HD-sEMG grid simultaneously collected the surface M-wave from the BR muscle. The CMAP amplitude was measured for each grid electrode as previously described. The maximum CMAP amplitude per electrode was used for MUNE analysis. The CMAP amplitude from each grid electrode was averaged to provide a mean grid CMAP amplitude per session. The maximal CMAP amplitude from each session was compared against a mean CMAP amplitude collected during a baseline period (shaded in grey in Figure 5.2 – 5.5). Baseline sessions were collected prior to the injection of the viruses for Monkey Ma (10 sessions for radial innervated muscles, 5 sessions for median innervated muscles), however due to the injury sustained to Monkey Mi's right radial nerve, the first 10 sessions collected after recovery from this injury contributed to

the baseline, some of which were collected in the weeks immediately following the virus injections.

In each session, any electrode channels poorly connected to the skin showing a poor signal to noise ratio were excluded from further analysis.

### ***Motor unit decomposition***

Motor unit decomposition was performed on EMG signals recorded from the HD-sEMG grid using techniques previously described by our lab in collaboration with colleagues at Imperial College London and Friedrich-Alexander-Universität Erlangen-Nürnberg (Del Vecchio et al., 2022). Briefly, HD-sEMG signals recorded from the brachioradialis during an isometric elbow flexion task were decomposed into individual MUAPs using a modified blind source separation protocol, adapted from (Negro et al., 2016), which utilises the unique 2D spatiotemporal features, or fingerprint, of each MUAP to identify their individual firing times. This decomposition technique has been used previously for the tracking of individual MUs across multiple sessions spanning one month, recorded while two NHPs perform an isometric elbow flexion task (Del Vecchio et al., 2022). Spike-triggered averaging used the MU firing times as triggers to aid in the validation of the decomposition, and to align the MUAPs temporally. Scripts for decomposition analysis were provided by Prof Alessandro Del Vecchio.

The number of MUs decomposed during the task performance was recorded for each electrode per session. The trigger-aligned MUAPs were averaged per electrode to provide an average MUAP pattern across the grid. The peak-peak amplitude of the average MUAP was measured and used for later MUNE analysis.

### ***Motor unit number estimation (MUNE)***

The MUNE calculation followed the protocol proposed by (van Dijk et al., 2008). The MUNE value for the grid was calculated using Eq (5.1):

$$MUNE = \sum_i w(i) \frac{CMAP(i)}{\text{mean MUAP}(i)} \tag{5.1}$$

where  $\text{CMAP}(i)$  and  $\text{mean MUAP}(i)$  are the peak-peak amplitudes of the CMAP and mean MUAP recorded from the  $i$ 'th channel. The weight function  $w(i)$ , described in Eq. (5.2), weights the channel-by-channel MUNE values so as to account for differences in amplitude.

$$w(i) = \frac{\text{mean MUAP}^2(i)}{\sum_i \text{mean MUAP}^2(i)} \quad (5.2)$$

The MUNE value for each session was tracked over time for each animal, along with the average MUAP and maximal grid CMAP peak-peak amplitudes. This analysis was performed on the left and right BR muscle of Monkey Ma, but only the right BR of Monkey Mi as she was unable to learn the task with her left arm. These measures were compared against a mean MUAP amplitude and CMAP amplitude collected from a series of baseline sessions. All baseline sessions for Monkey Ma were collected prior to the virus injections, while for Monkey Mi, as before, baseline sessions were collected following the nerve injury recovery, with some sessions collected in the weeks following the virus injections. Baseline sessions are displayed under the grey shaded block in Figure 5.2 – 5.5.

### ***Statistical analysis***

All data and statistical analysis was performed offline using custom scripts written in the MATLAB environment (R2020a, MathWorks). Paired t-tests were performed on all measures against their respective baseline periods. Any results that reached the alpha significance level, set as 0.05, were marked with black markers in subsequent plots. The Benjamini Hochberg (BH) procedure was performed for each muscle, and also for each MUNE related measure, to correct for false positives discovered with the use of multiple comparisons (Benjamini and Hochberg, 1995), and any sessions which passed the BH correction were marked in red.

## Results

### *Compound Muscle Action Potential (CMAP)*

Compound muscle action potentials (CMAP) were collected from chronically implanted intramuscular EMG electrodes in eight upper limb muscles, bilaterally, and tracked weekly for approximately seven months following the viral targeting of motoneurons innervating the right brachioradialis muscle. Figure 5.1A displays an example of the M-waves recorded from the intramuscular right BR (R-BR) electrode of Monkey Ma from each stimulus intensity in a baseline session. The peak-peak amplitude from each stimulus was measured and plotted, displaying the sigmoid-like curve, characteristic of healthy muscles (Figure 5.1B). The maximal CMAP amplitude was derived from an average of the supramaximal values from the flat portion of the sigmoid curve. Nine weeks after the injection of a combination of viral vectors designed to target and transfect the spinal motoneurons (MNs) supplying the R-BR, the stimulus-response CMAP scans of this muscle began to display a stepped appearance such as is often seen in MND patients, and thought to be indicative of MU loss (Figure 5.1C) (Maathuis et al., 2013). This stepped appearance was intermittently present in scans collected from the R-BR for the duration of the project. The size and pattern of the steps frequently changed, presumably due to the compensatory reinnervation. The steps appeared in the R-ECR muscle one month after the R-BR, and in fact became very pronounced in the last month of the project. The CMAP scans of the L-BR, and particularly the L-ECR and L-EDC also began to exhibit the stepped appearance at a similar time to the R-ECR.

Monkey Mi suffered a nerve injury prior to the injection of the AAVs, which caused a much more marked and obvious appearance of steps in the CMAP scan. This stepped appearance recovered over the course of six weeks, at which point we began the investigation phase of the project by injecting the viral vectors (Figure 5.2A). This stepped pattern re-appeared in the R-BR of Monkey Mi, one month after the virus injection (Figure 5.2B), and while the location and appearance of the steps changed regularly, their presence remained throughout the extent of the project (Figure 5.2C-F). Steps were also present in the CMAP scans recorded from the L-BR in Monkey Mi two months after the virus injections, however they were much less pronounced.

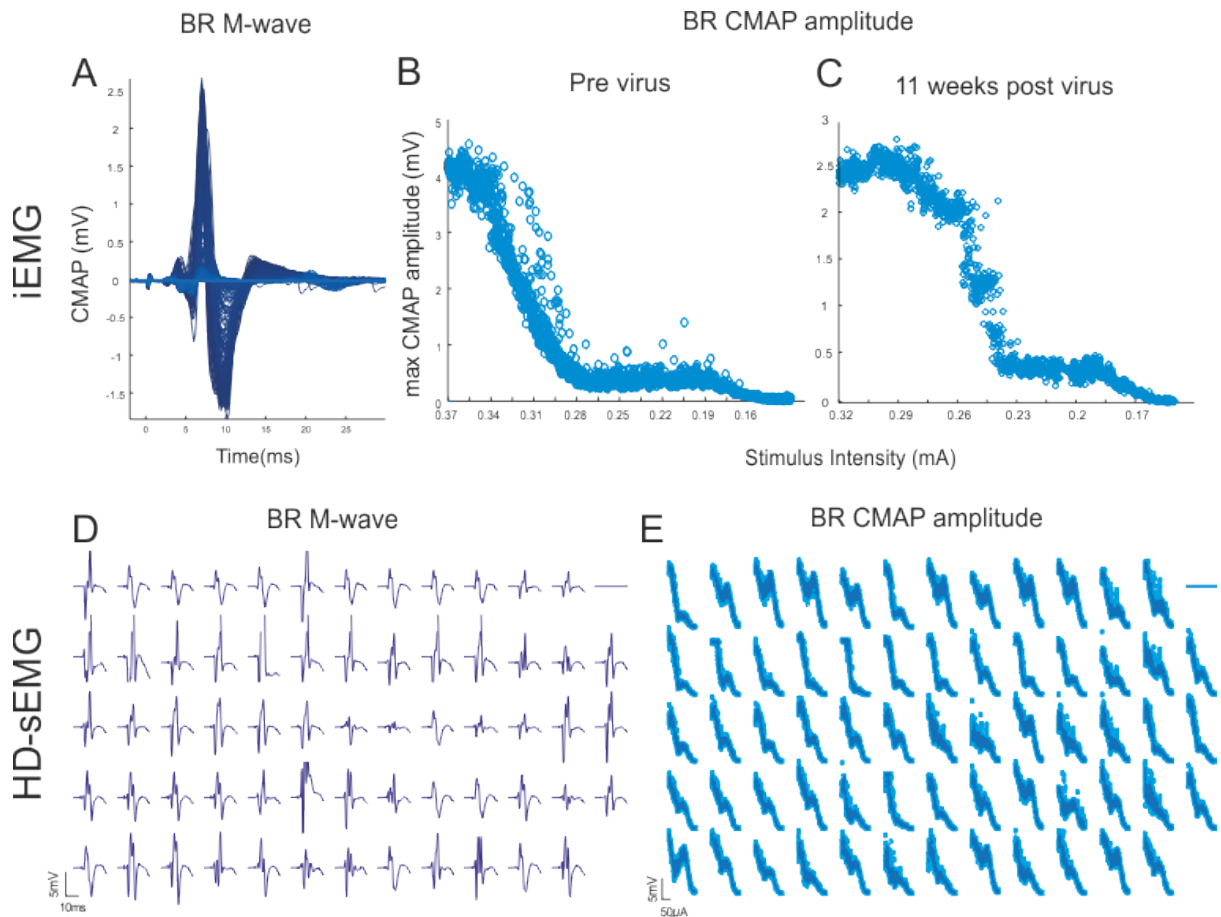


Figure 5.1. A series of decremental M-waves, elicited from median and radial innervated muscles of the forearm were used to assess the health of the muscles in a NHP model of MND. (A) An example series of superimposed M-wave responses recorded from a chronically implanted EMG electrode in the right BR of monkey Ma. (B) The peak-peak amplitude of the CMAP at each stimulus intensity was used to generate the CMAP scans, with maximal CMAP amplitude of each response plotted against stimulus intensity. In healthy muscles, the CMAP scan has the appearance of a sigmoid-like curve. Prior to the injection of the AAV vectors, the scans collected from the R-BR of monkey Ma showed this continuous, sigmoidal shape, however nine weeks after the virus injections a series of breaks or steps became evident in the curve (C). This stepped appearance is characteristic of the CMAP scans of patients with MND (Maathuis et al., 2013). (D) Simultaneous to the intramuscular recordings, a HD-sEMG electrode grid placed over the skin covering the BR muscle recorded surface signals. The CMAP is recorded at each electrode site across the grid, adding spatiotemporal information. (E) The peak-peak amplitude was measured as before, giving CMAP amplitude scans for each contact. D and E refer to an example set of grid recordings from monkey Ma, prior to virus injections. No stepped appearance was present in the CMAP amplitude collected from the grid at any point during the duration of the project for monkey Ma, but steps did appear in the surface CMAP scans collected from the R-BR of monkey Mi one month after the virus injection (Figure 5.2).

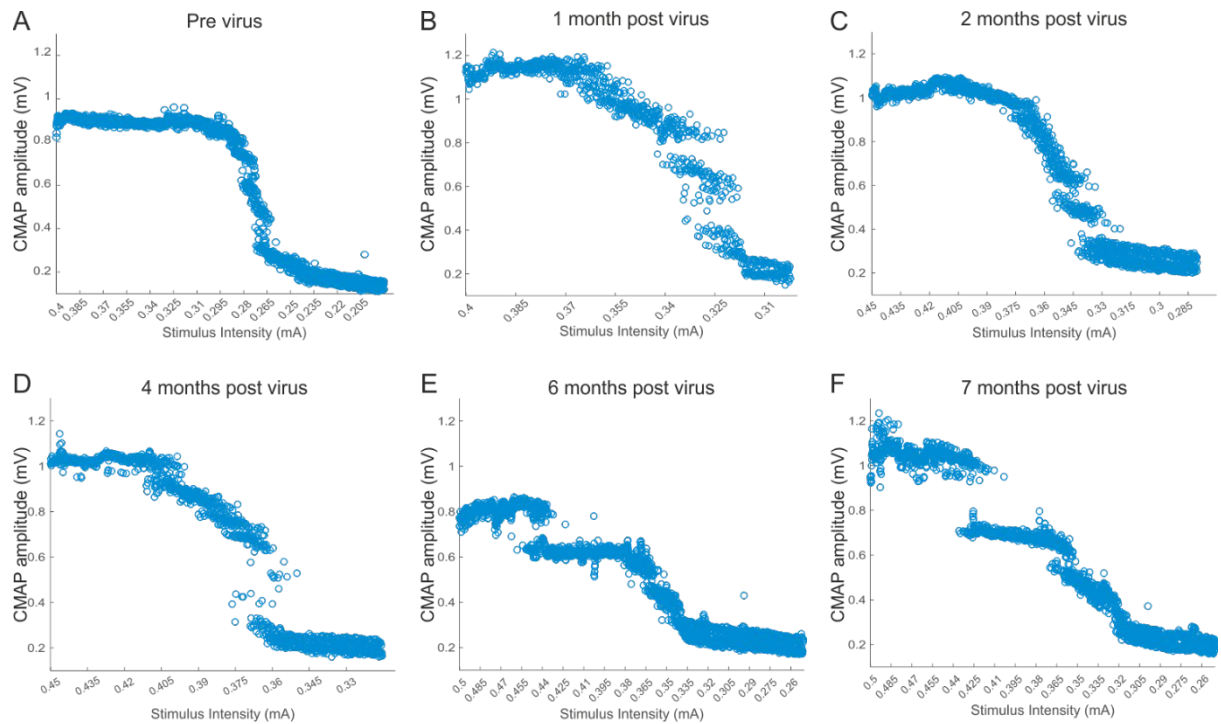
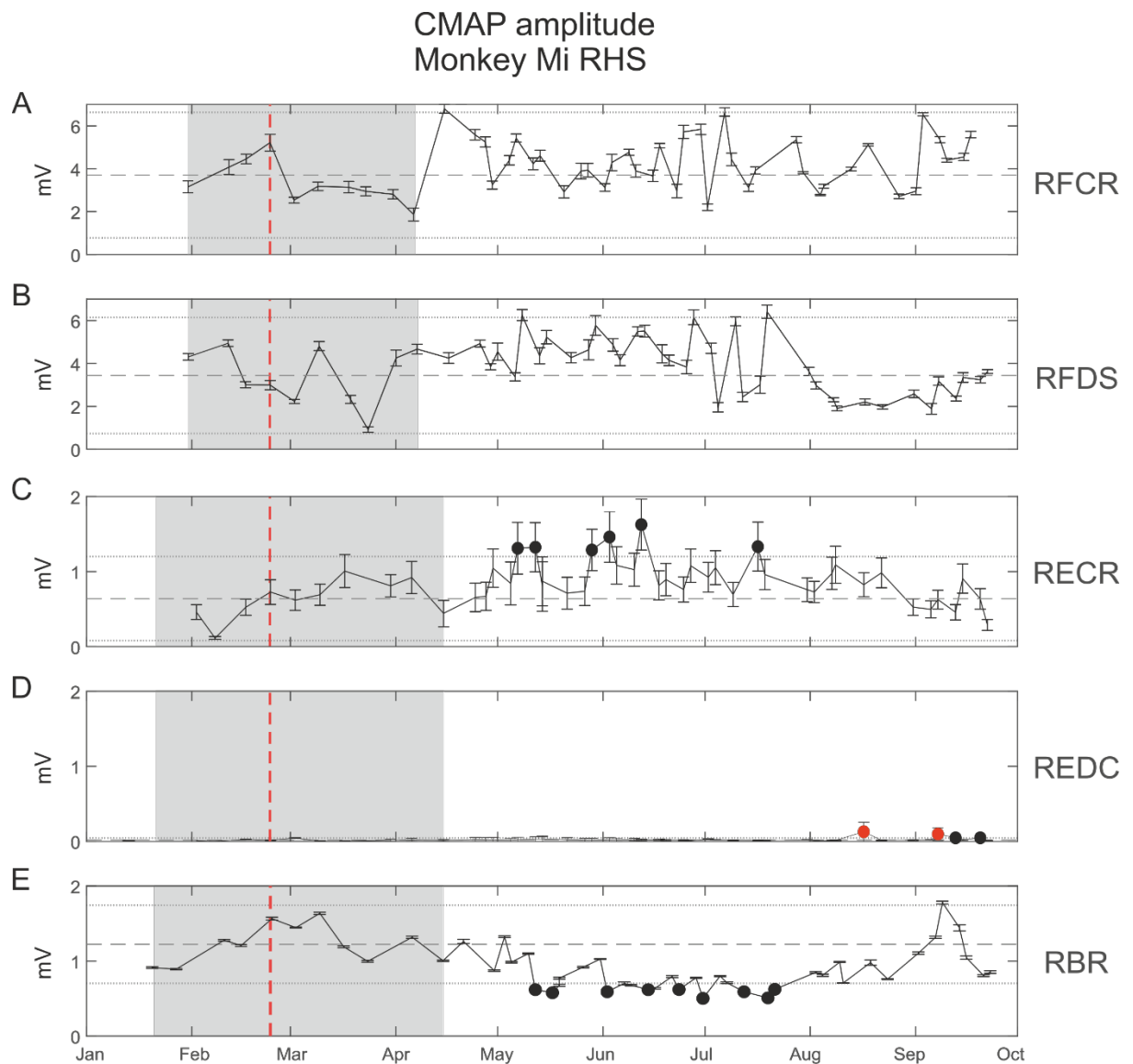


Figure 5.2. CMAP scans collected from the R-BR muscle of Monkey Mi displayed a stepped appearance, characteristic of CMAP scans collected from MND patients. (A) Six weeks after the accidental nerve injury, and immediately prior to the virus injections, the CMAP scans collected from the R-BR of Monkey Mi appeared sigmoidal in shape. (B) Clear steps in the CMAP scan emerged one month after the virus injections, indicating the occurrence of MU remodelling (Maathuis et al., 2013). The position of the steps, as well as the maximum CMAP amplitude were noted to regularly change during the seven months of recording following the virus injections (C-F).

The peak-peak CMAP amplitude of each muscle was measured each week for the duration of the project, which spanned the baseline period and a seven month intervention phase once the viruses designed to transfect the BR spinal MNs had been injected. No change in the peak-peak amplitude of the CMAP was recorded in the two flexor muscles studied in both the right and left arms of Monkey Mi (Figure 5.3A, B; Figure 5.4A, B). The CMAP amplitude recorded from the R-BR of Monkey Mi decreased twelve weeks after the virus injections and remained so for eleven weeks, before returning to within baseline limits ( $P<0.05$ ) (Figure 5.3E). During this reduction noted in the R-BR, the amplitude of the R-ECR CMAP increased intermittently ( $P<0.05$ ). After the same length of time, it also normalised (Figure 5.3C). Neither of these changes in the CMAP amplitude passed the BH correction for multiple comparisons. The CMAP amplitude of the R-EDC remained very low ( $<200\mu\text{V}$ ) for the duration of the study (Figure 5.3D). It is possible that the nerve fibres supplying this muscle were the most damaged during the radial nerve injury sustained by Monkey Mi during a cuff implantation surgery. In fact, the CMAP amplitudes for each of the radial innervated muscles in the right limb were much lower than those recorded from the left limb (Figure 5.4C-E), suggesting a long lasting impact of the injury.

The CMAP amplitude of the L-BR muscle in Monkey Mi interestingly also decreased in the same week as the R-BR ( $P<0.05$ ) (Figure 5.4E). This reduction lasted the duration of the recording period. The CMAP amplitude of the L-EDC was variable, with significant fluctuations from baseline recorded both prior to and during the decrease noted in the R-BR (Figure 5.4D). The first of these increases passed the BH correction for multiple comparisons. No differences in CMAP amplitude were recorded in the other muscles sampled in the left arm.



*Figure 5.3. Tracking the intramuscular peak-peak CMAP amplitude in the right forearm of monkey Mi. (A,B) The CMAP amplitude of the median innervated flexor muscles did not change during the project. The baseline period is indicated by the grey shaded box and the time point of the virus injections, which were designed to induce an overexpression of TDP-43 in the right brachioradialis (R-BR), is indicated by the red dashed line. (C) The CMAP amplitude in the R-ECR increased 12 weeks after the virus injections and remained elevated for a further 11 weeks ( $P < 0.05$ ). These increases reached alpha significance, but did not pass the BH multiple correction test, and so are marked in black. Results which passed the BH test are marked in red. (D) Only a very low response was recorded from the R-EDC during the project. It is likely that the nerve fibres supplying this muscle were unable to recover following the nerve injury sustained by this animal. (E) The CMAP amplitude recorded from the R-BR muscle declined at the same time as the increase was recorded in the R-ECR. This reduction was sustained for 11 weeks ( $P < 0.05$ ). The dashed line indicates the baseline mean, and dotted lines 2 standard deviations (SD) of the baseline.*

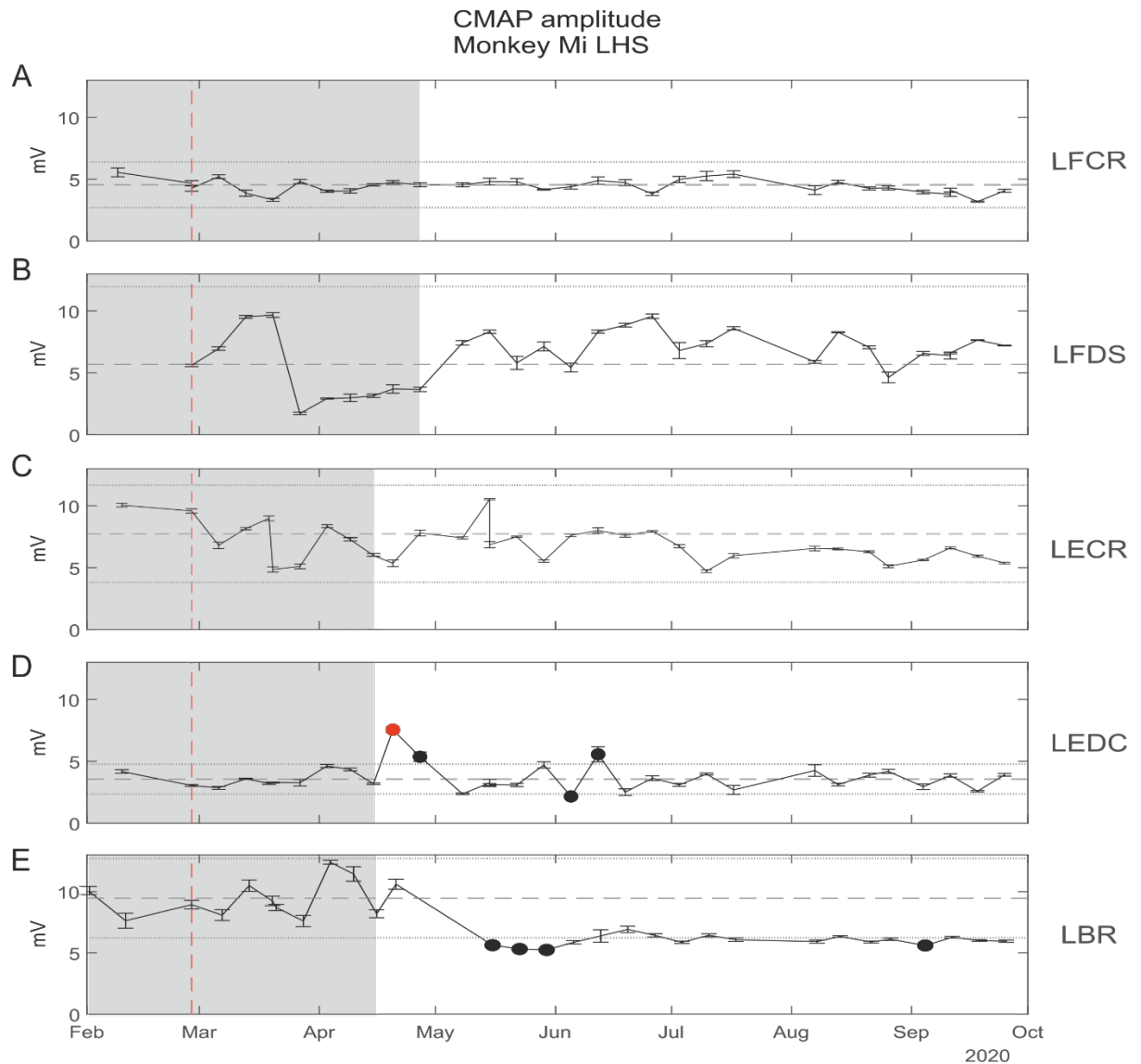


*Figure 5.4. Tracking the intramuscular peak-peak CMAP amplitude in the left forearm of monkey Mi. (A,B) The CMAP amplitude of the median innervated flexor muscles did not change during the project. The baseline period and time point of injection are represented as in Figure 5.3. (C) No change in the CMAP amplitude of the L-ECR muscle was recorded during the project. (D) The CMAP amplitude of the L-EDC was variable, with significant fluctuations from baseline recorded both prior to and during the decrease noted in the R-BR. The first of these increases in the L-EDC CMAP amplitude was the only to pass the BH test for multiple comparisons (marked in red). The points that did not pass the BH test but reached the alpha level are marked in black. (E) A decrease in the CMAP amplitude of the L-BR was recorded at the same time as occurred in the R-BR, however this decrease was sustained for the duration of the project, with four sessions reaching the alpha significance level. The dashed line indicates the baseline mean, and dotted lines 2 SDs of the baseline.*

The intramuscular peak-peak CMAP amplitude was measured and tracked in the same way in Monkey Ma. No changes were detected in the R-FCR muscle, but as the project progressed, increasing fluctuations were recorded in the R-FDS, with both increases and decreases in CMAP amplitude passing BH correction (Figure 5.5A, B). The CMAP amplitude from the R-ECR and R-EDC radially innervated muscles increased from early in the intervention stage of the project, and prior to any recorded changes in the R-BR (Figure 5.5C-E). The R-EDC CMAP increased shortly after the virus injections and remained elevated for the entirety of the project. The CMAP amplitude of the R-ECR primarily increased during the study, however a two week long reduction was recorded nineteen weeks after the viral targeting of the R-BR muscle. After this period, the CMAP amplitude again increased beyond the baseline amplitude. The R-BR CMAP amplitude did not increase above baseline levels at any point during the project, and instead three distinct periods of reduced amplitude were recorded, each of which passed the BH correction for multiple comparisons. The first of these reductions in amplitude occurred eleven weeks post virus injections and endured for two weeks. A further decrease occurred six weeks later and lasted for four weeks. The second reduction in occurred at the same time as the R-ECR CMAP amplitude reduced. During this time, the amplitude of the R-EDC also decreased from its elevated state back within baseline limits, though it quickly recovered.

The median innervated muscles sampled in the left limb of Monkey Ma remained unchanged for the approximately seven months in which they were recorded from (Figure 5.6A, B). In contrast to this, the CMAP amplitudes collected from the L-ECR and L-EDC, similar to the contralateral limb, increased well beyond the amplitudes recorded before the injection of the viruses targeting the R-BR MNs (Figure 5.6C, D). The amplitude of the CMAP recorded from the L-ECR increased six-fold in comparison to the baseline recordings. The CMAP amplitude recorded from the L-BR was more variable, with both increases and a decrease in amplitude recorded (Figure 5.6E). These changes in amplitude did not meet the threshold for significance set by the BH correction, unlike the other two radially innervated muscles sampled. The decrease in L-BR CMAP amplitude did however occur within the second reduction of amplitude recorded in the R-BR.

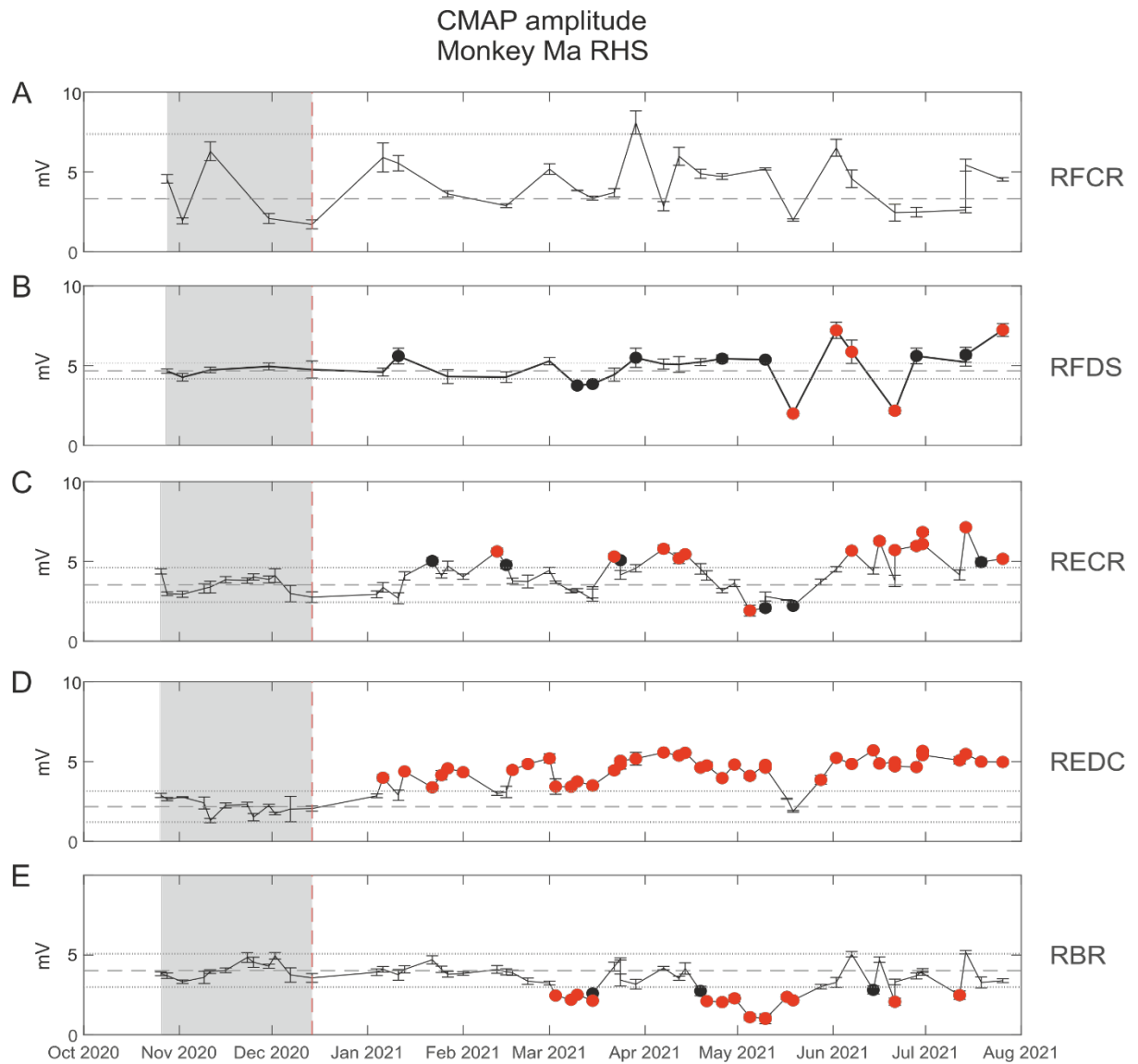


Figure 5.5. Tracking the intramuscular peak-peak CMAP amplitude in the right forearm of monkey Ma. (A) The CMAP amplitude recorded from the R-FCR muscle did not change over the course of the project, however increasing fluctuations were recorded in the R-FDS, with both increases and decreases in CMAP amplitude passing BH correction (marked in red) (B). The points that did not pass the BH test but reached the alpha significance level are marked in black. The baseline period and time point of injection are represented as in Figure 5.3. (C, D) The CMAP amplitude recorded from both the R-ECR and R-EDC became elevated 4 and 3 weeks after the injection of the AAV viruses, and remained higher than the baseline period with an exception of a 3 week period in which the R-ECR CMAP amplitude became significantly smaller than the baseline CMAP and the R-EDC dropped back into the baseline range. (E) The CMAP amplitude recorded from the R-BR was decreased in three independent periods, each of which passed the BH correction. In these graphs, the middle dashed line represents the mean baseline CMAP amplitude, and the lines on either side display 2 standard deviations of the baseline mean, and dotted lines 2 SDs of the baseline.

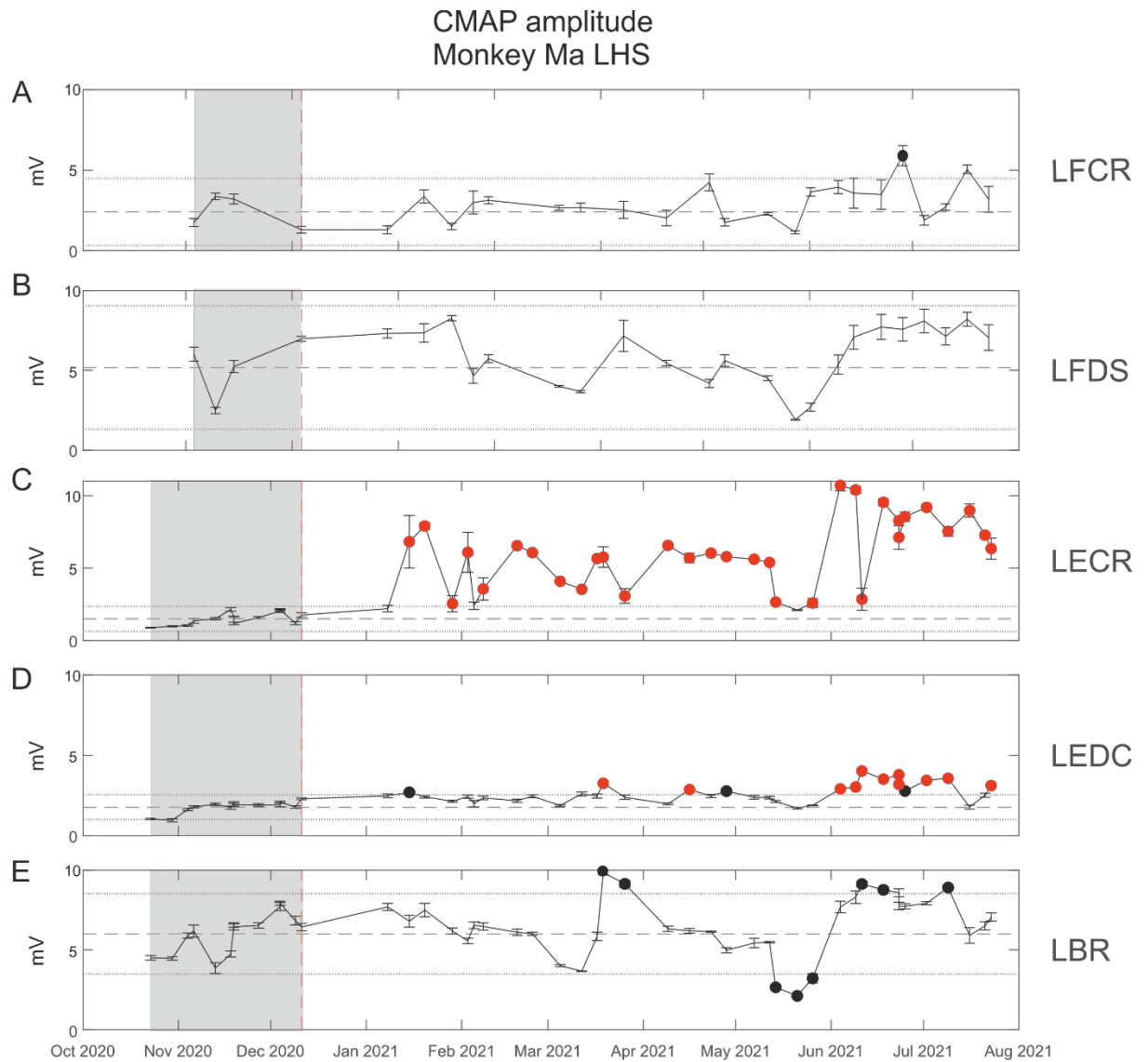


Figure 5.6. Tracking the intramuscular peak-peak CMAP amplitude in the left forearm of monkey Ma. (A, B) The CMAP amplitude recorded from the flexor muscles did not change from baseline, with the exception of one session, 6 months after the virus injections where the L-FCR CMAP amplitude increased ( $P < 0.05$ ). The points that did not pass the BH test but reached the alpha significance level are marked in black, whereas those that successfully passed are marked in red. The CMAP amplitude recorded from the L-ECR and the L-EDC were significantly increased compared to their respective baseline periods, with their values passing the BH correction (C, D). They remained elevated for the entire project, at no point crossing below the baseline mean, indicated by the middle dashed line. The two lines on either side represent 2 standard deviations of the baseline mean. (E) The CMAP amplitude recorded from the L-BR was more variable, first increasing 3 months after the injection followed by a 2 week decrease 2 months later, and finally a further increase in amplitude ( $P < 0.05$ ). These changes did not pass the BH test for multiple comparisons. The dashed line indicates the baseline mean, and dotted lines 2 SDs of the baseline.

### ***Motor unit number estimation (MUNE)***

During the nerve stimulation protocol, a 64 channel HD-sEMG electrode grid simultaneously recorded the responses from the surface of the BR muscle (Figure 5.1C). The peak-peak amplitude was measured for each channel as before, and used to produce CMAP scan plots (Figure 5.1D). No stepped appearance was evident in the surface CMAP scans collected from Monkey Ma, or the left BR of Monkey Mi but was present in those recorded from the R-BR one month after the virus injections. Not every electrode across the grid displayed these changes, and the position of the affected electrodes was not stable over time. The average surface CMAP amplitude across the grid was tracked for the left and right BR muscles of both animals, while the maximal CMAP from each electrode contact was used for estimating the number of MUs in the muscle.

Individual MUAPs were decomposed from voluntary activity performed by the animals within a set force range. Figure 5.7A and B demonstrate a selection of the lower amplitude MUAPs (<800 $\mu$ V) active across the grid. The close up in panel B shows the entire sample of MUAPs recorded in that example channel, and clearly shows the variation in the amplitude of recorded MUAPs. The individual MUAPs active for each channel of the electrode grid were averaged, to generate a mean MUAP for each channel (Figure 5.7C, blue trace). The spatiotemporal profiles of the CMAP (red trace) and mean MUAP (blue trace), did not perfectly match, suggesting that the MUAP sample may not be representative for the entire muscle (van Dijk et al., 2008).

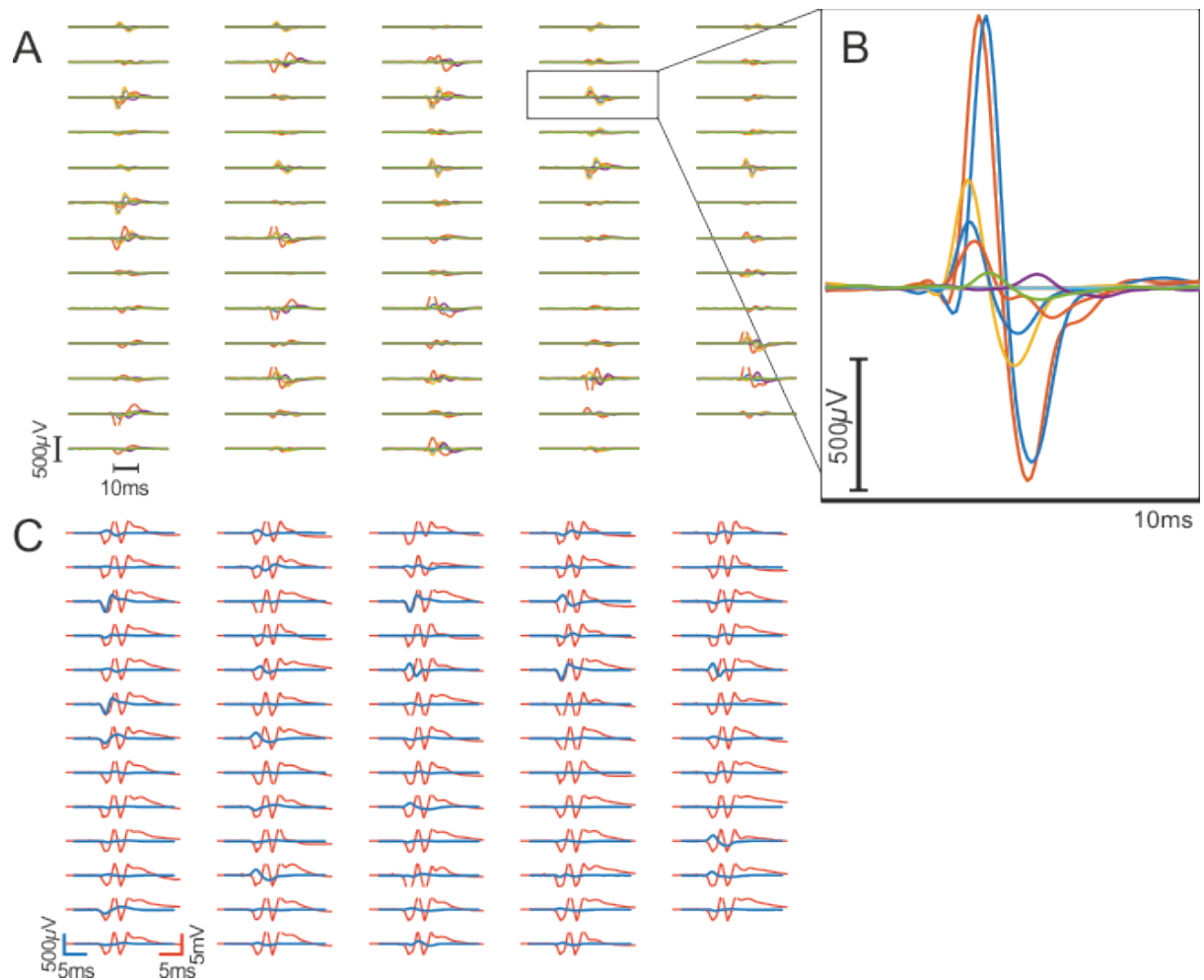


Figure 5.7. A modified decomposition protocol detected the individual MUAPs active during an isometric task performed by two NHPs. (A) A sample of decomposed MUAPs active in the 64 electrodes of a HD-sEMG grid recorded during an isometric elbow flexion task performed by monkey Ma. 2 high amplitude units ( $>800\mu V$ ) were excluded from this figure to improve clarity. 12 MUAPs were decomposed from the voluntary activity recorded during the task, all units, including the high amplitude units, are displayed in (B). (C) The MUAP (blue trace) and CMAP (red trace) were aligned and the scaled MUAP amplitude was divided into the CMAP amplitude for each channel. A weighted average was derived to give the motor unit number estimation (MUNE) for the total surface CMAP (see Eq (5.1) and (5.2)).

Decomposition spike-triggered averaging MUNE analysis was performed on the R-BR of Monkey Mi and both the L-BR and R-BR of Monkey Ma. As the MUAP decomposition method used in this study relied on HD-sEMG signals recording during voluntary activity, we were limited to the muscles which could be sampled. As such, we were unable to perform MUNE analysis on the control L-BR of Monkey Mi. There is evidence that different levels of force produced during voluntary contractions can impact the MUNE values, and so the animals were trained to perform the isometric task within a set force range (1.6-3.2 N.m) in order to standardise results (Boe et al., 2005). The mean MUAP signal from each electrode site was divided into the maximal CMAP for the respective channel, and appropriately weighted, using a formula proposed by van Dijk et al. (2008) (Eq. 5.1 and 5.2).

The accidental injury to the Monkey Mi's right radial nerve complicated the collection of baseline data due to strict time constraints. A group of ten sessions spanning the weeks immediately preceding and succeeding the virus injections was collected as baseline (marked by the grey shaded boxes). During this time, many fewer MUs were decomposed by the algorithm than in the months prior to the injury (marked by the blue shaded area), with only one MU identified in two of the baseline sessions (Figure 5.8A). The ongoing recovery following the radial re-innervation may contraindicate these sessions for use as a baseline. It is therefore relatively unsurprising that following a further six weeks, the number of decomposed MUAPs per session increased significantly and stabilised.

The average MUAP amplitude varied between 200-400 $\mu$ V prior to the accidental nerve injury. In the first four months following the nerve injury and subsequent virus injections, primarily small amplitude MUAPs were sampled and identified in the HD-sEMG signals from the R-BR by the decomposition algorithm for Monkey Mi, with the amplitude of the mean MUAP and the total range of MUAPs recorded <150 $\mu$ V (Figure 5.8B). Sixteen weeks after the virus injections the amplitude of the sampled MUAPs increased progressively. The mean MUAP amplitude remained elevated from this week until the end of the study, with the majority of these results passing the BH multiple comparison correction. The variability in the identified MUAPs also increased during this time, with amplitudes ranging from <40 $\mu$ V to >350 $\mu$ V.

The CMAP amplitude began to progressively increase the week after the virus injections, possibly due to the ongoing recovery of the radial nerve post injury (Figure 5.8C). Ten

weeks into the tracking phase of the project, post virus administration, the mean CMAP amplitude across the grid began to decrease, at which point it remained towards the lower end of the baseline values. While this decline did not reach significance, a clear trend can be seen. The decrease in the surface R-BR CMAP occurred in the same week as a reduction in intramuscular CMAP was recorded (Figure 5.3E).

The MUNE values calculated from the sessions at the outset of the experiment were very high, ranging from 237-426 in the baseline period (Figure 5.8D). At week ten, the MUNE value sharply decreased to <200, and within five weeks had progressively decreased to below 20. The MUNE did not then increase above 20 for the duration of the project. Each of the MUNE values following the ten week mark passed the BH test for multiple comparisons. The significant reduction in the MUNE first occurred in the same week as the downward trend in the surface CMAP amplitude became clear, and was followed closely by the increase in mean MUAP amplitude.

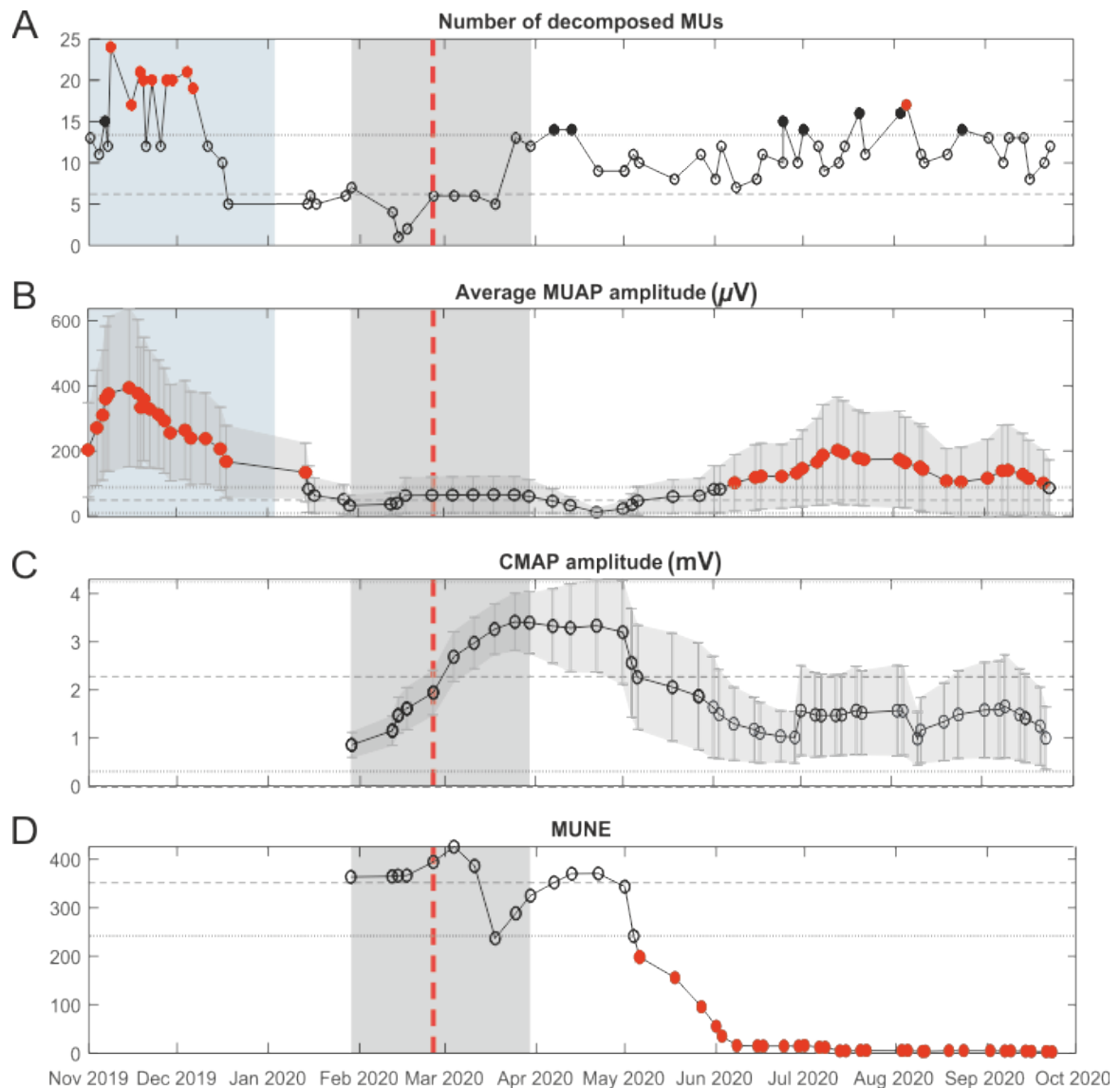


Figure 5.8. MUNE was calculated for the R-BR muscle of Monkey Mi from surface EMG signals recorded using a HD-sEMG grid. (A) The number of MUs decomposed during the isometric task was higher prior to the nerve injury ( $16 \pm 5$ ), indicated by the blue shaded area, than immediately after the injury. Due to time constraints, the baseline period was collected during the latter half of the animal's recovery from the nerve injury. Sessions immediately following the virus injections were added to this baseline period in order to compensate for the recovery time (grey shaded area). The number of MUs decomposed by the algorithm increased 6 weeks after the injections and remained elevated, however they were still fewer than the MUs decomposed prior to injury ( $11 \pm 3$ ). The increased numbers of MUs decomposed before and after the baseline period reached alpha significance level of 0.05 (marked in black), with 9 sessions prior to injury, and 1 session following the virus injections also passing the BH correction (marked in red). (B) The average MUAP amplitude was over  $200 \mu V$  for all session but one, prior to the nerve injury (blue shaded area). The range of MUs decomposed by the algorithm in the first 4 months post-injury were all low amplitude units ( $< 150 \mu V$ ). The mean MUAP amplitude increased 16 weeks after the virus injections due to an increased decomposition of larger amplitude units.

*Deviations which reached the alpha significance level (0.05) were marked in black while those that also passed the BH correction for multiple comparisons were marked in red. The decomposition of larger amplitude units did not prevent the simultaneous isolation of smaller amplitude units. (C) No significant changes were recorded in the CMAP amplitude compared to baseline, although a downward trend was observed 10 weeks after the virus injections. (D) The MUNE values calculated from the mean MUAP and CMAP amplitudes recorded across the grid electrode were highly variable, ranging from 237-426 in the baseline period. At week 10, the MUNE value sharply decreased to <200, and within five weeks had progressively decreased to below 20 where it remained for the duration of the study. The reduced MUNE values after week 10 all passed the BH correction. Error bars indicate SD, and dashed line represented the baseline mean and dotted lines represent 2 SDs of the baseline. Due to the accidental breakage of the chronic nerve cuff electrode wires, no stimulation data were recorded between Nov 2019 and Feb 2020 while the second surgery was planned, performed and subsequently recovered from. CMAP amplitude, and so also the MUNE derived from these values, were not recorded during this time (B-D). The animal was able to continue performing the trained behavioural task during this time, allowing for the decomposition of MUs.*

A mean of eleven ( $\pm 3$ ) MUs were decomposed from the R-BR of Monkey Ma during the isometric elbow flexion task during the baseline period (marked by the grey box, Figure 5.9A). This number was fairly stable each session, with the exception of a five week long reduction which occurred nine weeks after the virus injections. In this time the number of MUs decomposed decreased to as low as three ( $P < 0.05$ ). A further reduction occurred four months later, with the number of decomposed units dropping to four. Neither of these losses of decomposed MUs survived the BH correction for multiple comparisons. The amplitude of the decomposed average MUAP did not change significantly, however the size range of the decomposed MUAPs progressively declined until only those with a peak-peak amplitude of  $< 200 \mu\text{V}$  were identified (Figure 5.9B).

The average peak-peak CMAP amplitude across the grid showed a very different result to that recorded by the R-BR intramuscular electrodes (Figure 5.5E). No periods of reduction were recorded in the surface CMAP amplitude, which instead remained fairly stable for seven months of recordings with the exception of one session in which the average amplitude was larger than the baseline amplitude (6 weeks post injection,  $P < 0.05$ ) (Figure 5.9C). In the final weeks of the project, a downward trend in CMAP amplitude began to appear, and the inter-channel variability, expressed by the shaded error bars decreased indicating a loss of MUAP number or of the high threshold MUAPs, which contribute to the CMAP.

The MUNE values calculated for the R-BR of Monkey Ma were much lower than those calculated for the same muscle in Monkey Mi. The MUNE results calculated during the baseline period and during the tracking period were not significantly different, with all results fluctuating between 15.9 and 44.5 (Figure 5.9D).

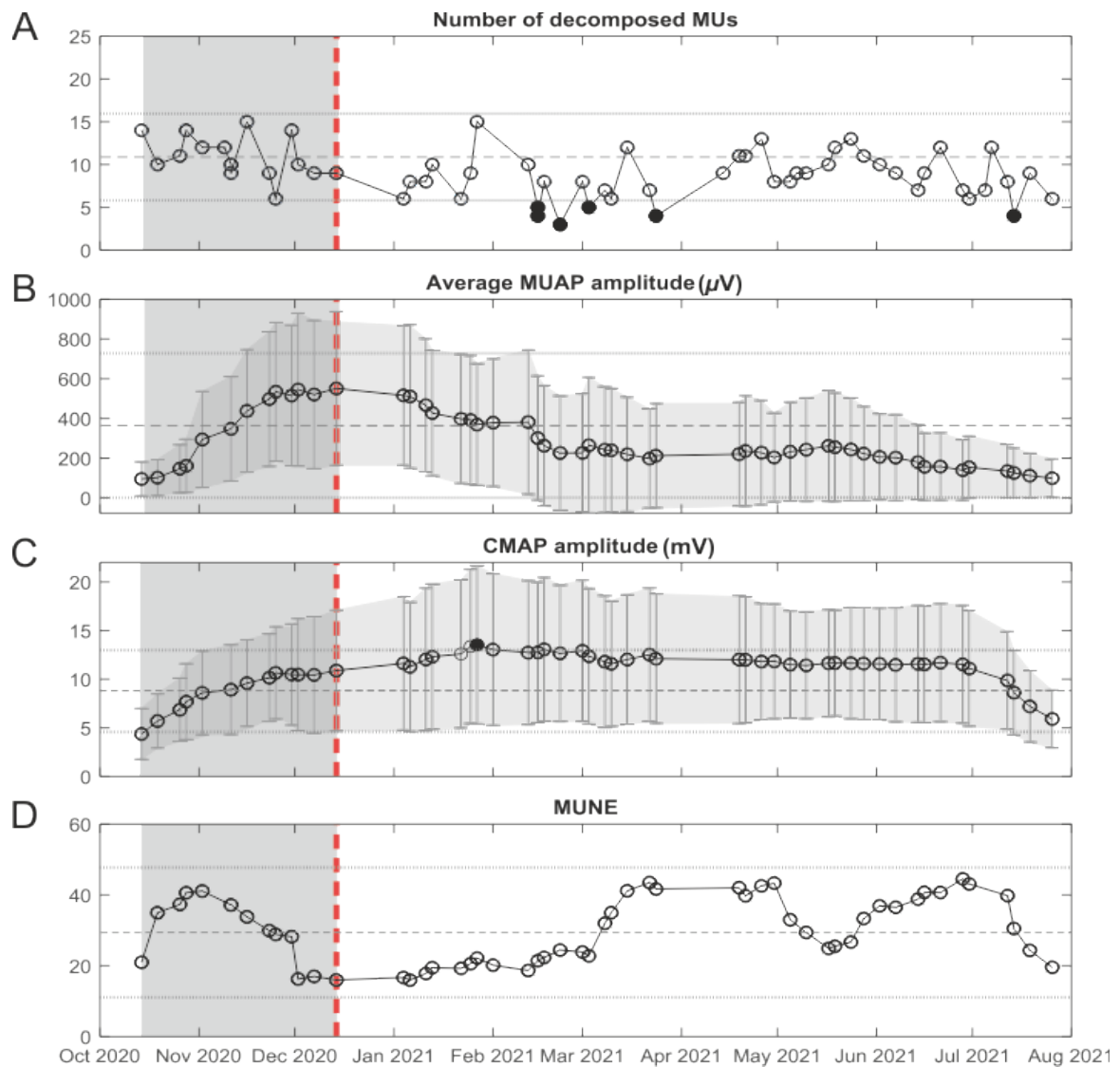


Figure 5.9. MUNE was calculated for the R-BR muscle of Monkey Ma from surface EMG signals recorded using a HD-sEMG grid. (A) A mean of  $11 (\pm 3)$  individual MUs were decomposed during the baseline period (grey shaded area) collected prior to the virus injections, indicated by the red dashed line. The number of decomposed units decreased 9 weeks after the virus injections for a duration of 5 weeks, at which time the number of units decreased to as low as 3 in one session ( $P < 0.05$ ). A further reduction occurred four months later, with the number of decomposed units dropping to four. Deviations from baseline which reached alpha significance but did not pass the BH correction for multiple comparisons were marked in black. (B) The amplitude of the decomposed MUAPs did not change significantly, however the size range of the MUAPs progressively declined until only those with a peak-peak amplitude of  $< 200 \mu\text{V}$  were identified. (C) The surface peak-peak CMAP amplitude did not decrease compared to baseline, as was recorded in the intramuscular CMAP. A slight arched trend was noted, with the amplitude in a session 6 weeks after injections six weeks after virus injection increasing beyond baseline ( $P < 0.05$ ) followed by a gradual decline in amplitude in the final month of recording following 6 months of stability. (D) The MUAP and CMAP amplitudes contributed to the MUNE

*calculation, which gave small values ranging between 16 and 45. No change from baseline MUNE was recorded in the R-BR of this animal. Error bars indicate SD, and dashed line represented the baseline mean and dotted lines represent 2 SDs of the baseline.*

As Monkey Ma also learnt to perform the isometric elbow flexion task with her left arm, we were able to implement the MUNE analysis on her L-BR. Similar to the R-BR, a mean of twelve ( $\pm 3$ ) MUs were decomposed during the baseline period, collected prior to the injection of the combination of viruses. The numbers of MUs decomposed by the algorithm did not change during the project (Figure 5.10A). Only small amplitude MUAPs ( $<200\mu\text{V}$ ) were recorded during the baseline sessions. After the time point at which the viruses were injected (marked by the red dashed line), an increased range of MUAPs were decomposed, with many larger MUAPs present (Figure 5.10B). The addition of larger MUAPs did not bias the algorithm against smaller amplitude units, as the error bars show a wide range ( $<100\mu\text{V}$ :  $>600\mu\text{V}$ ). The amplitude of the mean MUAP progressively declined six months after the viral administration until no large amplitude MUAPs were decomposed. The fourteen MUAPs decomposed during the final session were significantly smaller than those recorded during the baseline period ( $<100\mu\text{V}$ ). The changes in the amplitude of the MUAPs recorded in the L-BR of Monkey Ma all passed the BH multiple comparisons corrections (indicated by a red marker).

The CMAP amplitude recorded across the surface of the L-BR muscle exhibited a similar arch-like trend to that seen in the R-BR of this animal, with a smaller peak-peak amplitude recorded during the baseline sessions and the final month of recordings than the seven months following the viral vector injections (Figure 5.10C). The CMAP amplitude increased in the final week of January, the same time at which an increase was recorded in the R-BR surface CMAP amplitude (Figure 5.9C). The increase in the L-BR was maintained for seven weeks ( $P<0.05$ ), however the increase did not pass the BH multiple comparisons test.

There was greater variation in the MUNE values calculated from the left arm than the right; and the values themselves were higher (Figure 5.10D). The MUNE values collected from the baseline period ranged from 47.55 to 123.20. Following the virus injections targeting the contralateral BR muscle, the MUNE values remained largely between 40 and 100, with the exception of a five week period where the MUNE decreased below 30 ( $P<0.05$ ).

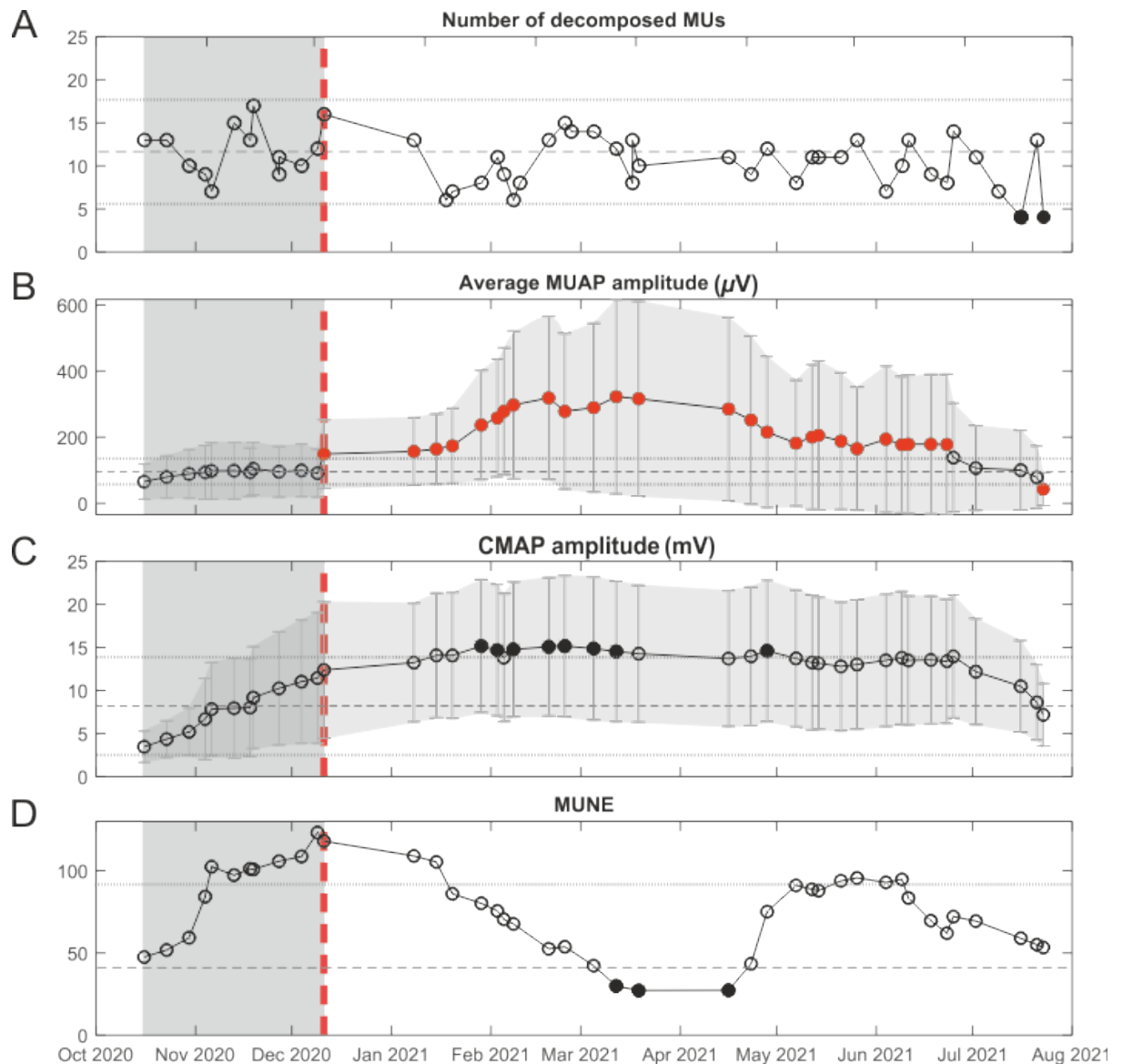


Figure 5.10. MUNE was calculated for the L-BR muscle of Monkey Ma from surface EMG signals recorded using a HD-sEMG grid. (A) A mean of 12 ( $\pm 3$ ) MUs were decomposed from the baseline period (grey shaded area), collected prior to the injection of the combination of viruses (indicated by the red dashed line). (B) The decomposition algorithm detected a wider range of MUs after the virus injection, which lead to an increase in the mean MUAP amplitude. 6 months after the virus injections, this increase in the mean amplitude decreased and ultimately became lower than the baseline mean MUAP amplitude. All of the changes in MUAP amplitude passed the BH correction, thus they are marked in red. (C) The CMAP amplitude in the L-BR followed a similar trend to that seen in the R-BR of Monkey Ma (Figure 5.8D), with an increase in the amplitude recorded 6 weeks after the virus injections which was maintained for 7 weeks ( $P < 0.05$ ). These increases in CMAP amplitude from baseline did not survive the BH test and so are marked in black. A downward trend in the CMAP amplitude was noted in the same session as the decrease in the MUAP amplitude. (D) The MUNE values calculated from the L-BR were higher than the R-BR MUNE values. The MUNE ranged largely between 40 and 100

*following the virus injections, with an exception of a 5 week period where the MUNE decreased to <30 ( $P < 0.05$ ). Error bars indicate SD, and dashed line represented the baseline mean and dotted lines represent 2 SDs of the baseline.*

## **Discussion**

In this study we applied techniques used clinically, such as MUNE and the more straightforward tracking of CMAP amplitude for between seven and eight months in two macaques overexpressing the protein TDP-43, implicated in the propagation of MND, in the spinal MNs supplying their right BR muscle. We were able to track the CMAP amplitude in five forearm muscles bilaterally using chronically implanted intramuscular EMG electrodes and chronic stimulating cuffs surgically placed around the radial and median nerves. Using decomposition techniques recently validated in Monkey, we were able to isolate surface MUAPs from the left and right BR muscles with the use of a HD-sEMG electrode grid (Del Vecchio et al., 2022). This same grid was used to collect the surface CMAP across the muscle. These readings allowed us to perform MUNE analysis on the BR muscles, an analysis technique which is being incorporated into the clinical assessment of MND patients more and more frequently.

There are various methods of performing MUNE, with most differing in regards to their MUAP identification techniques. In order to validate MUNE for its potential use as a clinical biomarker, more work must be performed to make sense of the individual differences in the values given by the varying techniques. Efficient animal models are crucial to the improvement of our understanding, where factors such as posture, electrode position and regularity of sampling, all of which have shown to impact MUNE and CMAP amplitude values, can be better controlled for than is possible clinically (Boekestein et al., 2012, Maathuis et al., 2008). We were able to control for these factors by using chronically implanted stimulating cuff electrodes placed around the radial and median nerves; chronically implanted intramuscular EMG electrodes; a semi-permanent marking of grid position that was re-applied daily and an arm cast to position the limb in an identical posture each session.

Similar studies have been performed in rodent models of MND, using the time intensive MPS stimulation method while the animals were anaesthetised (Shefner et al., 2006). There is much debate as to the relevancy of rodent models for such a complex human motor disorder, thought to involve the direct corticomotoneuronal pathway that rodents lack. In order to recapitulate the disease so as to develop and validate clinical assessments, an animal such a non-human primate (NHP) is required. We employed MUNE in our range of electrophysiological techniques in the hopes of validating the technique for the assessment of a MND-like denervation event and validating our model alike. Due to the nature of primate research, adaptations were made to the MUNE protocol. Rather than sampling MUAPs using ICT or MPS methods, which may be uncomfortable and would be extremely time intensive if the animal were to produce any voluntary activity during the sampling, MUAPs were decomposed from voluntary activity collected while the animals performed an isometric elbow flexion task within a set force range.

MUNE produced highly variable results in this longitudinal study in a NHP model of MND. Relatively small fluctuations in CMAP or mean MUAP amplitude led to exaggerated changes in the estimated MU number (Figure 5.8). Furthermore, the weighting function proposed by van Dijk et al. (2008) for multi-electrode MUNE analysis contributed to the irregularities. Alterations in the proportion and range of high and low amplitude MUAPs collected in each session may bias the weighting factor, leading to the high variability in MUNE. This weighting factor was developed to account for noise in MUAPs collected by incremental stimulation. It is possible that this technique is not directly transferrable to our method, in which MUAP amplitudes, collected from the voluntary activity produced during high force movements, often varied between sessions of the same animal.

The fairly low number of MUs estimated to be present in the left and right BR of Monkey Ma, and in the R-BR of Monkey Mi during the latter half of the project were somewhat in line with previous research regarding the functionality of MUNE in regards to force levels (Boe et al., 2005, Boe et al., 2006, Peng et al., 2016). When MUNE has been tested with MUAPs decomposed from voluntary activity at various contraction intensities, as the force increases so too does the bias of the decomposition algorithm to higher amplitude units, leading to an underestimation of the MUNE. The sampling of units by incremental stimulation tends to favour smaller amplitude units, a bias which accounts for overestimation of the MUNE (Gooch et al., 2014). The predisposition of the algorithm towards the detection of small amplitude units in the first four months of Monkey Mi's

recordings may have contributed to an overestimation of MUNE values in this muscle. The values and even the large variation were still in keeping with the literature (Peng et al., 2016). Without a 'gold standard' approach for motor unit estimation with which to compare against, it is difficult to say whether the variation seen in this study is truly representative of ongoing changes or a limitation of the technique.

It is likely that the MUNE results were so variable due to the method of MUAP extraction used in this study, in which the 6kg animals exerted an equivalent of 2-4kgF during their task. A clear drawback of an animal model in this case is the feasibility of defining multiple force targets for the animal as a percentage of their maximum voluntary contraction (MVC). It is likely that the decomposed MUAPs were not representative of the true average MUAP in the muscle. However, the decomposition algorithm employed in this study did not display this pre-documented bias towards the higher amplitude units, and was clearly able to decompose even the smaller amplitude ( $<100\mu\text{V}$ ) units alongside larger ( $>600\mu\text{V}$ ) units. The only exception to this was seen during the baseline period of the R-BR from Monkey Ma. In this case, when units with an amplitude of  $>800\mu\text{V}$  were decomposed, there was a dropout of the  $<100\mu\text{V}$  units. Therefore it is possible that there is a size threshold at which point the decomposition algorithm is unable to isolate temporally superimposed MUAPs.

An obvious alternative to our current method for MUAP sampling would be to perform the ICT method developed by McComas et al. (1971) or the more updated MPS method. Rather than decomposing voluntary activity into single motor unit activity, these methods use graded stimulation to identify the progressive recruitment of single units. There are many technical limitations associated with these techniques, especially in their application in NHP research. Any voluntary activity elicited during the sampling prevents the identification of units. In fact, human participants and patients are typically provided with visual EMG feedback to aid their suppression of voluntary activity. This is more of a challenge in NHP work, particularly during time intensive MPS sessions. This technique has been successfully applied on anaesthetised rodents, however the necessity for anaesthesia may limit the frequency of sampling and any improvements to the technique in such a circumstance could not be clearly transferred to a clinical setting. Furthermore, the very nature of these MUAP sampling techniques limits the discovery to low threshold MUAPs, as high threshold MUAPs are seldom active in isolation and rather form complex signal patterns in combinations with many other simultaneously firing MUs. The MUNE

values derived from the R-BR of Monkey Mi exemplify the overestimation produced by a sample of low amplitude MUAPs.

The intramuscular CMAP amplitude, with testing at regular intervals, detected a reduction in the R-BR of both animals, as well as other changes in primarily the other extensor muscles. This reduction was followed by a recovery, most likely due to compensatory reinnervation. It is therefore essential to perform regular sampling in order to appreciate the ongoing pattern of denervation and reinnervation. The phasic reduction in the CMAP amplitude of R-BR muscle of Monkey Ma may be indicative of a primary, isolated denervation event caused by the loss of the originally transfected spinal MNs, followed by a secondary spread of pathology and so further reductions. The CMAP amplitude of the neighbouring extensor muscles, as well as the contralateral extensors, were also altered during this time. Phasic changes in the CMAP amplitude of these muscles, though not always in the same direction, may be indicative of spreading pathology throughout the motoneurons supplying both limbs. Alternatively, increases seen in the EDC and ECR muscles may represent compensatory action.

Interestingly, the CMAP amplitude recorded across the grid did not show the same fluctuations as was recorded on the intramuscular electrodes. The results from the R-BR of Monkey Mi may be an exception to this, as a similar downward trend in the CMAP amplitude was detected in the grid, which occurred at the same time point as was detected by the implanted electrodes. As the intramuscular and surface electrodes sample different populations of MUs, it is possible that the deep MUs were more efficiently targeted by the viral vector, which was injected near the endplate regions deep within the BR muscle.

The hyperintense signal detected in MRI scans of the R-BR (see Chapter III), together with the phasic limb-wide changes in voluntary activity during an isometric hold task (see Chapter IV) indicated the occurrence of an initial disturbance in the transfected muscle, followed by on-going denervation and reinnervation in additional muscles. MUNE and CMAP analysis, however, were not efficient in detecting an MND-like denervation event in a NHP model of MND. The MUNE values were highly variable between animals and between muscles of the same animal, and clear over or underestimations were produced with minor changes in MUAP or CMAP amplitude. MUNE analysis is not currently relied on clinically due to high variability between healthy participants and longitudinally, therefore the variation in MUNE values between the animals and limbs of the same animal

was not unexpected. The size of MUAPs is known to increase during the course of MND, which in theory could cause an overestimation of the amount of neurodegeneration occurring. More research must be performed to understand the subtleties of this analysis before it can progress as a clinical biomarker. Technical factors of the MUNE protocol are inherently limited in primates, which may contribute to the high variability noted in these results. The intramuscular CMAP amplitude proved the most interesting and valuable technique for monitoring changes in the muscle health, however regular sampling is required in order to identify these changes prior to compensatory reinnervation.

# CHAPTER VI. Histopathological Changes in the Spinal Cord of a NHP Model of MND

## Introduction

Alpha-motoneurons ( $\alpha$ -MNs), Sherrington's 'final common path', located in lamina IX of the spinal cord ventral horn, receive direct signals from cortical and subcortical structures via pathways such as the corticospinal tract (CST). This pathway provides a monosynaptic connection between the  $\alpha$ -MNs and corticomotoneuronal (CM) cells of the primary motor cortex (M1). An evolutionarily older branch of the CST delivers cortical inputs to segmental and propriospinal interneurons, some of which connect to the MNs, providing them with indirect cortical signals and modulating their activity. The spinal MNs integrate these descending inputs and in turn project to the skeletal muscles of the periphery, thus regulating voluntary movement.

Subsets of  $\alpha$ -MNs connect to and supply individual muscles, making up the 'motor pool' of that muscle. These motor pools are arranged in rostrocaudal columns spanning several spinal segments. The motor pools are not anatomically discrete groups, but rather overlap with other  $\alpha$ -MN pools that innervate functionally similar muscles (Jenny and Inukai, 1983). The long axons of the neurons within each motor pool travel in bundles, making up the peripheral nerves, to terminate within their target muscle. Each motoneuron innervates multiple extrafusal muscle fibres within the muscle, making up the motor unit. This connectivity allows for the generation of coordinated motor activity within the muscle.

Other MN subtypes, such as beta- ( $\beta$ -MNs) and gamma-MNs ( $\gamma$ -MNs) are also present in the spinal cord.  $\gamma$ -MNs innervate intrafusal muscle fibres located within the muscle spindle, providing proprioceptive feedback to the spinal cord regarding the velocity and extent of muscle stretch (Hunt and Kuffler, 1951, Kuffler et al., 1951, Matthews, 1981).  $\beta$ -MNs are not as well described as the other MN subtypes, however they have been shown to innervate both intra- and extrafusal fibres (Barker et al., 1977, Bessou et al., 1965). These subtypes are difficult to differentiate histologically. All MNs express choline acetyl transferase (ChAT), the enzyme responsible for the synthesis of the neurotransmitter acetylcholine (ACh) (Barber et al., 1984).  $\alpha$ -MNs are large, multipolar cells found in the well-defined Rexed laminae IX. The morphological features of this cell type facilitate their identification, and there is also evidence that these cells can be identified by their expression of the neuronal marker NeuN together with ChAT.  $\beta$ - and  $\gamma$ -MNs, both much smaller than  $\alpha$ -MNs,

are more difficult to distinguish from each other. NeuN expression can be used to differentiate between  $\alpha$ - and  $\gamma$ -MNs, as the latter population downregulate this protein (Shneider et al., 2009). The receptor protein, Err3, has been used as a selective marker for  $\gamma$ -MNs in rodents, and while it has been documented with some success in cultured human  $\gamma$ -MNs its broader application in human tissue is unconfirmed (Lalancette-Hebert et al., 2016, Colon et al., 2017).

Contradicting their classical definition as large cells,  $\alpha$ -MNs are not uniform in size. It has been established for some time that variations in MN size are inversely related to their electrical activity and recruitment order (Henneman, 1957, Le Masson et al., 2014). Differences in size also contribute to varying vulnerability to degeneration in MND. Larger MNs, generally in control of larger motor units are thought to degenerate before their smaller counterparts (Le Masson et al., 2014, Nijssen et al., 2017).

### **a-MN pathology in MND**

Motor neurone disease (MND) is characterised by the rapidly progressing degeneration of specific subsets of neurons involved in motor processing and movement. During the progression of this disease, the nuclear protein TDP-43 undergoes cytoplasmic mislocalisation and becomes phosphorylated, at which point pTDP-43 inclusions form (Neumann et al., 2006, Arai et al., 2006). This process culminates in the death of the cell.  $\alpha$ -MNs, often referred to clinically as lower motor neurons (LMNs), are selectively vulnerable in (MND), with pTDP-43 pathology developing in the earliest stage of the disease (Brettschneider et al., 2013). CM cells (UMNs), despite their differences in location, morphology and neurotransmitter profile from the spinal MNs, are also targeted during this initial stage. It has been proposed that TDP-43 neuropathology spreads in a characteristic pattern throughout the central nervous system (CNS) (Brettschneider et al., 2013). This spread has been proposed to propagate using a 'prion-like' mechanism of self-perpetuation due to the nature of the TDP-43 aggregates themselves (Nonaka et al., 2013).

This pattern of spread appears to avoid particular neuronal subsets. MNs themselves are not affected equally, with certain subpopulations displaying increased susceptibility compared to others (Nijssen et al., 2017). The aforementioned contribution of soma size variability is not limited to  $\alpha$ -MNs. The small  $\gamma$ -MNs, for example, are thought to remain unaffected during the course of the disease, however this finding is yet to be confirmed in patient tissue. Within the spinal cord, MND neuropathologies are primarily found in  $\alpha$ -

MNs, which synapse directly with CM cells, or the upper motor neurons, of the primary motor cortex (M1) and the extrafusal muscle fibres. Impairments at any link in the chain between the cortex and musculature reflect the clinical manifestations of weakness, atrophy and loss of dexterity characteristic of MND. Differences in degenerative susceptibility within the population of  $\alpha$ -MNs is also affected by the contractile speed of their innervation targets. Various rodent models of MND have shown a gradient of degeneration, with MNs making up the fast fatigable motor units dying off first and those which supply the slower motor units often surviving until late in the disease course (Frey et al., 2000, Hegedus et al., 2007, Spiller et al., 2016). This pattern of preferential cell involvement and deterioration reflects the clinical phenotype observed in each patient throughout the disease course.

The aim of this study was to determine whether a viral vector mediated TDP-43 overexpression event within a focal spinal motor pool, would be sufficient to induce MND-like pathology. Of particular interest in this study, was whether any proteinopathies identified would be limited to only the transfected MNs, or whether this pathology was capable of spreading to contiguous cells. We have developed a novel dual virus approach which has enabled us to induce the overexpression of the healthy, human TDP-43 protein in only the spinal MNs which innervate the right brachioradialis (BR) muscle. Evidence of TDP-43 pathology in cells other than those transfected may support the argument for this protein acting in a 'prion-like' fashion.

## **Methods**

### ***Animals***

Tissue was collected from two chronically implanted adult female awake behaving Monkeys (*M. mulatta*; Monkeys Mi and Ma, age 6 years, weight 6.1 and 6.9kg at outset) and one female control animal (age 3 years). All animal procedures were performed under appropriate licences issued by the UK Home Office in accordance with the Animals (Scientific Procedures) Act (1986) and were approved by the Animal Welfare and Ethical Review Board of Newcastle University.

### ***Immunohistochemistry***

Following the completion of the study, the animals were anaesthetised to a lethal level by administering intravenous propofol. The animals were perfused through the heart with phosphate buffered saline (PBS) followed by 10% neutral buffered formalin (NBF). The cortex, cerebellum, brainstem and spinal cord were removed and immersed in 10% NBF for 16 hours at 4°C before progressing through ascending concentrations of PBS sucrose (10%, 20%, 30%) for cryoprotection. A freezing sledge microtome (8000-01, Bright Instruments Co. Ltd, United Kingdom) connected to a solid state freezer (53024-01, Bright Instruments Co. Ltd, United Kingdom) was used to cut the spinal cord into 40µm coronal sections. All sections were stored free floating in PBS at 4°C until further processing.

### ***Fluorescent viral tag***

Sections from cervical segments spanning and surpassing those known to supply the BR muscle (C4-C8) were labelled with an antibody against red fluorescent protein (RFP) and its variants in order to detect tdTomato positive cells. Sections were collected at 960µm intervals for anti-RFP immunostaining to detect the tdTomato viral tag (600-401-379, RFP Pre-adsorbed Polyclonal Antibody, Rockland; 1:1000). Primary antibody dilutions were performed using a PBS solution containing 0.3% Tween-20 (Sigma-Aldrich) and 5% donkey serum (Bio-Rad Laboratories). A goat anti-ChAT polyclonal antibody (Sigma-Aldrich; 1:500) was applied to the sections overnight at 4°C. The sections were washed in PBS 3 times before a donkey anti-goat Alexa Fluor 488 (ab150129, abcam; 1:1000) was applied as a secondary antibody for 2 hours at room temperature. The sections were shielded from light during the secondary incubation and for all subsequent steps to prevent bleaching of the signal. The sections were again washed 3 times in PBS before being

mounted onto Superfrost Plus slides (Thermo Scientific). Once the sections had dried and adhered onto the slides, they underwent the Sudan Black B staining protocol in which they were dehydrated in 70% ethanol for 5 minutes before being immersed in Sudan Black B (199664, Sigma-Aldrich) dissolved in a 70% ethanol solution for 10 minutes. Following this the slides are washed twice in PBS to remove any residual Sudan Black deposits. The Sudan Black binds to and quenches the autofluorescent protein, lipofuscin, which builds up in the cytoplasm of cells of the CNS with age (Schnell et al., 1999). Fluoroshield mounting medium with DAPI (ab104139, abcam) was used to counterstain cell nuclei and coverslips were placed.

### ***Functional TDP-43***

Sections were collected at 960 $\mu$ m intervals for TDP-43 immunostaining (10782-2-AP, TDP-43 Polyclonal antibody, ProteinTech; 1:2000). Sections were washed with 0.1M PBS before incubated with 3% H<sub>2</sub>O<sub>2</sub> for 5 minutes to quench any endogenous peroxidase activity. Following this, the sections were washed with PBS a further 3 times. Primary antibody dilutions were performed using a PBS solution containing 0.3% Tween-20 (Sigma-Aldrich) and 5% goat serum (Vector Laboratories). A rabbit anti-TDP-43 polyclonal antibody (ProteinTech; 1:2000) was applied to the sections overnight at 4°C. The following day the sections were washed three times with PBS prior to a 30 minute incubation with an ImmPRESS HRP goat anti-rabbit IgG polymer reagent (MP-7451, Vector Laboratories) at room temperature. The sections were again washed with PBS 3 times to remove any residual secondary antibody. A DAB substrate (3,3'-diaminobenzidine) (SK-4100, Vector Laboratories) was applied to the sections until a desired stain intensity developed (2 minutes). The DAB substrate produces a brown precipitate in the presence of the peroxidase (HRP) enzyme. Tap water was applied to the sections for 5 minutes to quench the reaction. At this point sections were mounted onto Superfrost Plus slides (Thermo Scientific) and allowed to air dry. Sections were dehydrated in ascending ethanol solutions (70%, 90%, 100%) and cleared in histoclear for 10 minutes. Sections were coverslipped with VectaMount (Vector Laboratories).

### ***Phosphorylated TDP-43***

Sections were collected at 320-480 $\mu$ m (Mi = 1/12, Ma = 1/8) intervals for phosphorylated TDP-43 (pTDP-43) immunostaining (CAC-TIP-PTD-M01, Anti TAR DNA-Binding Protein 43 (TDP-43), phospho-Ser409/410 mAb (Clone 11-9), CosmoBio Ltd; 1:500)

(Inukai et al., 2008). Sections were washed with 0.1M PBS before a 3% H<sub>2</sub>O<sub>2</sub> incubation for 5 minutes to quench any endogenous peroxidase activity. Following this, the sections were washed with PBS a further 3 times. Primary antibody dilutions were performed using a PBS solution containing 0.3% Tween-20 (Sigma-Aldrich) and 5% goat serum (Vector Laboratories). A mouse anti-TDP-43 phospho-Ser409/410 polyclonal antibody (CosmoBio Ltd; 1:500) was applied to the sections overnight at 4°C. The following day the sections were washed three times with PBS prior to a 30 minute incubation with an ImmPRESS HRP goat anti-mouse IgG polymer reagent (MP-7452, Vector Laboratories) at room temperature. The sections were again washed with PBS 3 times to remove any residual secondary antibody. A DAB substrate (3,3'-diaminobenzidine) (SK-4100, Vector Laboratories) was applied to the sections until a desired stain intensity developed (2 minutes). Tap water was applied to the sections for 5 minutes to quench the reaction. At this point sections were mounted onto Superfrost Plus slides (Thermo Scientific) and allowed to air dry. Sections were dehydrated in ascending EtOH solutions (70%, 90%, 100%) and cleared in HistoClear for 10 minutes. Sections were coverslipped with VectaMount (Vector Laboratories).

### ***Motoneuron labelling***

Spinal cord motoneurons were labelled and identified with a primary antibody for choline acetyl transferase (ChAT) (ab144P, Anti-Choline Acetyltransferase Antibody, Sigma-Aldrich; 1:500). Sections were collected at 360-480µm (Mi = 1/12, Ma = 1/9) intervals for ChAT immunoanalysis. Primary antibody dilutions were performed using a PBS solution containing 0.3% Tween-20 (Sigma-Aldrich) and 5% donkey serum (Bio-Rad Laboratories). A goat anti-ChAT polyclonal antibody (Sigma-Aldrich; 1:500) was applied to the sections overnight at 4°C. The sections were washed in PBS 3 times before a donkey anti-goat Alexa Fluor 488 (ab150129, abcam; 1:1000) was applied as a secondary antibody for 2 hours at room temperature. The sections were shielded from light during the secondary incubation and for all subsequent steps to prevent bleaching of the signal. The sections were again washed 3 times in PBS before being mounted onto Superfrost Plus slides (Thermo Scientific). Once the sections had dried and adhered onto the slides, they underwent the Sudan Black B staining protocol in which they were dehydrated in 70% EtOH for 5 minutes before being immersed in Sudan Black B (199664, Sigma-Aldrich) solution for 10 minutes on a shaker plate. Following this the slides are washed twice in PBS to remove any residual

Sudan Black deposits. Fluoroshield mounting medium with DAPI (ab104139, abcam) was used to counterstain cell nuclei and coverslips were placed.

### ***Microscopy and Quantification***

All spinal cord motoneurons were identified by their morphology, as large multipolar neurons, and by their location within lamina IX of the ventral horn grey matter. Non-motoneuronal cell types were excluded from counts based on this criteria. Brightfield images of TDP-43 and pTDP-43 labelled sections were acquired using a Zeiss AxioImager (Carl Zeiss AG, Oberkochen, Germany) which allowed for tiling using a 10x objective. Fluorescently labelled sections were imaged using a Zeiss CellDiscoverer 7 (Carl Zeiss AG, Oberkochen, Germany) connected to a highly sensitive Hamamatsu Fusion sCMOS camera which allowed for multi slide imaging. Motoneurons labelled for pTDP-43 or ChAT were counted using the ImageJ Cell Counter tool (O'Brien et al., 2016) in the left and right ventral horn of all cervical segments for both Monkeys. pTDP-43 positive motoneurons were considered as cells displaying MND-like pathology.

### ***Statistical analysis***

Data were analyzed using custom scripts written in the MATLAB environment (R2020a, MathWorks). Statistical tests were performed using MATLAB. Paired t-tests were used to compare pTDP-43 and ChAT positive cell counts from contralateral sides of each spinal segment. The significance level was set at  $p < 0.05$ . A two-way ANOVA was used to compare both the effects of side (ipsilateral-contralateral) and the effect of segment on pTDP-43 counts. To examine the intersegmental effects, pairwise t-tests were performed to compare each segment against the group of segments in which reductions in ChAT+ motoneurons were counted. Benjamini Hochberg (BH) correction was applied to these results to account for multiple comparisons (Benjamini and Hochberg, 1995).

## **Results**

### ***Viral Tag***

The cervical spinal cord of both animals injected with a combination of adeno-associated viruses designed to induce overexpression of the protein, TDP-43, in the motor pool of the right brachioradialis (BR) muscle was assessed histologically for the expression of various proteins once the animals had been terminated, thirty-two weeks following the injection of the two viruses. The rAAV2 viral vector with a genetic payload including cre recombinase and a fluorescent tag, tdTomato, was injected intramuscularly to retrogradely transfect the spinal motoneurons (MNs) that project to the muscle. The AAV9, with a genetic payload containing the floxed, inactive TDP-43, was administered via a lumbar puncture to transfect all cells within the spinal cord. The TDP-43 is only excised and activated in the cells transfected with both viruses as the Cre recombinase is essential for this process. The fluorophore, tdTomato, if highly expressed, fluoresces intrinsically without the need for histological enhancement. Antibodies have also been developed against this fluorophore in order to improve its detection. To ascertain the location of virus expression within the spinal cord, we used an antibody against the fluorophore tdTomato, anti-RFP, to infer which cells had been transfected with the retrograde virus and were expressing its viral load. We have had previous success in our lab with retrograde transfection of spinal motoneurons causing the expression of the aforementioned fluorophore following intramuscular administration of rAAV2 (Figure 6.1A). No motoneurons were found to express the fluorophore in the C4-C8 segments of either animal in this study (Figure 6.1B).

### ***Evidence of Motoneuron Loss***

Following the absence of viral tag in the spinal cord, the tissue from the transfected animals, as well as a healthy control macaque, was stained for choline acetyl transferase (ChAT), an enzyme crucial for the synthesis of the neurotransmitter acetylcholine, used by spinal MNs. This enzyme has been used as a classical marker for spinal cord MNs, an example of this staining in the spinal cord grey matter of Monkey Mi can be seen in Figure 6.1C. ChAT positive cells within lamina IX of the left and right ventral horns were counted manually in 12-18 sections per spinal segment, at intervals of 360-480 $\mu$ m, to provide a measure of motoneuron number per side. Left and right counts from each section per segment were individually averaged to provide an average left and right motoneuron number for each spinal segment (Figure 6.1). MN counts in a healthy control macaque demonstrated a clear bell-shaped distribution throughout the cervical spinal cord, with less MNs recorded in C1

and T1 segments compared to C4-C8 segments. This increased number of MNs in the central cervical segments, with the exception of T1, was in keeping with the location of the cervical enlargement (Kuypers, 1981, Dum and Strick, 1996). There were significantly fewer MNs on the right side of the cord in spinal segments likely to innervate the BR muscle (Jenny and Inukai, 1983); C6 and C7 of Monkey Mi and segments C7 and C8 of Monkey Ma (Monkey Mi C6,  $P=0.000078$ ; Monkey Mi C7,  $P=0.0062$ ; Monkey Ma C7,  $P=0.0108$ ; Monkey Ma C8,  $P=0.00074$ ). No significant differences were recorded between the left and right counts in the healthy control, while both experimental animals showed significant losses on the right side of the spinal cord. The loss of MNs in the segments that supply the right BR, together with the lack of any cells expressing tdTomato, was consistent with the complete loss of transfected MNs. Furthermore, the control counts indicated a further possible loss of MNs in both the right and left side of the cord in the C4-C8 segments of Monkey Mi, whose counts were markedly lower than the control. The counts from Monkey Ma were more similar to those from the control animal, but did not replicate the same smooth distribution, and may also indicate a less advanced degree of MN loss in C6-C8. The impact of inter-animal variability may have also played a role in the differences in MN counts recorded between the animals.

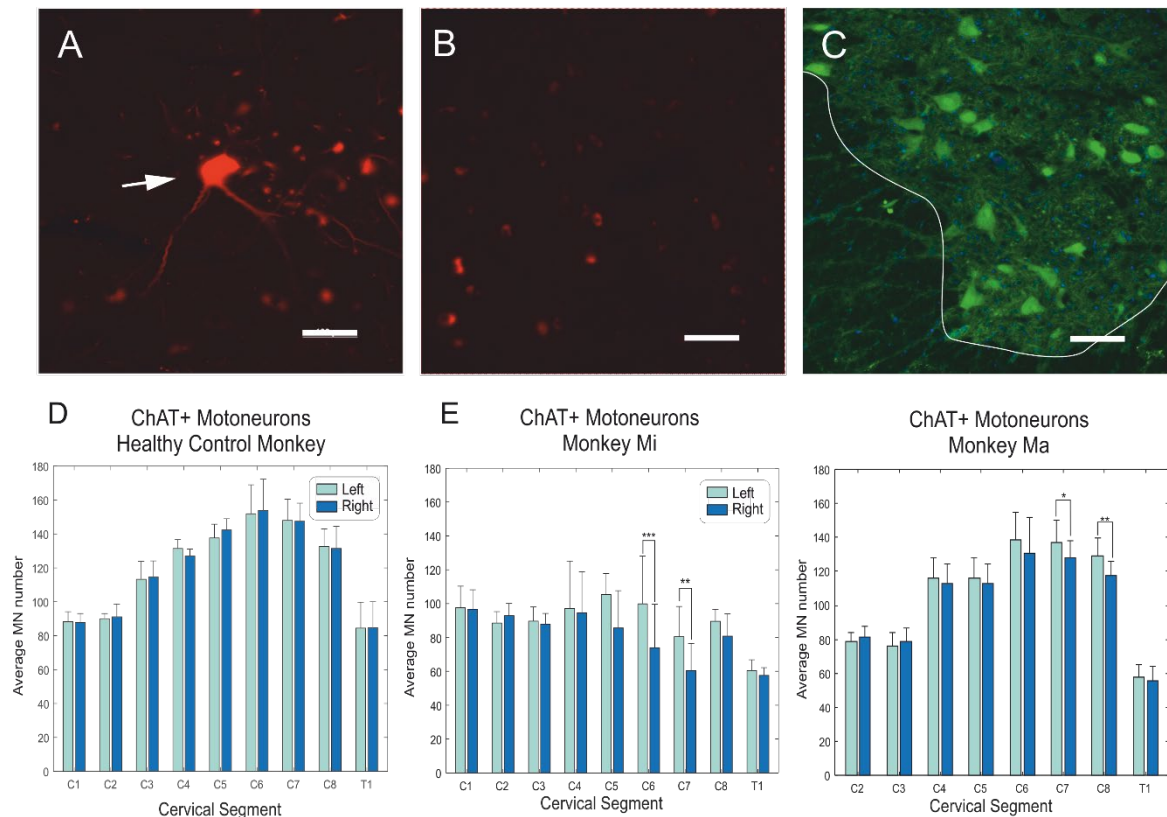


*Figure 6.1. Evidence for motoneuron degeneration in spinal segments innervating the brachioradialis (BR) muscle. The viral constructs (Fig. 2.1B) included a tdTomato fluorescent protein, which should be expressed in motoneurons infected by the rAAV2. A, previous studies in our group showed that retrograde viral transfection is effective, and that motoneurons express tdTomato when the genetic payload does not include TDP-43, as seen in this example image. Arrow indicates MN expressing tdTomato fluorophore. B, in the animals used for the macaque motoneuron disease model, no motoneurons with tdTomato were visualised. (A, B) Scale bar = 100 $\mu$ m. C, sections were stained for choline acetyl transferase (ChAT). ChAT positive cells within lamina IX of the spinal cord were counted in 12-18 sections (thickness 40 $\mu$ m) per spinal segment, collected at 320-480 $\mu$ m intervals, to provide an estimate of motoneuron number. Scale bar = 200 $\mu$ m. D, motoneuron counts for the healthy control macaque. There were no differences in ChAT<sup>+</sup> cell numbers between the left and right ventral horns at any segment between C1 and T1 in the healthy control animal. A clear gradual increase in MN number was seen in this animal, with C1 and T1 containing the fewest number of ChAT<sup>+</sup> cells, with this number increasing in segments which fall within the cervical enlargement (C5-C8). E, motoneuron counts for the two Monkeys infected with TDP-43 constructs, as in Figure 2.1. There were significantly fewer motoneurons on the right side of the cord for the C6/C7 segments of Monkey Mi and the C7/C8 segments of Monkey Ma; these are segments which innervate the BR muscle (\*,  $P < 0.05$ ; \*\*,  $P < 0.01$ ; \*\*\*,  $P < 0.0001$ ). The results are consistent with a complete loss of the doubly transfected motoneurons projecting to the BR muscle at the 32<sup>nd</sup> week when animals were killed to examine histology.*

### ***TDP-43***

In order to determine the cause of this spinal MN loss and to see if any obvious TDP-43 overexpression had been induced by the viral transfection, we stained the cervical tissue of these two animals for the protein TDP-43, using an antibody against the full length ‘functional’ protein. We saw very high expression of this protein in lamina IX MNs on both sides of the spinal cord and throughout all segments analysed. Closer inspection of the tissue revealed that this staining was not limited to the MNs but was also present in smaller cells, assumed to be interneurons, throughout the grey matter. The protein expression in the MNs was not limited to the nucleus, as it is in healthy control macaque spinal cord (Figure 6.2A and B). A high level of TDP-43 expression was detected throughout the cervical spine and first thoracic segment in both animals (Figure 6.2C-H).

It was noticeable that in C7 and C8, segments which innervate the BR muscle and where significant reductions in ChAT expressing MNs had been previously recorded, TDP-43 proteinopathies were especially prevalent. Enlarged images in Figure 6.2D and H show cells with a loss of clear nuclear protein expression and substantial clusters and clumps of dense expression throughout the cytoplasm. In segments that do not innervate the BR muscle, high expression was detected in both the nucleus and the cytoplasm, where the protein was expressed uniformly throughout the cell body and dendrites (Figure 6.2E, F). While the morphology of the cells detected in C1-C5 and T1 segments appeared healthy and no aggregates were detected, there was a clear difference from the strictly nuclear expression detected in the healthy age-matched control animal.

Following on from this, we stained the tissue for an antibody against the pathological phosphorylated TDP-43 serine groups 409/410 to assess whether the high expression levels of the functional TDP-43 could be proteinopathic. No phosphorylated TDP-43 (pTDP-43) was detected in the healthy control macaque spinal cord, consistent with the findings that phosphorylation at these sites on the protein occurs only in pathological conditions (Figure 6.3A and B) (Inukai et al., 2008). The very light staining detected in the control macaque spinal cord was most likely lipofuscin, a lipid protein which accumulates in neurons in normal ageing (Schnell et al., 1999, Moreno-Garcia et al., 2018). In animals where TDP-43 had been overexpressed, pTDP-43 was distributed throughout the spinal cord grey matter of all cervical segments, not just the segments known to innervate the BR. This expression was also not solely limited to MNs of lamina IX but also in cells of dorsal horn and intermediate zone. This protein was highly expressed in the cytoplasm of the MNs,

consistent with the characteristic cytoplasmic mislocalisation recorded in the spinal MNs of motor neurone disease (MND) patients (Figure 6.3C-H). Some nuclear expression of pTDP-43 was also identified, however this was less pronounced in segments which supply the BR muscle (Figure 6.3H). The complete absence of pTDP-43 expression in the healthy control animal, reaffirmed the causal link between the virus mediated TDP-43 overexpression in the R-BR motor pool and the ultimately widespread pathological pTDP-43 expression.

The pTDP-43 expression on both sides of the spinal cord and throughout the cervical and first thoracic segment indicated widespread pathology in the transfected animals. pTDP-43 positive cells in lamina IX with motoneuron-like morphology were counted manually in 12-18 sections per spinal segment, at intervals of 360-480 $\mu$ m, to provide an estimate of motoneurons expressing pathological changes. The counts per section were averaged to provide a mean number of pTDP-43 positive MNs per spinal segment. pTDP-43 expression in MNs was detected in all segments of the cervical spine and also in the first thoracic segment (Figure 6.4). No significant differences were recorded between the left and right ventral horns of each segment analysed. A two-way ANOVA confirmed no ipsilateral or contralateral effect of pTDP-43 positive MN numbers (Mi P=0.191; Ma P=0.107) but revealed an effect of segment (Mi P=0.00; Ma P=0.00).

To elucidate the intersegmental effects, pairwise t-tests were performed, comparing each segment to the combined two segments in each animal with fewer ChAT positive motoneurons (Mi: C6-C7; Ma: C7-C8), segments thought to supply the R-BR muscle. The *post hoc* tests revealed significant differences between the BR innervating segments and C1-C3 in Monkey Mi (C1 P<0.0001; C2 P<0.001; C3 P<0.001) and C2-C4 and T1 in Monkey Ma (C2 P<0.001; C3 P<0.01; C4 P<0.01; T1 P<0.0001). Higher numbers of pTDP-43 positive cells were recorded in the rostral cervical segments than in C6 and C7 in Monkey Mi whereas fewer pTDP-43 positive cells were counted in the rostral segments of Monkey Ma compared to C7 and C8. There were also fewer average pTDP-43 positive MNs in T1 in Monkey Ma than in the BR segments, consisting of C7 and C8. These differences survived the BH correction for multiple comparisons. No pTDP-43 expression was detected in the cervical spinal cord of a healthy age-matched control (Figure 6.3A, B). The expression seen in Monkey Mi and Ma was consistent with a pervasive 'prion-like' spread of this pathological protein throughout the spinal cord from the focal transfection site.

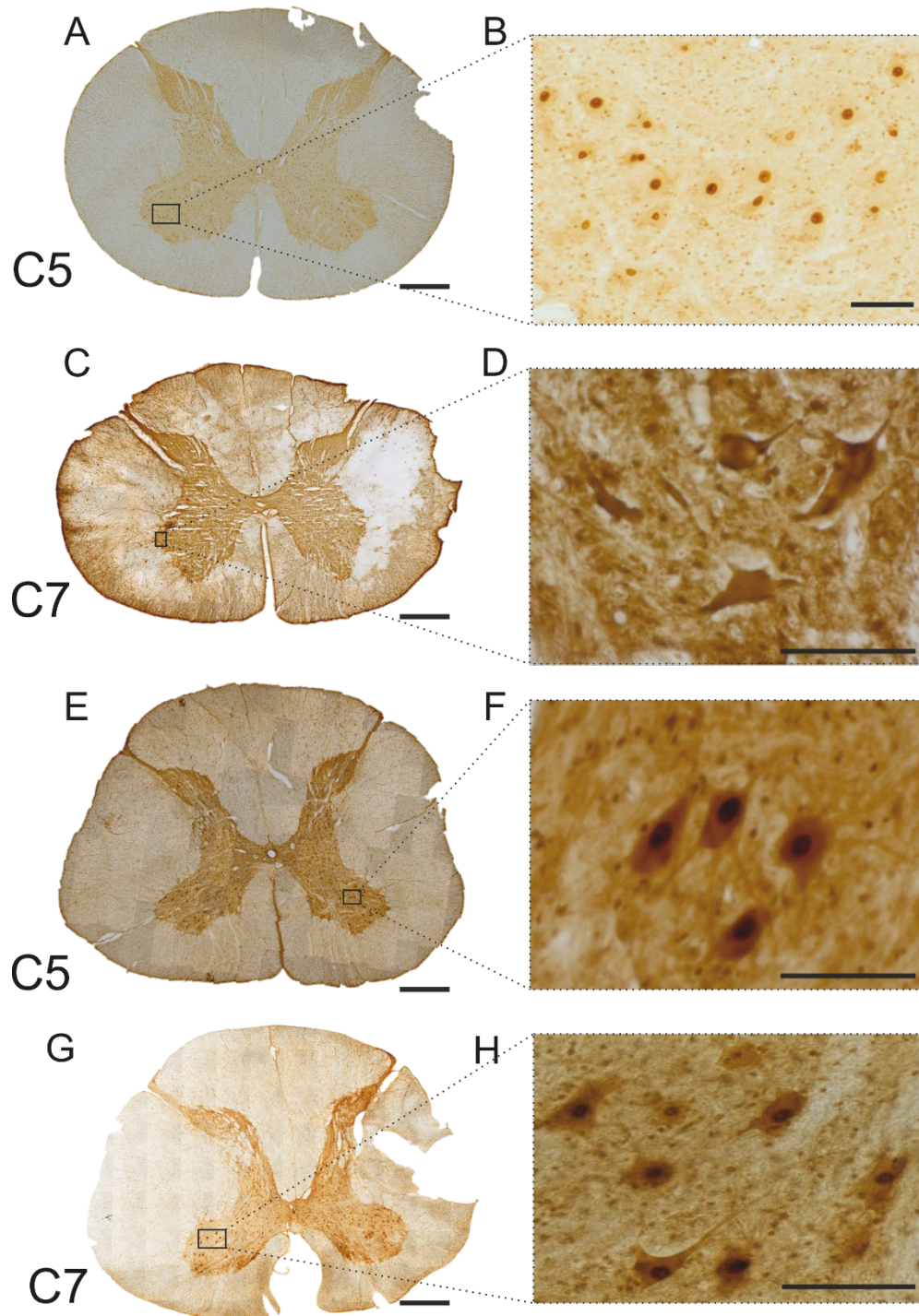
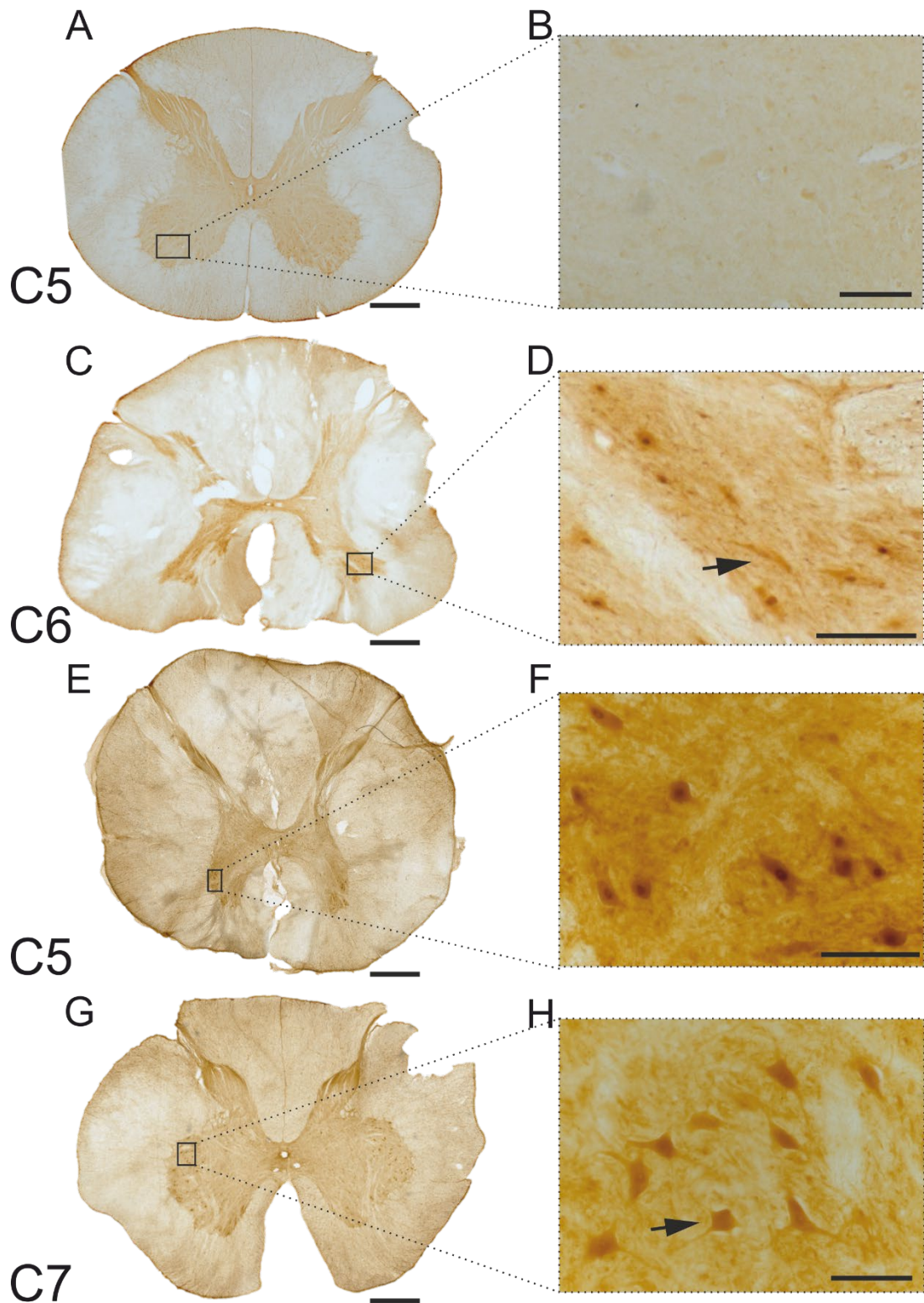
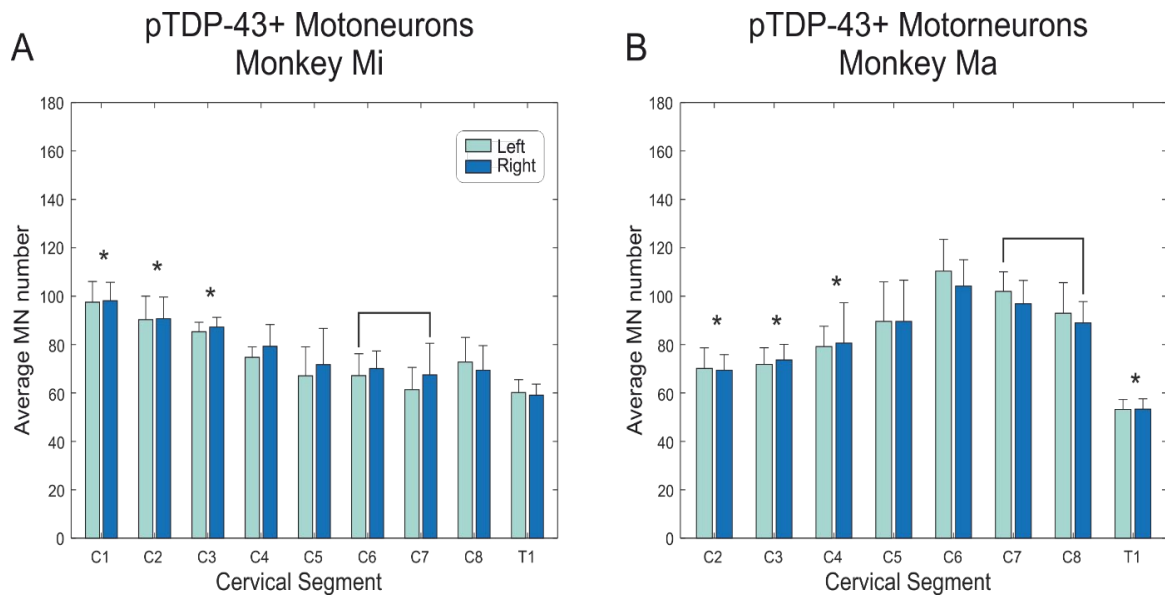


Figure 6.2. Spinal distribution of TDP-43, which is labelled in brown using DAB. A, control macaque, without virus transfection. Note the light staining, with TDP-43 restricted to the nucleus of motoneurons (enlarged view in B). C and G, Monkey Mi and Monkey Ma respectively, C7 segment which contains BR motoneurons. TDP-43 is widespread. Enlarged images of motoneurons (D and H) show dense staining in the cytoplasm, with visible clumps of TDP-43. E, Monkey Mi, C5 segment which does not contain BR motoneurons. Staining is still more dense than control. F, enlarged motoneurons show both cytoplasmic and nuclear TDP-43. Scale bars: 1000 $\mu$ m in low power images, 100 $\mu$ m in high power images.



*Figure 6.3. Spinal distribution of phosphorylated TDP-43, which is labelled in brown using DAB. A, control macaque, without virus transfection. Note the very light staining (enlarged view in B). C, Monkey Mi, C6 segment which contains BR motoneurons. pTDP-43 is widespread. Enlarged images of motoneurons (D) show staining in both nuclei and cytoplasm. E, Monkey Mi, C5 segment which does not contain BR motoneurons. Staining is more dense than in control, with both cytoplasm and nuclear staining in motoneurons (F). G and H, Monkey Ma, C7 segment which contains BR motoneurons. pTDP43 is*

widespread. *D* and *H*, nuclear staining was less prominent in MNs of segments which innervate the BR muscle (indicated by arrows), than more distant segments (*F*). Scale bars: 1000 $\mu$ m in low power images, 100 $\mu$ m in high power images.



*Figure 6.4. Phosphorylated TDP-43 is widely expressed in motoneurons of the cervical spine in transfected animals. pTDP-43 positive motoneuron counts for the two Monkeys infected with TDP-43 constructs. Sections were stained for TDP-43 phospho-Ser409/410 (pTDP-43). pTDP-43 positive cells within lamina IX of the spinal cord were counted in 12-18 sections per spinal segment (thickness 40 $\mu$ m), collected at 320-480 $\mu$ m intervals, to provide an estimate of pTDP-43+ motoneuron number. A two-way ANOVA showed no effect of side of the cord on the number of pTDP-43 positive cells, but a significant effect of segment. Post hoc t-tests revealed a significant differences between multiple segments in both animals compared to the combined segments in which a reduction of ChAT+ MNs was recorded (Mi: C6-C7; Ma: C7-C8) Segments significantly different to this group were marked with a star (\*). Interestingly, in Monkey Mi significantly more cells were recorded in the distant segments, while a reduction was recorded in Monkey Ma. The results are consistent with prion-like spread of 'pathological' pTDP-43 from the transfected motoneurons projecting to the right brachioradialis (BR) muscle, located in C6/C7/C8 segments, to neighbouring motor pools and also distant cervical segments bilaterally. Healthy age-matched control animals show no pTDP-43+ motoneurons throughout the spinal cord, and therefore no data was displayed for this animal.*

## **Discussion**

The results from this study demonstrate that a focal overexpression of healthy TDP-43 in a subset of spinal MNs is able to induce widespread changes in TDP-43 expression within adjacent and distant cells throughout the spinal cord. The extensive spread of TDP-43 pathology throughout adjacent, distant and contralateral motor pools supports the theory of a self-perpetuating prion-like action of this protein.

### ***Detection of transfected motoneurons***

A fluorescent tag, tdTomato, was included in the genetic payload of the rAAV2 virus administered intramuscularly in order to allow us to detect which spinal cells were retrogradely transfected. We have had previous success enhancing the detection of this expression for microscopy with the use of an antibody against the family of red fluorescent proteins (RFP), however, no tdTomato expression was identified the cervical segments C4-C8, understood to supply the BR muscle, in the two animals involved in this study (Figure 6.1A and B). The inability to identify this viral tag raises concerns over the validity of the results presented, as we cannot say with certainty that the virus has indeed crossed the neuromuscular junction (NMJ) to transfect the spinal MNs. It would be possible to detect the AAV vector RNA in homogenised spinal cord tissue by performing a quantitative real-time polymerase chain reaction (qRT-PCR) assay. While this would prove that both viruses successfully reached the cervical spinal cord, it would not be sufficient to determine whether they transfected the same cells. Furthermore, with the lack of virus tag and length of time between the injections and termination of the animal, it is unlikely that this technique could provide definitive results.

### ***Degeneration of spinal cord MNs***

Once the absence of viral tag had been identified in the spinal cord, we quantified the number of motoneurons (MNs) in each cervical segment, as well as the first thoracic segment due to its known innervation of forearm muscles involved in wrist and hand (Jenny and Inukai, 1983). In segments C6-C7 and C7-C8 in Monkey Mi and Ma respectively, a significant reduction in MNs was recorded in the right ventral horn as compared to the left. MNs innervating the right BR muscle are thought to be located in columns spanning these segments. This corresponding absence of fluorescent viral tag and reduction of MNs in these overlapping segments suggests that any doubly transfected MNs have degenerated in the seven months between transfection and termination. In addition to this focal loss, a

more general loss of MNs had possibly occurred in the segments closest to the site of transfection; C4-C8. The MN counts from the healthy control animal indicated the expected number per segment, and when compared to the counts from the two transfected animals made clear a marked reduction in Monkey Mi with a less prominent reduction in the aforementioned segments in Monkey Ma. This difference, particularly obvious between the control and Monkey Mi, suggested that a level of MN degeneration in segments within the cervical enlargement had already begun at the time at which the animal was terminated. The counts collected from Monkey Ma were closer to those of the control animal, which may suggest more severe pathology occurring in Monkey Mi compared to Ma.

### ***TDP-43 pathology is widespread throughout the cervical spinal cord***

In healthy tissue in normal conditions, the ubiquitously expressed TDP-43 is located in the nucleus with minor shuttling between the cytoplasm (Figure 6.2A and B). In the transfected macaques of this study, TDP-43 is highly expressed in the nucleus and cytoplasm of MNs in the left and right spinal cord ventral horns. This abnormal cytoplasmic expression was recorded in MNs throughout the rostrocaudal extent of the cervical cord and first thoracic segment, revealing extensive abnormal expression not limited to the segments innervating the right BR (Figure 6.2E and F). In addition to this, many large MNs from C6 to C8 segments exhibited a complete loss of defined nuclear staining as well as dense clusters of TDP-43 expression in the cytoplasm (Figure 6.2C, D, G and H). These expression patterns are consistent with cytoplasmic mislocalisation and accumulation noted in patient cases (Neumann et al., 2006, Brettschneider et al., 2014, Arai et al., 2006). The more substantial TDP-43 proteinopathies identified in the MNs in these segments, bilaterally, suggests that cells from motor pools adjacent to the transfected MNs were further along the degenerative pathway.

Although the expression pattern of TDP-43 in the cytoplasm of the cervical MNs is clearly abnormal in comparison to that of the control macaque, where it is strictly nuclear, it is important to define whether this TDP-43 is deemed 'pathological'. In MND, TDP-43 serine groups 409 and 410 have been recorded to become phosphorylated (pTDP-43) (Inukai et al., 2008). The detection of the pTDP-43 variation therefore allows us to detect any trace of pathology within the tissue. Similar to the 'functional' protein, pTDP-43 expression was detected in MNs of all analysed sections from the cervical and thoracic segments of the transfected macaques (Figure 6.2C-F). These findings confirm that the abnormal TDP-43 expression noted in these cells was in fact pathological, and thus similar to the

proteinopathies recorded in MND patients. This same histological process and analysis performed on a healthy control macaque cervical spinal cord confirmed that this expression was limited to the MNs of the transfected animals. No MNs in the cervical spinal cord of the age matched healthy control displayed any TDP-43 abnormalities, with expression restricted to the nucleus, and there were no pTDP-43 proteinopathies (Figure 6.2A and B). No statistical assessments or comparisons could be made using the control due to this complete absence of pathology.

Counts of MNs positive for pTDP-43 expression revealed no significant differences in the number of pathological cells in the right and left ventral horn of each spinal segment analysed. Given the reduction of ChAT positive MNs in the right ventral horn of spinal segments C6-C8, we might expect to see a corresponding reduction in pTDP-43 positive cells in these same segments. The uniform pTDP-43 expression in the left and right of these segments may suggest that there has been a greater level of pathological spread to the MNs in the immediately adjacent motor pools of the right ventral horn. It is possible that the surrounding MNs in the transfected segments were the site of first pathological spread, from which it has continued to disseminate evenly to more distant motor pools and across the central canal into left ventral horn MNs.

The intersegmental analysis may further support this idea of a graded spread of pathology outwards from the site of transfection. In Monkey Ma, there is a clear stepped gradient of pTDP-43 positive MNs outwards from the BR innervating segments, with average counts significantly lower in the three furthest rostral segments as well as in the caudal T1 segment. The lower number of pTDP-43 positive cells in T1 may suggest that pathology spreads caudally at a later stage, involves a different pathway or could in fact be representative of differences in the overall number of MNs per segment rather than indicative of varying levels of spread. The segmental pattern is quite different in Monkey Mi. While the same three most rostral segments are again significantly different to those in which a reduction of MNs was recorded, in this animal there are more pTDP-43 immunoreactive cells in these rostral segments.

The absence of the stepped appearance, and comparable number of pTDP-43 positive MNs in the more caudal cervical segments in this animal provides an interesting comparison to the perhaps more expected pattern recorded in Monkey Ma, described above. From our *in vivo* assessments, in particular the MR imaging (see Chapter III), we have a relatively clear

idea that the virus mediated denervation onset occurred six weeks earlier in Monkey Mi than in Monkey Ma. It is possible, therefore, that the pathology in Monkey Mi was more advanced. If this was the case, pTDP-43 positive cells in the segments containing the transfected motor pool may have already begun to degenerate, explaining the apparent reduction of pathological cells in these segments. More caudal MNs, within T1 for example, may have been in an earlier stage at the time of termination and therefore have not yet degenerated.

There is some histological evidence in the two transfected animals of pTDP-43 expression in small intermediate zone cells thought to be interneurons. These findings may suggest a role of segmental and propriospinal interneurons, with their bilateral, intra- and intersegmental projections crucial for the coordination of motor circuit activity throughout the cord, in the propagation of disease pathology (Matsuyama et al., 2006, Bannatyne et al., 2009, Butt and Kiehn, 2003). Indeed, previous studies have proven an involvement of interneurons in clinical and animal studies of MND, however the chronology of their degeneration is not yet understood (Hossaini et al., 2011, Oyanagi et al., 1989, Stephens et al., 2006)

The evidence of a reduction of MNs in the right dorsal horn of the segments containing the transfected motor pool, in combination with the lack of the fluorescent viral tag, provided evidence for the degeneration of the transfected cells. Any cells that presented with pTDP-43 pathology in the segments supplying the virus targeted muscle indicated that a secondary spread from the transfected cells has occurred. Due to the columnar arrangement of MNs, MNs of different motor pools are interspersed within the ventral horn, and therefore not all MNs located in these segments will supply the infected BR muscle. Further to this, TDP-43 abnormalities and pTDP-43 expression were identified in the large MNs of the left ventral horn, contralateral to the transfected motor pool and in motor pools in distant cervical segments. The extensive evidence of neuropathic changes in the MNs of the entire left and right cervical cord support the model of 'prion-like' cell to cell transmission of MND-like pathology.

The complete absence of viral tag is a cause for concern. It is to be expected that a proportion of the BR motoneurons would be transfected by only the retrograde virus rather than both viruses, and so would not express TDP-43. These cells should therefore express tdTomato but not degenerate. A possible explanation for the lack of this fluorescent tag in

the BR segments could be that cells with the tdTomato genetic payload were more fragile and degenerated early when filled with TDP-43 following a prion-like spread. The singly transfected cells in the BR motor pool may also have been the first cells targeted by the pathological spread, leading to their degeneration shortly after those initially transfected.

An alternative argument to a ‘prion-like’ spread of this proteinopathy could be spread of the virus itself, inducing widespread rather than focal TDP-43 transduction. However, if the rAAV2 virus, injected intramuscularly had reached the blood stream and spread in this way, we would have expected to see evidence of the fluorescent protein tdTomato throughout the CNS. Instead, no fluorescent tag was detected in any of the spinal segments or even in the cortex (data not presented in this thesis). Furthermore, a widespread transfection would not account for the selective reduction of motoneurons consistent with the site of the targeted motor pool. The most likely explanation for the widespread MND-like pathology, present only in the transfected animals, is a prion-like spread of pathology initiated by a focal overexpression of TDP-43.

# CHAPTER VII. Histopathological Changes in the Primary Motor Cortex of a NHP Model of MND

## Introduction

Motor commands are sent from the primary motor cortex (M1) to the spinal cord via the corticospinal tract (CST) to initiate and influence voluntary movement. CST neurons, located in M1 cortical layer V, have long axons which descend within this tract to terminate in the spinal cord. CST neurons have been identified in the M1 of humans and old world primates, which connect both directly and indirectly to spinal cord  $\alpha$ -motoneurons (MNs). Corticospinal (CS) neurons, conserved in most mammals, make indirect connections with MNs primarily via intermediate zone interneurons. A phylogenetically newer subtype of CS neuron, cortico-motoneuronal (CM) cells, first described by Bernhard and Bohm (1954), connect predominantly monosynaptically to spinal cord MNs in primates, providing a direct link between M1 neurons and spinal cord MNs (Rathelot and Strick, 2009, Witham et al., 2016). The CM cells also connect to spinal MNs disynaptically via segmental interneurons and propriospinal interneurons, located in C3-C4 spinal segments (Isa et al., 2007). CM cells are thought to play a crucial role in the development of dextrous finger and hand movements (Heffner and Masterton, 1975, Isa et al., 2013).

In their work to define the cortical origins of the direct CST pathway, Rathelot and Strick, identified two anatomical subdivisions within the macaque M1 (Rathelot and Strick, 2006, Rathelot and Strick, 2009). CST neurons were found in comparable numbers throughout M1, however by tracing their termination patterns the researchers were able to determine that different subtypes of CST neuron were found in distinct regions of M1. CST neurons which almost exclusively terminated monosynaptically onto intermediate zone interneurons were located in the rostral region of M1, while CM with direct connections to spinal MNs were instead primarily limited to the caudal region of M1, located within the bank of the central sulcus. A small number of CM cells were also identified in the primary somatosensory cortex, referred to as area 3a, but were proposed to connect to the  $\gamma$ -MNs involved in the fusimotor pathways (Rathelot and Strick, 2006). Widener and Cheney (1997) however, have provided evidence of an area 3a neuron producing post-spike facilitation in spike-triggered averages of electromyography data, suggesting a connection to  $\alpha$ -MNs.

The rostral and caudal divisions of the primary motor cortex, termed ‘old M1’ and ‘new M1’, were thus defined based on the presence, or lack thereof, of CM cells. The ‘new M1’ region therefore provides direct input of signals from the motor cortex to spinal cord MNs in addition to the integrative action of ‘old M1’, whose CS cells act on spinal cord interneurons to influence MNs indirectly. These anatomical divisions in the macaque M1 have been corroborated with electrophysiology, however recent investigations have challenged this strict boundary. Direct connections to spinal MNs have also been identified in the rostral ‘old M1’, however these monosynaptic inputs are from slower-conducting axons than the fast conducting CST axons which are indeed restricted to the more caudal ‘new M1’ (Witham et al., 2016). The presence of a similar ‘old’ versus ‘new’ anatomical divide in humans in the hand-knob region of the motor cortex has been confirmed with the use of histochemistry and direct electrophysiology (Geyer et al., 1996, Vigano et al., 2019, de Noordhout et al., 1999).

The occurrence of this anatomical M1 divide is correlated with the appearance and evolution of the CM system. The CS neurons and ‘old M1’ area in which they are found are conserved across many mammals and are thought to make up the traditional motor area (Nudo and Masterton, 1988). CM neurons and the ‘new M1’ area are more recently evolved features found exclusively in primates. Humans have the most developed CM system, followed by old world primates and some new world primates (Kuypers, 1981, Lemon, 2008). Other mammals, such as cats and rodents have no functional CM system (Illert et al., 1976, Alstermark and Ogawa, 2004).

The enhancement of the CM system in primates is correlated with the development of dextrous and ‘fractionated’ finger movements. Thus, primates with stronger, more developed CM connections to MNs are able to perform better in tasks requiring such skilled movements (Nakajima et al., 2000). Deficits in the capacity to produce fine finger movements can be fully appreciated when observing the fine motor abilities of rodents. Macaques are able to perform learnt dextrous tasks with 100% accuracy (Schmidlin et al., 2011), while rodents, who lack CM cells and so the direct monosynaptic connection between motor cortex and spinal cord motoneurons have a much more limited degree of manual dexterity (Gu et al., 2017). Lesions to the CST in Monkeys, disrupting the direct connection between the CM cells and MNs produce significant deficits in the animals’ ability to perform dextrous movements such as a precision grip (Isa et al., 2013, Tohyama et al., 2017). From these data, it is clear that the development of this direct monosynaptic

connection between motor cortex and spinal cord is crucial for the improvement of refined, voluntary movements.

The CM cells of the primary motor cortex comprise pyramidal cells of heterogeneous shape and size located in cortical layer Vb, including the giant cells of Betz, with their characteristically long, fast conducting axons and a volume three to twenty times larger than that of other pyramidal cells in human and macaque samples, and smaller projection neurons (Rivara et al., 2003, Bakken et al., 2021). These cells, often referred to clinically as upper motor neurons (UMNs), are selectively vulnerable and show specific pathology in Motor Neurone Disease (MND), a disorder characterised by the progressive degeneration of both the 'upper' and spinal and bulbar 'lower' motor neurons (LMNs). While the neuropathologies recorded in these two, distinct cell populations varies, they share a mutual selective vulnerability and early involvement in MND (Brettschneider et al., 2013).

Growing evidence implicates Betz cells and the CM system as important contributors to the development and spread of disease pathology in MND (Eisen et al., 2017). Many pathological changes have been recorded in Betz cells in MND, such as a reduction in soma size, degeneration of the apical dendrite, and ultimately loss of the cells during the course of the disease (Genc et al., 2017). Brettschneider et al. (2013) in defining the progression of neuronal histopathological features of this disease, have differentiated four stages of the sporadic disease. In the first stage, phosphorylated TDP-43 (pTDP-43), the pathological state of the normal nuclear protein 43-kDa trans-activating response DNA-binding protein, is found in the Betz cells of M1 and spinal and bulbar  $\alpha$ -MNs (Arai et al., 2006, Neumann et al., 2006). In both cell types, normal nuclear TDP-43 expression in the cell nucleus is lost, however in the Betz cells the pTDP-43 is noted by Braak et al. (2017) not to form into the cytoplasmic aggregates characteristically seen in  $\alpha$ -MNs. They suggest that the proteinopathy may be transmitted along the length of the axons of the Betz cells and across the synapse to the directly connected motoneurons, eliciting a 'prion-like' spread of disease throughout the motor system (Feiler et al., 2015, Fallini et al., 2012, Cushman et al., 2010).

There are differing theories regarding the direction of degeneration in MND, with some postulating that neuronal pathology, specifically TDP-43, present in the overwhelming majority of cases, progresses from the neuromuscular junction to the cortex while others argue that the onset is cortical in origin (Braak et al., 2013, Menon et al., 2015, Vucic et al., 2013). Either way, as integrators of motor information and an effective direct link

between the spinal cord and cortex, Betz cells are likely to play an important role in the progression and possibly spread of this unforgiving disease.

In this study we have quantified the number of pTDP-43 positive cells in ‘old-M1’ and ‘new M1’ throughout the mediolateral extent of M1 in the left and right hemispheres in two transfected macaques overexpressing TDP-43 in the spinal  $\alpha$ -MNs supplying only the right brachioradialis (BR) muscle. The identification of pTDP-43 expression in M1 neurons of these animals would indicate a prion-like spread of this protein from the spinal  $\alpha$ -MNs to the cerebral cortex. By analysing the expression of pTDP-43 throughout the left and right M1 hemispheres, we were able to determine whether spread had occurred, and whether it was limited only to CM cells likely directly connected to the BR MNs or whether the pathology was widespread.

## **Methods**

### ***Animals***

Tissue was collected from two chronically implanted adult female awake behaving Monkeys (*M. mulatta*; Monkeys Mi and Ma, age 6 years, weight 6.1 and 6.9kg at outset) and one healthy female control macaque (age 3 years). All animal procedures were performed under appropriate licences issued by the UK Home Office in accordance with the Animals (Scientific Procedures) Act (1986) and were approved by the Animal Welfare and Ethical Review Board of Newcastle University.

### ***Immunohistochemistry***

Following the completion of the study, the animals were anaesthetised to a lethal level by administering intravenous propofol. The animals were perfused through the heart with phosphate buffered saline (PBS) followed by 10% neutral buffered formalin (NBF). The cortex, cerebellum, brainstem and spinal cord were removed and immersed in 10% NBF for 16 hours at 4°C before progressing through ascending concentrations of PBS sucrose (10%, 20%, 30%) for cryoprotection. Blocks containing the mediolateral extent of the left and right sensorimotor cortex were removed. A freezing sledge microtome (8000-01, Bright Instruments Co. Ltd, United Kingdom) connected to a solid state freezer (53024-01, Bright Instruments Co. Ltd, United Kingdom) was used to cut the cortical blocks into 60µm parasagittal sections (total length along sulcus sectioned: Monkey Mi RM1: 18,180µm, LM1: 18,180µm; Monkey Ma RM1: 19,320µm, LM1: 18,600µm). All sections were stored free floating in PBS at 4°C until further processing.

### ***Functional TDP-43***

Sections were collected at 1440µm intervals along the mediolateral axis of the central sulcus for TDP-43 immunostaining (10782-2-AP, TDP-43 Polyclonal antibody, ProteinTech; 1:2000). Sections were washed with 0.1M PBS before being incubated with 3% H<sub>2</sub>O<sub>2</sub> for 5 minutes to quench any endogenous peroxidase activity. Following this, the sections were washed with PBS a further 3 times. Primary antibody dilutions were performed using a PBS solution containing 0.3% Tween-20 (Sigma-Aldrich) and 5% goat serum (Vector Laboratories). A rabbit anti-TDP-43 polyclonal antibody (ProteinTech; 1:2000) was applied to the sections overnight at 4°C. The following day the sections were washed three times with PBS prior to a 30 minute incubation with an ImmPRESS HRP goat anti-rabbit IgG polymer reagent (MP-7451, Vector Laboratories) at room temperature.

The sections were again washed with PBS 3 times to remove any residual secondary antibody. A DAB substrate (3,3'-diaminobenzidine) (SK-4100, Vector Laboratories) was applied to the sections until a desired stain intensity developed (2 minutes). The DAB substrate produces a brown precipitate in the presence of the peroxidase (HRP) enzyme. Tap water was applied to the sections for 5 minutes to quench the reaction. At this point sections were mounted onto Superfrost Plus slides (Thermo Scientific) and allowed to air dry. Sections were dehydrated in ascending ethanol solutions (70%, 90%, 100%) and cleared in histoclear for 10 minutes. Sections were coverslipped with VectaMount (Vector Laboratories).

### ***Phosphorylated TDP-43***

Sensorimotor cortex sections were collected at 720 $\mu$ m intervals for phosphorylated TDP-43 (pTDP-43) immunostaining (CAC-TIP-PTD-M01, Anti TAR DNA-Binding Protein 43 (TDP-43), phospho-Ser409/410 mAb (Clone 11-9), CosmoBio Ltd; 1:500) (Inukai et al., 2008). Sections were washed with 0.1M PBS before a 3% H<sub>2</sub>O<sub>2</sub> incubation for 5 minutes to quench any endogenous peroxidase activity. Following this, the sections were washed with PBS a further 3 times. Primary antibody dilutions were performed using a PBS solution containing 0.3% Tween-20 (Sigma-Aldrich) and 5% goat serum (Vector Laboratories). A mouse anti-TDP-43 phospho-Ser409/410 polyclonal antibody (CosmoBio Ltd; 1:500) was applied to the sections overnight at 4°C. The following day the sections were washed three times with PBS prior to a 30 minute incubation with an ImmPRESS HRP goat anti-mouse IgG polymer reagent (MP-7452, Vector Laboratories) at room temperature. The sections were again washed with PBS 3 times to remove any residual secondary antibody. A DAB substrate (3,3'-diaminobenzidine) (SK-4100, Vector Laboratories) was applied to the sections until a desired stain intensity developed (2 minutes). Tap water was applied to the sections for 5 minutes to quench the reaction. At this point sections were mounted onto Superfrost Plus slides (Thermo Scientific) and allowed to air dry. Sections were dehydrated in ascending ethanol solutions (70%, 90%, 100%) and cleared in Histoclear for 10 minutes. Sections were coverslipped with VectaMount (Vector Laboratories).

### ***Neuron labelling***

Cortical neurons were labelled with the classical neuronal marker NeuN (ab104225, abcam; 1:1000) (Gusel'nikova and Korzhevskiy, 2015). Primary antibody dilutions were performed using a PBS solution containing 0.3% Tween-20 (Sigma-Aldrich) and 5%

donkey serum (Bio-Rad Laboratories). A rabbit anti-NeuN polyclonal antibody (ab104225, abcam; 1:1000) was applied to the sections overnight at 4°C. The sections were washed in PBS 3 times before a donkey anti-rabbit Alexa Fluor 488 (ab150073, abcam; 1:1000) was applied as a secondary antibody for 2 hours at room temperature. The sections were shielded from light during the secondary incubation and for all subsequent steps to prevent bleaching of the signal. The sections were again washed 3 times in PBS before being mounted onto Superfrost Plus slides (Thermo Scientific) and coverslipped with Fluoroshield mounting medium with DAPI (abcam).

### ***Microscopy and Quantification***

Betz cells were identified based on their location in layer V of the motor cortex and their large pyramidal cell body. All brightfield and widefield images were acquired using a Zeiss AxioImager (Carl Zeiss AG, Oberkochen, Germany) which allowed for the capture of high magnification images as well as tiling using a 10x objective. For analysis, the primary motor cortex was divided into ‘old M1’ and ‘new M1’ based on anatomical landmarks previously described by Rathelot and Strick (2009) and Witham et al. (2016). The presence of the giant pyramidal Betz cells was used to demarcate the most rostral border of ‘old M1’ and most caudal border of ‘new M1’ for each section analysed. Betz cells positive for pTDP-43 immunoreactivity within these regions were counted in every 12<sup>th</sup> section throughout the mediolateral extent of the motor cortex (every 720µm) using the ImageJ Cell Counter tool (O’Brien, 2016). The number of counted cells were averaged for each area. In order to account for differences in size of ‘old M1’ and ‘new M1’, the density of pTDP-43 positive cells was measured. Cell density was calculated by dividing the number of counted cells per section by the rostrocaudal length of layer Vb, measured in ImageJ. Before the length could be measured, each image was spatially calibrated to convert the number of pixels into a real distance in microns (µm). pTDP-43 positive Betz cells were considered to be displaying MND-like pathology.

### ***Statistical analysis***

Data were analyzed using custom scripts written in the MATLAB environment (R2020a, MathWorks). Statistical tests were performed using MATLAB. Unpaired t-tests were used to compare counts from different hemispheres and between cortical subdivisions. The significance level was set at  $p < 0.05$ .

## Results

The primary motor cortex (M1) of two animals transfected with a combination of viruses designed to induce the over expression of the protein TDP-43, responsible for the majority of motor neurone disease (MND) pathology, in a focal pool of spinal motoneurons (MNs), was analysed histologically to determine whether pathology is able to spread backwards throughout the central nervous system. Staining for an antibody against the functional N-type TDP-43 in the left and right M1 revealed a high level of expression in the large Betz cells in cortical layer Vb (Figure 7.1C-F). This expression was not solely limited to the cell nucleus but rather was also present at a high level throughout the cytoplasm of these cells. This band of TDP-43 positive cells was also present in the control macaque tissue, suggesting that Betz cells have a high level of functional TDP-43 expression even in healthy animals.

To determine whether any proteinopathies were present in the M1 of the transfected animals the tissue was stained for an antibody against the pathological phosphorylated TDP-43 serine groups 409/410 (pTDP-43) (Inukai et al., 2008). A band of pTDP-43 expression was identified in a region consistent with cortical layer Vb, where the large cells of Betz' are located. This expression was limited to the cytoplasm of the giant neurons, with little to no expression present in the cell nucleus (Figure 7.2C-E). The expression appeared uniform throughout the cytoplasm and did not show any signs of aggregation or clumping, consistent with the findings of Braak et al. (2017) that proteinopathies of the Betz cells or upper motor neurons differ from those of the  $\alpha$ -motoneurons of the spinal cord and bulbar motor nuclei. No pTDP-43 expression was detected in M1 of the healthy macaque, suggesting that the transfection of the spinal cord MNs was essential for the expression of this pathological protein (Figure 7.2A and B).

The number of Betz cells positive for the expression of the pathological pTDP-43 protein were counted within manually defined subdivisions of M1. Anatomical markers previously described by Rathelot and Strick (2009) were used to define the boundary between the more rostral 'old M1' and caudal 'new M1', and the presence of giant Betz cells, or lack thereof, used to define their outer borders (Figure 7.3A). pTDP-43 positive cells within cortical layer Vb, consistent with the location and size of Betz cells, were counted in 15-22 sections spanning the mediolateral extent of each M1 hemisphere per animal (thickness 60 $\mu$ m), collected at 540-720 $\mu$ m intervals, to provide an average count of pTDP-43 positive Betz cells per slice number (Figure 7.3). A higher number of pTDP-43 positive Betz cells were

counted in 'new M1' than 'old M1' in both transfected animals. Significantly more pTDP-43 positive cells were recorded in the right hemisphere of 'new M1' compared to the left hemisphere in Monkey Ma ( $P=0.0188$ ) (Figure 7.3B). No significant differences were recorded between the right and left hemispheres of Monkey Mi. Counts of pTDP-43 positive cells were zero in both M1 area in the healthy control animal, and hence no statistical comparison between the transfected animals and control could be made.

In order to account for differences in size of the 'new M1' and 'old M1', we calculated the density of pTDP-43 positive cells in each region to allow for a more direct comparison of the areas. The number of cells positive for the expression of the pathological protein was divided by the recorded length of layer Vb in each area. The density of pTDP-43 positive cells was significantly higher in the 'new M1' subdivision as compared to the right 'old M1' subdivision in the left hemispheres of both Monkey Mi ( $P=0.0359$ ) and Monkey Ma ( $P=0.0037$ ), while no difference between these subdivisions was recorded in the right hemisphere (Figure 7.3C).

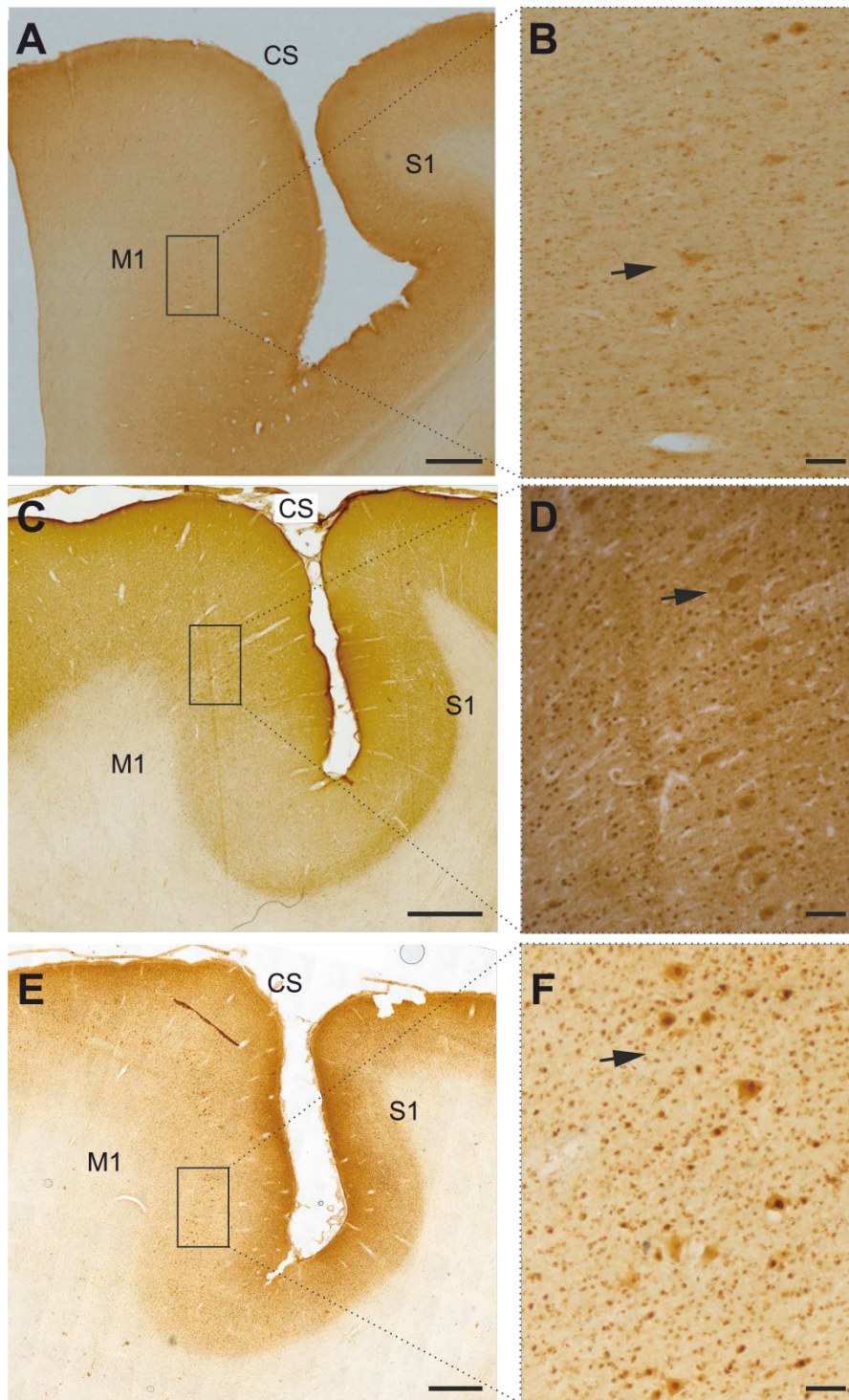
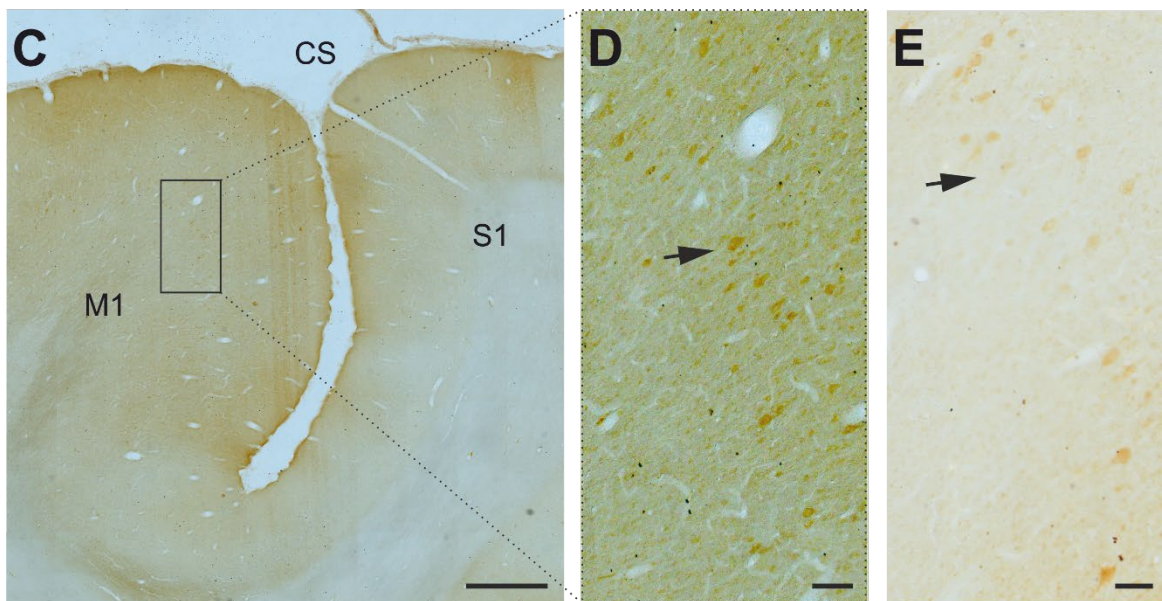
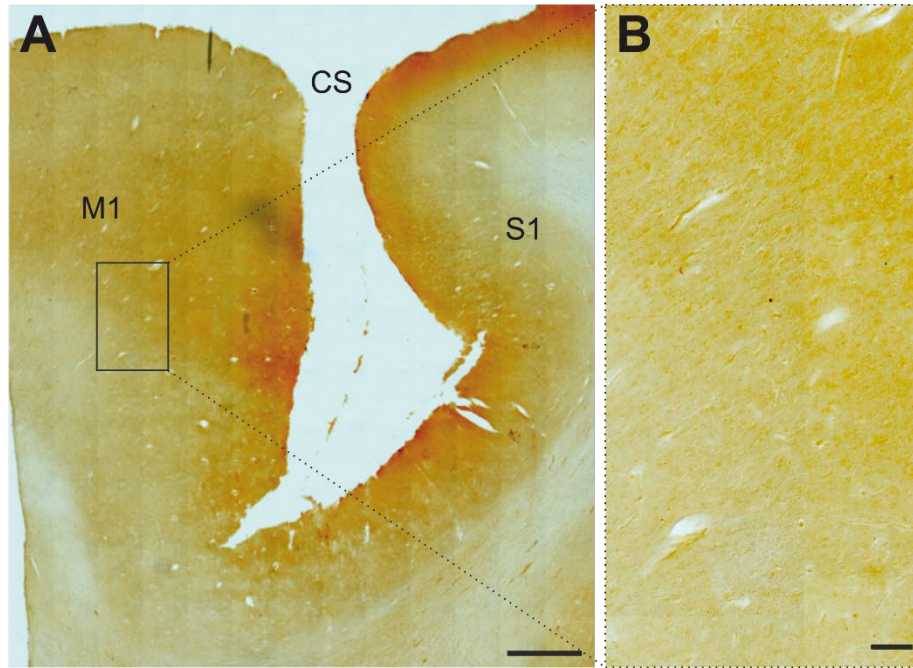
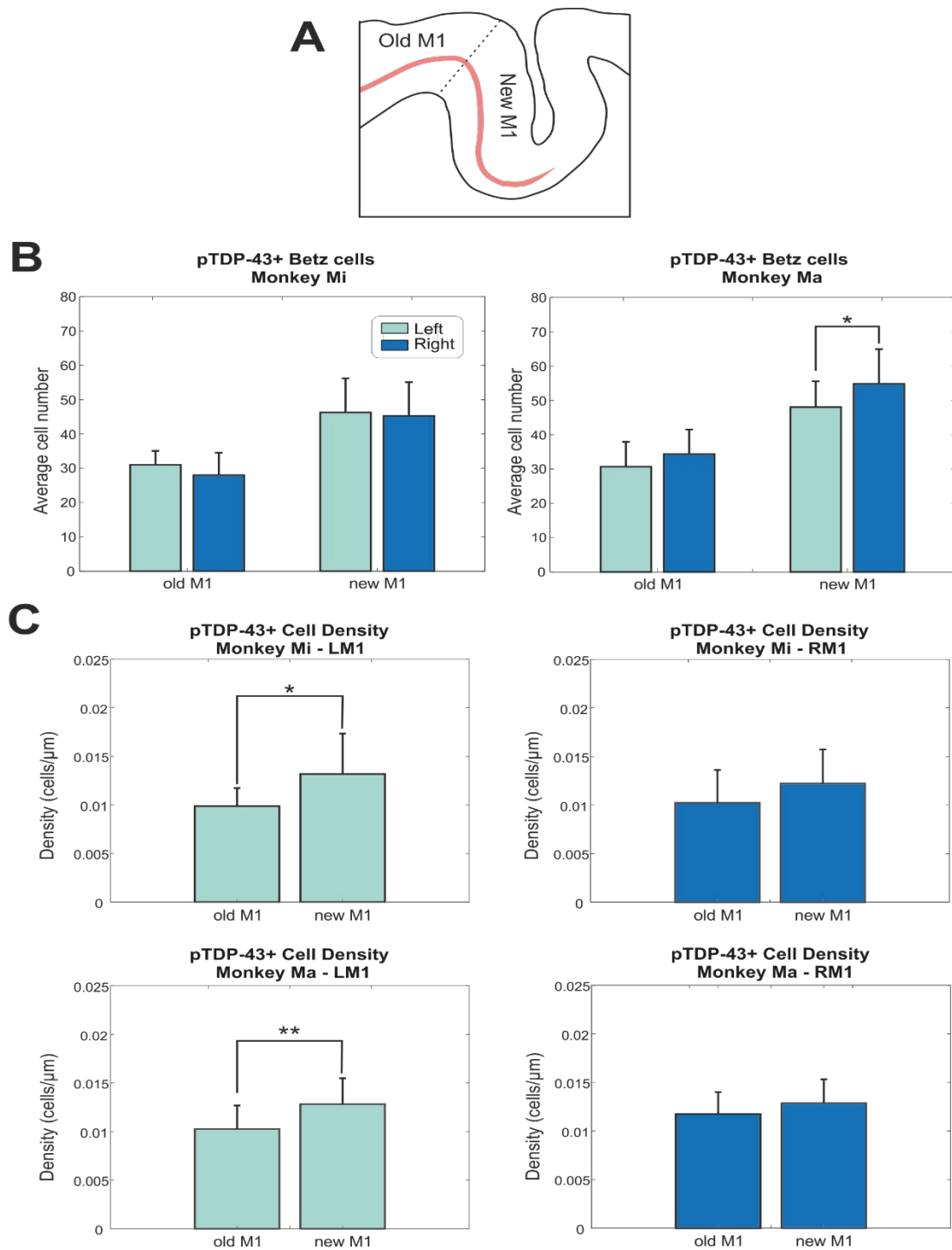


Figure 7.1. TDP-43 in the sensorimotor cortex. Images show parasagittal sections of the cortex in the region surrounding the central sulcus (CS). Pre-central (primary motor cortex, M1) and post-central (primary somatosensory cortex, S1) are labelled. Sections have been stained to label TDP-43 in brown, using DAB. A, for a control macaque, without virus transfection. Note the very light staining (enlarged view in B), largely confined to nuclei, although the Betz cells of M1 seem to have low levels of cytoplasmic TDP-43. Betz cells are large pyramidal cells in layer V, and are likely to project to the corticospinal tract. C and E, Left M1 of Monkey Mi and Monkey Ma, which had received the double virus injection shown in Figure 2.1. Staining is more dense, with clear cytoplasmic staining of Betz cell cytoplasm and nuclei in the enlarged image (D and F). Arrows indicate TDP-43<sup>+</sup> Betz cells in cortical layer Vb. Scale bars: 1000 $\mu$ m in low power images, 100 $\mu$ m in high power images.



*Figure 7.2. Phosphorylated TDP-43 in the sensorimotor cortex. Images show parasagittal sections of the cortex in the region surrounding the central sulcus (CS). Pre-central (primary motor cortex, M1) and post-central (primary somatosensory cortex, S1) are labelled. Sections have been stained to label pTDP-43 in brown, using DAB. A, for a control macaque, without virus transfection. Note the uniform staining (enlarged view in B), with no cells visible. C, representative section from left M1 of monkey Mi, which had received the double virus injection shown in Figure 2.1. Staining is more dense, with clear cytoplasmic staining of Betz cell cytoplasm and nuclei in the enlarged image (D). E, An identical staining pattern is seen in left M1 of monkey Ma. Arrows indicate pTDP-43<sup>+</sup> Betz cells in cortical layer Vb. Scale bars: 1000 $\mu$ m in low power images, 100 $\mu$ m in high power images.*



*Figure 7.3. Phosphorylated TDP-43 (pTDP-43) is widely expressed in the large Betz cells of cortical layer Vb of the primary motor cortex (M1) in two transfected animals. A, B, pTDP-43 positive Betz cell counts in the subdivisions of M1, ‘old’ and ‘new M1’. Sections were stained for TDP-43 phospho-Ser409/410 (pTDP-43). pTDP-43 positive cells within cortical layer Vb were counted in 15-22 sections spanning the mediolateral extent of the M1 per hemisphere per animal (thickness 60 $\mu\text{m}$ ), collected at 540-720 $\mu\text{m}$  intervals. Higher numbers of pTDP-43 positive Betz cells were counted in new M1 of both transfected animals. A significantly higher number of pTDP-43 positive cells were counted in the right ‘new M1’ subdivision compared to the left ‘new M1’ area of Monkey Ma ( $P=0.0188$ ). C-*

*F, pTDP-43 positive cell density was calculated by dividing the number of cells positive for the protein expression by the length of layer Vb. pTDP-43 positive cell density was significantly higher in the left hemispheres of both Monkey Mi ( $P=0.0359$ ) and Monkey Ma (0.0037), while no difference was recorded in the right hemisphere. These results are consistent with a 'prion-like' spread of 'pathological' pTDP-43 from the transfected motoneurons projecting to the right brachioradialis (BR) muscle, located in C6/C7 segments, to the distant Betz cells of the left and right M1.*

## Discussion

In this study, we have shown that TDP-43 overexpression within a focal spinal motor pool is capable of inducing a MND-like pathology throughout the right and left primary motor cortices in two female macaques. These results provide the first conclusive evidence of a 'prion-like' spread of this protein in NHPs, implicating this protein in the propagation of pathology in MND.

Much previous research has implicated the direct branch of the corticospinal tract (CST), which connects the corticomotoneuronal (CM) cells of the primary motor cortex and the spinal  $\alpha$ -MNs, in the spread of neuropathology in motor neurone disease (MND). This direct, monosynaptic connection is the only link between these two, otherwise distinct and distant neuronal subtypes which are both involved in the earliest stage of the disease (Brettschneider et al., 2014). This direct connection is an evolutionary development specific to dextrous primates. In order to recapitulate the disease process and accurately examine the role this direct pathway may play in disease propagation, a suitable model organism must be used. Failures of translatability of previous research into this disease may be due in part to the use of inappropriate model animals, such as rodents, which lack this direct monosynaptic connection between the two primarily affected cells in this disease. The use of macaques, which have also evolved this CM pathway, as a model organism allows us to study this disease in a much more physiologically accurate system, thus reliably assessing the involvement of this pathway and the cells that it links in MND.

In two non-human primates (NHPs), the spinal motor pool supplying the right brachioradialis (BR) muscle was transfected using a novel, dual virus approach to induce the overexpression of the healthy human protein TDP-43. TDP-43 has long been implicated in this disease, with pathological inclusions and abnormalities found in the majority of all familial and sporadic cases of MND. The animals were terminated seven months post injection and histologically analysed for signs of neuropathology throughout the central nervous system in order to determine the presence of spreading proteinopathies. Until now, despite much debate on the topic, there has been no definitive evidence that this protein spreads between cells in a 'prion-like' fashion.

High expression of the functional N-type TDP-43 protein was observed in the large cells located in M1 layer V. These cells are consistent with the morphology, size and location of the giant cells of Betz (Rivara et al., 2003). These cells, with their giant soma and long

axons, are thought to be one of the main sources of descending motor input to the distant motoneurons and interneurons of the spinal cord (Catsman-Berrevoets and Kuypers, 1976). This expression was present at high levels in both the nucleus and the cytoplasm of these cells, in the model animals and in the healthy control macaque M1 (Figure 7.1A and B). Interestingly, despite this cytoplasmic TDP-43 expression in the healthy macaque, no pathological pTDP-43 was found in the M1 of this animal, signifying that Betz and large pyramidal cells have a higher baseline functional cytoplasmic TDP-43 concentration (Figure 7.1A and B). This cytoplasmic expression may be involved in the regulation of axonal growth and maintenance, providing an explanation of why these cells with their lengthy axons may require a higher cytoplasmic expression than previously thought (Fallini et al., 2012). Taken together, these observations suggest a higher baseline cytoplasmic TDP-43 expression which may in turn contribute to the selective vulnerability of these cells to the exposure of TDP-43 pathology.

In the transfected animals, pTDP-43 was expressed in these same large cells located all along M1 cortical layer Vb (Figure 7.2C-E). Much less nuclear staining was observed as compared to the functional TDP-43. This observation corresponds to the literature which states that pTDP-43 proteinopathies appear less often as dense aggregations in the Betz cells but rather as nuclear clearance and general cytoplasmic and axonal accumulation (Braak et al., 2017). Betz cells expressing the pathological phosphorylated TDP-43 were found throughout the mediolateral extent of both the left and right hemispheres. As no pTDP-43 was identified in the healthy control macaque M1, we can be certain that the pathology is linked to the virus mediated TDP-43 overexpression in the spinal cord  $\alpha$ -MNs.

Betz cells expressing this pathology were quantified in order to help elucidate the pathway by which the disease is spread. By subdividing M1 into its functionally separate 'old' and 'new' territories, we hoped to identify whether the direct and indirect branches of the CST play differing roles in disease transmission. pTDP43 expression was found in cells of the 'old' and 'new' M1, in which the direct and indirect CS neurons are located. Both pathways, therefore, may facilitate the spread of this proteinopathy, or perhaps the direct CM connection, with its fast conducting axons in 'new M1' and slower axons in 'old M1' may primarily be involved. The number of pathological cells in the cortical subdivisions are even between the left and right hemispheres in Monkey Mi, but in Monkey Ma there were significantly more pTDP-43 positive cells in the right 'new M1' than in the left 'new M1'.

One possible explanation for this could be that cells in the left hemisphere are further advanced in the degenerative process compared to those on the right leading to their loss.

There was a greater density of giant Betz cells expressing the pathological protein, pTDP-43, in 'new M1', the site of the direct, fast-conducting CM cells, than in the 'old M1' in the left cortex of both animals. This significant difference was not present in the right cortices. This suggests that the left new M1, which contains the cells monosynaptically connected to the transfected motoneurons that supply the right brachioradialis muscle, received more of the pathological protein than the other subdivision of M1 or the other hemisphere. This can only be the case if the pathology is spreading preferentially via the direct CST pathway mediated by the CM-MN link. At this point, the pathology may have spread throughout the mediolateral extent of the cortex and to the contralateral hemisphere. As no other significant differences were found it seems logical to think that following this initial spread to the left 'new M1', the spread outwards to the other regions occurs at a comparable rate. It is unclear at this point whether the secondary spread originates from the CM cells, modelling a corticofugal spread and 'dying-forwards' mechanism proposed by Eisen and Weber (2001), or whether the spinal MN and interneuron circuitry is recruited to aid the spread further to more distant 'new M1' CM cells and the 'old M1' CS cells. The ability of TDP-43 neuropathology to spread 'backwards' from the MNs to the motor cortex is evidenced in this model, and further bolsters the idea of a 'dying-outwards' model of MND neurodegeneration in which the synapse itself is a key site of vulnerability (Baker, 2014).

In this novel model of MND, we have proven that TDP-43 overexpression in a subset of spinal  $\alpha$ -MNs is sufficient to induce a widespread cascade of pathological phosphorylated TDP-43 throughout the primary motor cortex. This spread targets the giant Betz cells, and primarily those located within the 'new M1' subdivision, known to be the source of the direct CM pathway. This spread is not limited to just the cortical region representing the BR muscle, but instead is widespread throughout M1 demonstrating considerable 'prion-like' propagation of the disease pathology.

## CHAPTER VIII. General Discussion

The development of an animal model which accurately recapitulates the symptomatic and histopathological complexities of MND is essential to our understanding of this disease. Anatomical variability between species must be taken into account when selecting the appropriate model animal. Rodents are primarily used for the study of this disease, however they lack the crucial monosynaptic connection that links the two principally involved cell populations; the corticomotoneuronal (CM) cells located in the primary motor cortex, and the  $\alpha$ -motoneurons of the spinal cord and brainstem cranial nuclei. This pathway is exclusive to primates, and especially developed in humans. Furthermore, there are fundamental genetic differences between humans and rodents. With their mostly conserved anatomy and network organisation, the next best organism to humans in which to study a human disease, is likely to be a non-human primate.

We hypothesised that inducing the overexpression of TDP-43, the protein implicated in and found within the pathological proteinaceous inclusions in ~97% of sporadic and familial MND cases, in a focal population of spinal motoneurons innervating one selected muscle would be sufficient to generate pathology within those cells similar to that seen in MND patients. The detection of phosphorylated TDP-43 (pTDP-43) proteinopathies in additional cell populations within the spinal cord, or further afield in the motor cortex, without evidence of widespread AAV action, would be taken as an indication that TDP-43 pathology is able to spread from a focal site. Evidence of cell-cell transmission between contiguous, non-contiguous or both populations may provide further support for a prion-like mechanism of pTDP-43 spread (Nonaka et al., 2013). The selected cell populations targeted by the spread of pathology may signal which pathways these proteinopathies are capable of utilising for their cell-cell propagation.

Additionally, we employed an array of *in vivo* assessments of muscle health and function in order to determine whether such techniques would be able to detect signs of onset of pathology in the virus targeted motoneuron population, manifesting as muscle weakness and denervation, followed by progressive deterioration in the innervated, neighbouring and distant muscles. These *in vivo* measures were to allow for real time assessment of the development of pathology, limiting the necessity for sequential culling to assess progression of pathology, a necessity in many animal studies, and have the potential for better translation into patient studies if validated.

## ***MRI***

Structural MRI scans have long been used to assess cortical thinning and, more recently, structural differences in the motor cortices have been used to distinguish MND patients from healthy controls (Roccatagliata et al., 2009, Ferraro et al., 2017). In addition to these cortical assessments, scans of the muscles elucidate processes related to on-going degeneration and denervation in MND patients, and have been proposed as a disease biomarker (Jenkins et al., 2020). Many variations of diffusion tensor imaging scans have been used to determine the health and stability of the muscle fibres. T2-weighted RARE scans detect fluctuations in proportion of water within a muscle, displaying increases in fluid dynamics as an increase in signal. Following denervation, the cytoarchitecture of a muscle is thought to become destabilised and reorganise, leading to an increase in signal detected with these scans (Kamath et al., 2008).

T2 weighted scans detected bands of high signal in the transfected right brachioradialis muscle of both animals, which progressively worsened and spread throughout the muscle before recovering. The signal fluctuations occurred later than would be expected for inflammation associated with the needle penetrations and from the intramuscular virus injections and virus-related immune response, and also differed from the diffuse signal increase recorded in the entire extensor compartment following an accidental injury to the right radial nerve of one of the animals. It is therefore likely that this increased signal represented the onset of virus mediated denervation in the muscle. The recovery of this signal, which occurred approximately eight weeks after the onset in both animals, was most likely indicative of compensatory reinnervation. Of note, while the time of onset differed between the two animals, the duration and spatial progression throughout the muscle followed an identical pattern. No further indication of denervation was recorded in either the virus-targeted muscle or any of the other forearm muscles. The virus induced TDP-43 overexpression likely provoked wide scale destabilisation throughout the R-BR, however later more gradual reorganisation caused by progressive spread may not have generated a sufficiently extensive or coordinated event to be resolved with this technique. Alternatively, the animals may have been terminated before denervation caused by the spread had developed.

## **Electromyography**

Increased importance is being placed on the use of electrophysiological techniques for the facilitation of MND diagnoses. The identification of fasciculation potentials and motor unit number estimation (MUNE) analysis are commonly employed in clinical settings currently, however such techniques can be unreliable and costly on time. A range of electrophysiological techniques were applied to validate the model while simultaneously assessing the ability of these techniques to identify changes in a muscle exhibiting MND-like pathology. Time considerations and requirements of voluntary input from the test subject, to either produce set movements and forces, or to remain strictly at rest, render many of the clinical electrophysiological assessments impractical for use in non-human primates.

A behavioural task involving the voluntary flexion of the elbow within a set force range allowed us to study voluntary electromyography (EMG) activity in a range of upper limb muscles, including the transfected muscle, over several months. Unlike the MRI findings, the EMG changes were not limited to virus targeted muscle. Individual muscle changes were highly variable, which is generally unsurprising due to the myriad ways in which the animals may engage their muscles to perform the task. From this task related muscle activity, we were able to detect limb-wide changes replicated in the experimental limbs of both animals as well as the contralateral ‘control’ limb. Interestingly, the discrepancies in muscle activity were not progressive but rather phasic in their appearance. These phasic changes were temporally conserved between animals and experimental and control limbs, indicating a replicable pathogenesis occurring in both animals. These data provided the first indication of a widespread malfunctioning of spinal motoneurons. These changes may represent a step of dysfunction occurring prior to motoneuron degeneration, perhaps involving the spinal, and even cortical, circuitry as a whole.

## **Nerve stimulation**

Nerve conduction studies are regularly performed clinically to exclude other motor disorders during MND diagnosis and to ascertain which muscles are affected but pre-symptomatic. Using surface stimulating and recording electrodes these tests can be performed easily in clinics, however some techniques such as MUNE are extremely time intensive, or in the case of MUNIX require patients to exert various ranges of force, an aspect they may struggle with at later stages of disease. Application of these techniques in

animal studies allows for the use of chronic electrodes, enabling the consistent sampling of the same motor units. Adaptations are required for the replication of these protocols in animal studies in order to accommodate for shorter experimental times and limit the necessity of subject input. For example, patients are often required to produce voluntary contractions within defined ranges, or in some cases to suppress their voluntary activity entirely.

The maximal CMAP amplitude is often regarded clinically as insufficient in isolation to determine changes in the health of the motoneurons. The infrequent testing clinicians are often restricted to does not allow for the detection of transient changes in CMAP amplitude during on-going denervation and reinnervation. Applying this technique weekly in our experimental animals, we were able to detect phases of increased and decreased CMAP amplitude over the course of several months, each separated by intermittent recovery of amplitude. These changes were predominantly detected in the radial nerve innervated muscles in both the transfected and control limbs.

There are various methods of applying MUNE analysis, each depending on a particular method of motor unit action potential (MUAP) extraction. The time consuming nature of individual MUAP identification and necessity for restriction of voluntary activity does not suit research involving awake animals. We applied an adapted MUNE protocol in which MUAPs decomposed during the voluntary task could be used to generate an average MUAP. Issues with number and amplitude of MUAPs successfully decomposed by the algorithm led to highly variable estimations. Without further validation of these methods and comparisons to the true MU numbers per muscle, it is unclear whether these numbers represent over or underestimations. It seems clear from these studies that MUAPs decomposed during high force voluntary activity do not represent the average MUAP of a muscle, although it could equally be said that neither do MUAPs detected from low stimulus intensities (Boe et al., 2005).

## **Histopathology**

MND is characterised by the degeneration of CM cells of the motor cortex along with spinal and bulbar  $\alpha$ -motoneurons. These distinct and distant cell types are functionally connected by their combinatory role in the direction of movement and physically connected both directly and indirectly by means of the corticospinal or corticobulbar tracts and local interneuron circuitry. These cell types develop pTDP-43 pathology in the earliest stage of

disease, and explain the deficits in dextrous movement and development of weakness and atrophy displayed by patients. The mechanisms of action by which this ubiquitous protein becomes pathological and spreads between different neuronal populations in MND are as yet unclear.

By inducing the overexpression of human wild-type TDP-43 in a focal population of spinal motoneurons, with the use of a novel dual virus approach, we were able to prove that the overexpression was sufficient in and of itself to induce the conversion of endogenous TDP-43 into pathological phosphorylated TDP-43. Evidence of phosphorylated TDP-43 was found not only in the originally transfected cells, but also in neighbouring and distant cells following the transfection. Pathological pTDP-43 expression was identified throughout the cervical spinal cord in adjacent and remote motoneuron pools, and in cells anatomically consistent with interneurons, in both the ipsilateral and contralateral sides of the cord. Additionally, the presence of pTDP-43 pathology in the giant cells of Betz in the primary motor cortex confirmed the ability of a local TDP-43 overexpression event to induce the widespread propagation of pTDP-43 pathology. The pTDP-43 pathology was present throughout the mediolateral extent of both motor hemispheres, indicating that spread had not only reached the CM cells which monosynaptically connect to the transfected right brachioradialis motoneurons, but had spread throughout the cortex. Whether this spread took place primarily from other transfected spinal MNs backwards to the motor cortex, or if pathology spread in multiple directions is yet to be elucidated. A complete lack of this proteinopathy in the healthy age-matched control macaque confirmed that the formation of these proteinopathies in the spinal cord and M1 neurons was directly linked to spreading outwards from the transfected motoneurons.

As mentioned, one potential cause for changes in mean EMG in muscles throughout the upper limbs could be the spread of TDP-43 pathology from the virus transfected cells innervating the R-BR. However, an alternative explanation for the limb-wide EMG changes could be the spreading of virus into adjacent muscles, thus targeting other spinal motor pools, or trans-synaptic spread from the transfected MNs. The latter can be ruled out immediately, as AAVs are replication-defective without the addition of a helper virus, such as an adenovirus (AV), and so cannot spread trans-synaptically (Atchison et al., 1965). The former was controlled for during the intramuscular administration, as low volumes (100µl) were injected slowly at multiple sites close to the motor end plates. Identification of the end plate zone using electrical stimulation through the needle (see General Methods)

provided confirmation that only the R-BR was injected. Of course, there may have been some spread of virus via leakage out of the injection sites, although most of this would have been controlled for by the small aliquots and their slow injection. Spread to adjacent muscles would be unlikely to account for the ultimate EMG changes recorded in the more proximal muscles such as the biceps and brachialis, or in the contralateral limb in the case of Monkey Ma.

Additionally, there is a possibility of the virus spreading through the blood stream, and this has in fact been reported in neonatal mice with the result of widespread transduction throughout the CNS (Chen et al., 2020). This has not been reported in primates, however, where intramuscular delivery results in only select retrograde transduction of the motoneurons which supply that muscle (Towne et al., 2010, Bohlen et al., 2019).

A complete lack of fluorescent viral tag in the spinal segments which innervate the brachioradialis muscle, in combination with a reduction of motoneurons in the right side of the cord in these segments implies that the initially transfected cells have succumbed to the TDP-43 overexpression and degenerated. The fluorescent tdTomato tag was also not identified in any other cervical spinal segment, the first thoracic segment or in the motor cortex. This absence confirms that the intramuscular rAAV2 virus did not spread trans-synaptically from the transfected right brachioradialis motoneurons, and was also not spread around the CNS by the blood stream. The pTDP-43 proteinopathies were therefore not caused by widespread transduction of human TDP-43, but rather propagated in a ‘prion-like’ manner from the selectively transfected motor pool.

### **Time course of severity**

Characteristic sequences of changes were detected in both animals, indicating a comparable mechanism of pathology. Many factors, for example the location of virus injections within the muscle, weight of the animal and upper limb posture during task performance and nerve stimulation, may contribute to variability in the outcome in each experimental animal. Some expected inter-subject variability was recorded, however, the patterns of in vivo and post mortem change were remarkably conserved. Limb-wide phasic changes of intramuscular EMG activity and CMAP amplitude were recorded from as early as six weeks after the virus injections, in multiple upper limb muscles. During the first half of the project, before the electrophysiological trends conserved between animals and limbs became clear, the period of MRI signal hyperintensity occurred. It could be argued that the

elevated signal represented a standard pathophysiological process in the muscle, as the signal changes progressed in the same spatial pattern throughout the muscle and for the same number of weeks in both animals. The changes in task-related EMG and CMAP do not necessarily line up, however they both appear in phases emphasising the role of compensatory reinnervation in this pathological process.

The histological changes, on the other hand, paint a picture of widespread, ubiquitous pathology, reaching as far as the neurons of the motor cortex. The increasingly phasic electrophysiological changes recorded throughout the experimental and control limbs may be representative of the pre-symptomatic phase of MND in which compensatory remodelling of motor units disguises the severity of the neuronal injury and onset of the disease. It is possible that the time point at which we terminated the experiment occurred immediately before the ‘tipping point’ when other motoneurons and CM cells began to degenerate, reinnervation could no longer keep up and symptoms began to manifest. However, it is unknown for how long malfunctioning cells can survive while overloaded with pathological aggregates.

Despite the phenotypic heterogeneity in MND, patients tend to display similar median survival times. This is especially so in patients with comparable sites of disease onset. It therefore seems plausible that there is a chain reaction that may start and progress using variable mechanisms and pathways, but that culminates in a similar end point after a reasonably set period of time. This feature of MND could be said to be replicated in our model; the two animals demonstrated different onset times, registered by the hyperintense MRI signals, but ultimately followed very similar disease trajectories, with altered patterns of muscle activity occurring at the same time.

In our model animals, spinal cord MNs in segments closest, and contralateral to the transfected motor pool, as well as the directly connected CM cells showed greater levels of pathology than the more distant or indirectly connected cells. The initial site of overexpression of TDP-43 in the right brachioradialis MNs therefore likely played a critical role in directing the pattern of spread of pTDP-43 seen in the transfected animals. The findings from this model suggest that TDP-43 proteinopathies are able to propagate outwards in a somewhat orderly fashion from spinal MNs, consistent with Ravits and La Spada (2009)’s hypothesis regarding orderly spread. We would therefore posit that if an alternative motor pool was induced to overexpress TDP-43, a similar pattern would be seen,

but with the focal point and secondarily affected cells shifted accordingly. Had the overexpression of TDP-43 been limited to the UMNs, including the Betz cells of M1, rather than the spinal cord MNs, the pTDP-43 would likely propagate 'forwards' down the CST to the monosynaptically connected MNs, and possibly contiguously throughout M1, at which point the widespread propagation may begin.

### **Future Directions**

To elucidate the timeline of disease progression and to determine the severity of disease caused by this TDP-43 overexpression event, it would be useful to assess the presence of pathological inclusions in other cortical regions, following the staging criteria set out by Brettschneider et al. (2013). We have determined that the animals displayed pathology comparable to that of stage one MND pathology, with pTDP-43 proteinopathies present in the spinal  $\alpha$ -MNs and CM cells of M1, although analysis of the brainstem cranial motor nuclei is required to assess if spread has reached these cell populations. It would be of interest to track the limits of the pathological spread, to see if the proteinopathies followed the categorised stages, with inclusions noted in patients within cortical and subcortical areas such as the reticular formation, red nucleus, prefrontal cortex and ultimately, in the latest stage of disease, in temporal regions such as the hippocampus. It is also important to rule out the presence of pTDP-43 proteinopathies in the oculomotor motoneurons, a cranial nucleus generally unaffected in MND patients, in order to confirm the validity and representativeness of this pathological spread in modelling MND (Lawyer and Netsky, 1953).

It would be very interesting to determine whether pTDP-43 pathology is also present in the frontotemporal lobes in our model, as is the case in FTL. Such a discovery might provide further insight into the relationship between these two disorders, thought to exist on either end of a spectrum. If this pathology were to be found in this model, in future, a cognitive test could be developed in order to assess any signs of impairment to aid with staging of this disease.

MND is phenotypically variable, and it is likely that numerous factors are involved in the dysregulation of TDP-43 and that multiple mechanisms of spread work in tandem or independently to propagate the proteinopathies between cell populations in disease. This model of TDP-43 proteinopathy has created a starting point at which we are able to test the possible mechanisms and routes of spread utilised in this disease and dissect the function

and role of TDP-43. While we cannot confirm whether pathology spreads in this way naturally in disease, we have displayed what an overexpression of wild type human TDP-43 in a focal motor pool could lead to in a human-like system.

It would be of great interest to harness this dual virus technology to transfect a small population of CM cells in order to record the pattern of pathological pTDP-43 propagation when overexpression is initiated at the site of the UMNs, rather than the LMNs. Differences in the time course of disease, pattern of spread between cells and ultimately symptom severity between different sites of onset in this model would be invaluable for understanding phenotypic diversity, as well as deciphering and targeting the mechanisms at play in this complex disease.

There are many potential benefits and applications of a model of this kind. The similarity of the motor system and genetic profile of macaques and humans make them an ideal animal for the study of this complex disease, and an assumption can be made that any disease mechanisms occurring in the model will be similar to that which could occur in humans. It is of course impossible to recapitulate the disease processes which occur in MND with our current understanding, however replicating the pathological outcomes of such diseases in a system near identical to humans allows us to identify novel drug targets and gain a better understanding of the disease mechanisms. This model of pTDP-43 pathology, with evidence of prion-like spread, is an ideal candidate for pre-clinical therapeutic trials with the potential for high translatability into human studies.

## References

- ALONSO, A., LOGROSCINO, G., JICK, S. S. & HERNAN, M. A. 2009. Incidence and lifetime risk of motor neuron disease in the United Kingdom: a population-based study. *Eur J Neurol*, 16, 745-51.
- ALSTERMARK, B. & OGAWA, J. 2004. In vivo recordings of bulbospinal excitation in adult mouse forelimb motoneurons. *J Neurophysiol*, 92, 1958-62.
- ARAI, T., HASEGAWA, M., AKIYAMA, H., IKEDA, K., NONAKA, T., MORI, H., MANN, D., TSUCHIYA, K., YOSHIDA, M., HASHIZUME, Y. & ODA, T. 2006. TDP-43 is a component of ubiquitin-positive tau-negative inclusions in frontotemporal lobar degeneration and amyotrophic lateral sclerosis. *Biochem Biophys Res Commun*, 351, 602-11.
- ARGYRIOU, A. A., POLYCHRONOPOULOS, P., TALELLI, P. & CHRONI, E. 2006. F wave study in amyotrophic lateral sclerosis: Assessment of balance between upper and lower motor neuron involvement. *Clinical Neurophysiology*, 117, 1260-1265.
- ARRUDA, V. R., SCHUETTRUMPF, J., HERZOG, R. W., NICHOLS, T. C., ROBINSON, N., LOTFI, Y., MINGOZZI, F., XIAO, W. D., COUTO, L. B. & HIGH, K. A. 2004. Safety and efficacy of factor IX gene transfer to skeletal muscle in murine and canine hemophilia B models by adeno-associated viral vector serotype 1. *Blood*, 103, 85-92.
- ATCHISON, R. W., CASTO, B. C. & HAMMON, W. M. 1965. Adenovirus-Associated Defective Virus Particles. *Science*, 149, 754-6.
- BAKER, M. R. 2014. ALS-dying forward, backward or outward? *Nature Reviews Neurology*, 10.
- BAKKEN, T. E., JORSTAD, N. L., HU, Q. W., LAKE, B. B., TIAN, W., KALMBACH, B. E., CROW, M., HODGE, R. D., KRIENEN, F. M., SORENSEN, S. A., EGGERMONT, J., YAO, Z. Z., AEVERMANN, B. D., ALDRIDGE, A. I., BARTLETT, A., BERTAGNOLLI, D., CASPER, T., CASTANON, R. G., CRICHTON, K., DAIGLE, T. L., DALLEY, R., DEE, N., DEMBROW, N., DIEP, D., DING, S. L., DONG, W. X., FANG, R. X., FISCHER, S., GOLDMAN, M., GOLDY, J., GRAYBUCK, L. T., HERB, B. R., HOU, X. M., KANCHERLA, J., KROLL, M., LATHIA, K., VAN LEW, B., LI, Y. E., LIU, C. E. S., LIU, H. Q., LUCERO, J. D., MAHURKAR, A., MCMILLEN, D., MILLER, J. A., MOUSSA, M., NERY, J. R., NICOVICH, P. R., NIU, S. Y., ORVIS, J., OSTEN, J. K., OWEN, S., PALMER, C. R., PHAM, T., PLONGTHONGKUM, N., POIRION, O., REED, N. M., RIMORIN, C., RIVKIN, A., ROMANOW, W. J., SEDENO-CORTES, A. E., SILETTI, K., SOMASUNDARAM, S., SULC, J., TIEU, M., TORKELESON, A., TUNG, H. R., WANG, X. N., XIE, F. M., YANNY, A. M., ZHANG, R. E., AMENT, S. A., BEHRENS, M. M., BRAVO, H. C., CHUN, J., DOBIN, A., GILLIS, J., HERTZANO, R., HOF, P. R., HOLLT, T., HORWITZ, G. D., KEENE, C. D., KHARCHENKO, P. V., KO, A. L., LELIEVELDT, B. P., LUO, C. Y., MUKAMEL, E. A., PINTO-DUARTE, A., PREISSEL, S., REGEV, A., REN, B., SCHEUERMANN, R. H., SMITH, K., SPAIN, W. J., WHITE, O. R., KOCH, C., HAWRYLYCZ, M., TASIC, B., MACOSKO, E. Z., MCCARROLL, S. A., TING, J. T., et al. 2021. Comparative cellular analysis of motor cortex in human, marmoset and mouse. *Nature*, 598, 111-+.
- BANNATYNE, B. A., LIU, T. T., HAMMAR, I., STECINA, K., JANKOWSKA, E. & MAXWELL, D. J. 2009. Excitatory and inhibitory intermediate zone interneurons in pathways

- from feline group I and II afferents: differences in axonal projections and input. *J Physiol*, 587, 379-99.
- BARBER, R. P., PHELPS, P. E., HOUSER, C. R., CRAWFORD, G. D., SALVATERRA, P. M. & VAUGHN, J. E. 1984. The morphology and distribution of neurons containing choline acetyltransferase in the adult rat spinal cord: an immunocytochemical study. *J Comp Neurol*, 229, 329-46.
- BARKER, D., EMONET-DENAND, F., HARKER, D. W., JAMI, L. & LAPORTE, Y. 1977. Types of intra- and extrafusal muscle fibre innervated by dynamic skeleto-fusimotor axons in cat peroneus brevis and tenuissimus muscles, as determined by the glycogen-depletion method. *J Physiol*, 266, 713-26.
- BARTHELEMY, D., GREY, M. J., NIELSEN, J. B. & BOUYER, L. 2011. Involvement of the corticospinal tract in the control of human gait. *Enhancing Performance for Action and Perception: Multisensory Integration, Neuroplasticity and Neuroprosthetics, Pt II*, 192, 181-197.
- BENATAR, M., BOYLAN, K., JEROMIN, A., RUTKOVE, S. B., BERRY, J., ATASSI, N. & BRUIJN, L. 2016. Als Biomarkers for Therapy Development: State of the Field and Future Directions. *Muscle & Nerve*, 53, 169-182.
- BENDSZUS, M., KOLTZENBURG, M., WESSIG, C. & SOLYMOSI, L. 2002. Sequential MR imaging of denervated muscle: experimental study. *AJNR Am J Neuroradiol*, 23, 1427-31.
- BENDSZUS, M., WESSIG, C., SOLYMOSI, L., REINERS, K. & KOLTZENBURG, M. 2004. MRI of peripheral nerve degeneration and regeneration: correlation with electrophysiology and histology. *Exp Neurol*, 188, 171-7.
- BENJAMINI, Y. & HOCHBERG, Y. 1995. Controlling the False Discovery Rate - a Practical and Powerful Approach to Multiple Testing. *Journal of the Royal Statistical Society Series B-Statistical Methodology*, 57, 289-300.
- BENSIMON, G., LACOMBLEZ, L. & MEININGER, V. 1994. A controlled trial of riluzole in amyotrophic lateral sclerosis. ALS/Riluzole Study Group. *N Engl J Med*, 330, 585-91.
- BERNHARD, C. G. & BOHM, E. 1954. Cortical representation and functional significance of the corticomotoneuronal system. *AMA Arch Neurol Psychiatry*, 72, 473-502.
- BESSOU, P., EMONET-DENAND, F. & LAPORTE, Y. 1965. Motor fibres innervating extrafusal and intrafusal muscle fibres in the cat. *J Physiol*, 180, 649-72.
- BEVAN, A. K., DUQUE, S., FOUST, K. D., MORALES, P. R., BRAUN, L., SCHMELZER, L., CHAN, C. M., MCCRATE, M., CHICOINE, L. G., COLEY, B. D., PORENSKY, P. N., KOLB, S. J., MENDELL, J. R., BURGHESE, A. H. & KASPAR, B. K. 2011. Systemic gene delivery in large species for targeting spinal cord, brain, and peripheral tissues for pediatric disorders. *Mol Ther*, 19, 1971-80.
- BEY, K., DENIAUD, J., DUBREIL, L., JOUSSEMET, B., CRISTINI, J., CIRON, C., HORDEAUX, J., LE BOULC'H, M., MARCHE, K., MAQUIGNEAU, M., GUILBAUD, M., MOREAU, R., LARCHER, T., DESCHAMPS, J. Y., FUSELLIER, M., BLOUIN, V., SEVIN, C., CARTIER, N., ADJALI, O., AUBOURG, P., MOULLIER, P. & COLLE, M. A. 2020. Intra-CSF AAV9 and AAVrh10 Administration in Nonhuman Primates: Promising Routes and Vectors for Which Neurological Diseases? *Molecular Therapy-Methods & Clinical Development*, 17, 771-784.
- BI, G. & POO, M. 2001. Synaptic modification by correlated activity: Hebb's postulate revisited. *Annu Rev Neurosci*, 24, 139-66.

- BOE, S. G., STASHUK, D. W., BROWN, W. F. & DOHERTY, T. J. 2005. Decomposition-based quantitative electromyography: Effect of force on motor unit potentials and motor unit number estimates. *Muscle & Nerve*, 31, 365-373.
- BOE, S. G., STASHUK, D. W. & DOHERTY, T. J. 2006. Within-subject reliability of motor unit number estimates and quantitative motor unit analysis in a distal and proximal upper limb muscle. *Clinical Neurophysiology*, 117, 596-603.
- BOEKESTEIN, W. A., SCHELHAAS, H. J., VAN PUTTEN, M. J., STEGEMAN, D. F., ZWARTS, M. J. & VAN DIJK, J. P. 2012. Motor unit number index (MUNIX) versus motor unit number estimation (MUNE): a direct comparison in a longitudinal study of ALS patients. *Clin Neurophysiol*, 123, 1644-9.
- BOHLEN, M. O., EL-NAHAL, H. G. & SOMMER, M. A. 2019. Transduction of Craniofacial Motoneurons Following Intramuscular Injections of Canine Adenovirus Type-2 (CAV-2) in Rhesus Macaques. *Frontiers in Neuroanatomy*, 13.
- BOLAND, M. R., SPIGELMAN, T. & UHL, T. L. 2008. The Function of Brachioradialis. *Journal of Hand Surgery-American Volume*, 33a, 1853-1859.
- BRAAK, H., BRETTSCHEIDER, J., LUDOLPH, A. C., LEE, V. M., TROJANOWSKI, J. Q. & DEL TREDICI, K. 2013. Amyotrophic lateral sclerosis-a model of corticofugal axonal spread. *Nature Reviews Neurology*, 9, 708-714.
- BRAAK, H., LUDOLPH, A. C., NEUMANN, M., RAVITS, J. & DEL TREDICI, K. 2017. Pathological TDP-43 changes in Betz cells differ from those in bulbar and spinal alpha-motoneurons in sporadic amyotrophic lateral sclerosis. *Acta Neuropathol*, 133, 79-90.
- BREDELLA, M. A., TIRMAN, P. F. J., FRITZ, R. C., WISCHER, T. K., STORK, A. & GENANT, H. K. 1999. Denervation syndromes of the shoulder girdle: MR imaging with electrophysiologic correlation. *Skeletal Radiology*, 28, 567-572.
- BRETTSCHEIDER, J., ARAI, K., DEL TREDICI, K., TOLEDO, J. B., ROBINSON, J. L., LEE, E. B., KUWABARA, S., SHIBUYA, K., IRWIN, D. J., FANG, L., VAN DEERLIN, V. M., ELMAN, L., MCCLUSKEY, L., LUDOLPH, A. C., LEE, V. M., BRAAK, H. & TROJANOWSKI, J. Q. 2014. TDP-43 pathology and neuronal loss in amyotrophic lateral sclerosis spinal cord. *Acta Neuropathol*, 128, 423-37.
- BRETTSCHEIDER, J., DEL TREDICI, K., TOLEDO, J. B., ROBINSON, J. L., IRWIN, D. J., GROSSMAN, M., SUH, E., VAN DEERLIN, V. M., WOOD, E. M., BAEK, Y., KWONG, L., LEE, E. B., ELMAN, L., MCCLUSKEY, L., FANG, L. B., FELDENGUT, S., LUDOLPH, A. C., LEE, V. M. Y., BRAAK, H. & TROJANOWSKI, J. Q. 2013. Stages of pTDP-43 Pathology in Amyotrophic Lateral Sclerosis. *Annals of Neurology*, 74, 20-38.
- BROMBERG, M. B., FORSHEW, D. A., NAU, K. L., BROMBERG, J., SIMMONS, Z. & FRIES, T. J. 1993. Motor Unit Number Estimation, Isometric Strength, and Electromyographic Measures in Amyotrophic-Lateral-Sclerosis. *Muscle & Nerve*, 16, 1213-1219.
- BROOKS, B. R., MILLER, R. G., SWASH, M., MUNSAT, T. L. & GR, W. F. N. R. 2000. El Escorial revisited: Revised criteria for the diagnosis of amyotrophic lateral sclerosis. *Amyotrophic Lateral Sclerosis and Other Motor Neuron Disorders*, 1, 293-299.
- BROUWER, B. & ASHBY, P. 1990. Corticospinal Projections to Upper and Lower-Limb Spinal Motoneurons in Man. *Electroencephalography and Clinical Neurophysiology*, 76, 509-519.

- BURATTI, E. & BARALLE, F. E. 2008. Multiple roles of TDP-43 in gene expression, splicing regulation, and human disease. *Frontiers in Bioscience-Landmark*, 13, 867-878.
- BUTT, S. J. & KIEHN, O. 2003. Functional identification of interneurons responsible for left-right coordination of hindlimbs in mammals. *Neuron*, 38, 953-63.
- CAIRNS, N. J., NEUMANN, M., BIGIO, E. H., HOLM, I. E., TROOST, D., HATANPAA, K. J., FOONG, C., WHITE, C. L., 3RD, SCHNEIDER, J. A., KRETZSCHMAR, H. A., CARTER, D., TAYLOR-REINWALD, L., PAULSMEYER, K., STRIDER, J., GITCHO, M., GOATE, A. M., MORRIS, J. C., MISHRA, M., KWONG, L. K., STIEBER, A., XU, Y., FORMAN, M. S., TROJANOWSKI, J. Q., LEE, V. M. & MACKENZIE, I. R. 2007. TDP-43 in familial and sporadic frontotemporal lobar degeneration with ubiquitin inclusions. *Am J Pathol*, 171, 227-40.
- CATSMAN-BERREVOETS, C. E. & KUYPERS, H. G. 1976. Cells of origin of cortical projections to dorsal column nuclei, spinal cord and bulbar medial reticular formation in the rhesus monkey. *Neurosci Lett*, 3, 245-52.
- CHEAH, B. C., VUCIC, S., KRISHNAN, A. V. & KIERNAN, M. C. 2010. Riluzole, Neuroprotection and Amyotrophic Lateral Sclerosis. *Current Medicinal Chemistry*, 17, 1942-1959.
- CHEN, Z., FAN, G., LI, A., YUAN, J. & XU, T. 2020. rAAV2-Retro Enables Extensive and High-Efficient Transduction of Lower Motor Neurons following Intramuscular Injection. *Mol Ther Methods Clin Dev*, 17, 21-33.
- CHIRMULE, N., XIAO, W. D., TRUNEH, A., SCHNELL, M. A., HUGHES, J. V., ZOLTICK, P. & WILSON, J. M. 2000. Humoral immunity to adeno-associated virus type 2 vectors following administration to murine and nonhuman primate muscle. *Journal of Virology*, 74, 2420-2425.
- CHRISTENSEN, E. 1959. Topography of terminal motor innervation in striated muscles from stillborn infants. *Am J Phys Med*, 38, 65-78.
- CICCARELLI, O., BEHRENS, T. E., ALTMANN, D. R., ORRELL, R. W., HOWARD, R. S., JOHANSEN-BERG, H., MILLER, D. H., MATTHEWS, P. M. & THOMPSON, A. J. 2006. Probabilistic diffusion tractography: a potential tool to assess the rate of disease progression in amyotrophic lateral sclerosis. *Brain*, 129, 1859-1871.
- CIFRA, A., NANI, F. & NISTRÌ, A. 2011. Riluzole is a potent drug to protect neonatal rat hypoglossal motoneurons in vitro from excitotoxicity due to glutamate uptake block. *European Journal of Neuroscience*, 33, 899-913.
- COLON, A., GUO, X., AKANDA, N., CAI, Y. & HICKMAN, J. J. 2017. Functional analysis of human intrafusal fiber innervation by human gamma-motoneurons. *Scientific Reports*, 7.
- CUSHMAN, M., JOHNSON, B. S., KING, O. D., GITLER, A. D. & SHORTER, J. 2010. Prion-like disorders: blurring the divide between transmissibility and infectivity. *Journal of Cell Science*, 123, 1191-1201.
- DAY, S. J. & HULLIGER, M. 2001. Experimental simulation of cat electromyogram: Evidence for algebraic summation of motor-unit action-potential trains. *Journal of Neurophysiology*, 86, 2144-2158.
- DE CARVALHO, M., BARKHAUS, P. E., NANDEDKAR, S. D. & SWASH, M. 2018. Motor unit number estimation (MUNE): Where are we now? *Clin Neurophysiol*, 129, 1507-1516.
- DE CARVALHO, M., DENGLER, R., EISEN, A., ENGLAND, J. D., KAJI, R., KIMURA, J., MILLS, K., MITSUMOTO, H., NODERA, H., SHEFNER, J. & SWASH, M. 2008.

- Electrodiagnostic criteria for diagnosis of ALS. *Clinical Neurophysiology*, 119, 497-503.
- DE NOORDHOUT, A. M., RAPISARDA, G., BOGACZ, D., GERARD, P., DE PASQUA, V., PENNISI, G. & DELWAIDE, P. J. 1999. Corticomotoneuronal synaptic connections in normal man - An electrophysiological study. *Brain*, 122, 1327-1340.
- DEFOREST, B. A., WINSLOW, J. & THOMAS, C. K. 2018. Improved motor unit number estimate when motor unit alternation is addressed. *Journal of Applied Physiology*, 125, 1131-1140.
- DEJESUS-HERNANDEZ, M., MACKENZIE, I. R., BOEVE, B. F., BOXER, A. L., BAKER, M., RUTHERFORD, N. J., NICHOLSON, A. M., FINCH, N. A., FLYNN, H., ADAMSON, J., KOURI, N., WOJTAS, A., SENGDY, P., HSIUNG, G. Y. R., KARYDAS, A., SEELEY, W. W., JOSEPHS, K. A., COPPOLA, G., GESCHWIND, D. H., WSZOLEK, Z. K., FELDMAN, H., KNOPMAN, D. S., PETERSEN, R. C., MILLER, B. L., DICKSON, D. W., BOYLAN, K. B., GRAFF-RADFORD, N. R. & RADEMAKERS, R. 2011. Expanded GGGGCC Hexanucleotide Repeat in Noncoding Region of C9ORF72 Causes Chromosome 9p-Linked FTD and ALS. *Neuron*, 72, 245-256.
- DEL VECCHIO, A., JONES, R. H. A., SCHOFIELD, I. S., KINFE, T. M., IBANEZ, J., FARINA, D. & BAKER, S. N. 2022. Interfacing Motor Units in Non-Human Primates Identifies a Principal Neural Component for Force Control Constrained by the Size Principle. *J Neurosci*.
- DENG, H. X., SHI, Y., FURUKAWA, Y., ZHAI, H., FU, R. G., LIU, E. D., GORRIE, G. H., KHAN, M. S., HUNG, W. Y., BIGIO, E. H., LUKAS, T., DAL CANTO, M. C., O'HALLORAN, T. V. & SIDDIQUE, T. 2006. Conversion to the amyotrophic lateral sclerosis phenotype is associated with intermolecular linked insoluble aggregates of SOD1 in mitochondria. *Proceedings of the National Academy of Sciences of the United States of America*, 103, 7142-7147.
- DIDERIKSEN, J. L. & FARINA, D. 2019. Amplitude cancellation influences the association between frequency components in the neural drive to muscle and the rectified EMG signal. *Plos Computational Biology*, 15.
- DUM, R. P. & STRICK, P. L. 1996. Spinal cord terminations of the medial wall motor areas in macaque monkeys. *Journal of Neuroscience*, 16, 6513-6525.
- DUQUE, S., JOUSSEMET, B., RIVIERE, C., MARAIS, T., DUBREIL, L., DOUAR, A. M., FYFE, J., MOULLIER, P., COLLE, M. A. & BARKATS, M. 2009. Intravenous administration of self-complementary AAV9 enables transgene delivery to adult motor neurons. *Mol Ther*, 17, 1187-96.
- EISEN, A., BRAAK, H., DEL TREDICI, K., LEMON, R., LUDOLPH, A. C. & KIERNAN, M. C. 2017. Cortical influences drive amyotrophic lateral sclerosis. *Journal of Neurology Neurosurgery and Psychiatry*, 88, 917-924.
- EISEN, A. & WEBER, M. 2001. The motor cortex and amyotrophic lateral sclerosis. *Muscle Nerve*, 24, 564-73.
- ESCORCIO-BEZERRA, M. L., ABRAHAO, A., SANTOS-NETO, D., BRAGA, N. I. D., OLIVEIRA, A. S. B. & MANZANO, G. M. 2017. Why averaging multiple MUNIX measures in the longitudinal assessment of patients with ALS? *Clinical Neurophysiology*, 128, 2392-2396.
- FALLINI, C., BASSELL, G. J. & ROSSOLL, W. 2012. The ALS disease protein TDP-43 is actively transported in motor neuron axons and regulates axon outgrowth. *Hum Mol Genet*, 21, 3703-18.

- FANG, J., LIU, M. S., GUAN, Y. Z., DU, H., LI, B. H., CUI, B., DING, Q. Y. & CUI, L. Y. 2016. Pattern Differences of Small Hand Muscle Atrophy in Amyotrophic Lateral Sclerosis and Mimic Disorders. *Chin Med J (Engl)*, 129, 792-8.
- FANG, T., AL KHLEIFAT, A., MEURGEY, J. H., JONES, A., LEIGH, P. N., BENSIMON, G. & AL-CHALABI, A. 2018. Stage at which riluzole treatment prolongs survival in patients with amyotrophic lateral sclerosis: a retrospective analysis of data from a dose-ranging study. *Lancet Neurol*, 17, 416-422.
- FEILER, M. S., STROBEL, B., FREISCHMIDT, A., HELFERICH, A. M., KAPPEL, J., BREWER, B. M., LI, D., THAL, D. R., WALTHER, P., LUDOLPH, A. C., DANZER, K. M. & WEISHAUPT, J. H. 2015. TDP-43 is intercellularly transmitted across axon terminals. *Journal of Cell Biology*, 211, 897-911.
- FELICE, K. J. 1997. A longitudinal study comparing thenar motor unit number estimates to other quantitative tests in patients with amyotrophic lateral sclerosis. *Muscle & Nerve*, 20, 179-185.
- FERRARO, P. M., AGOSTA, F., RIVA, N., COPETTI, M., SPINELLI, E. G., FALZONE, Y., SORARU, G., COMI, G., CHIO, A. & FILIPPI, M. 2017. Multimodal structural MRI in the diagnosis of motor neuron diseases. *Neuroimage Clin*, 16, 240-247.
- FETZ, E. E. & CHENEY, P. D. 1980. Postspike facilitation of forelimb muscle activity by primate corticomotoneuronal cells. *J Neurophysiol*, 44, 751-72.
- FISCHBEIN, N. J., KAPLAN, M. J., JACKLER, R. K. & DILLON, W. P. 2001. MR imaging in two cases of subacute denervation change in the muscles of facial expression. *American Journal of Neuroradiology*, 22, 880-884.
- FISCHER, L. R., CULVER, D. G., TENNANT, P., DAVIS, A. A., WANG, M. S., CASTELLANO-SANCHEZ, A., KHAN, J., POLAK, M. A. & GLASS, J. D. 2004. Amyotrophic lateral sclerosis is a distal axonopathy: evidence in mice and man. *Experimental Neurology*, 185, 232-240.
- FISHER, K. M., ZAAIMI, B., WILLIAMS, T. L., BAKER, S. N. & BAKER, M. R. 2012. Beta-band intermuscular coherence: a novel biomarker of upper motor neuron dysfunction in motor neuron disease. *Brain*, 135, 2849-2864.
- FREY, D., SCHNEIDER, C., XU, L., BORG, J., SPOOREN, W. & CARONI, P. 2000. Early and selective loss of neuromuscular synapse subtypes with low sprouting competence in motoneuron diseases. *J Neurosci*, 20, 2534-42.
- GAO, J., WANG, L., HUNTLEY, M. L., PERRY, G. & WANG, X. 2018. Pathomechanisms of TDP-43 in neurodegeneration. *J Neurochem*.
- GEEVASINGA, N., MENON, P., OZDINLER, P. H., KIERNAN, M. C. & VUCIC, S. 2016. Pathophysiological and diagnostic implications of cortical dysfunction in ALS. *Nature Reviews Neurology*, 12, 651-661.
- GENC, B., JARA, J. H., LAGRIMAS, A. K. B., PYTEL, P., ROOS, R. P., MESULAM, M. M., GEULA, C., BIGIO, E. H. & OZDINLER, P. H. 2017. Apical dendrite degeneration, a novel cellular pathology for Betz cells in ALS. *Scientific Reports*, 7.
- GEYER, S., LEDBERG, A., SCHLEICHER, A., KINOMURA, S., SCHORMANN, T., BURGEL, U., KLINGBERG, T., LARSSON, J., ZILLES, K. & ROLAND, P. E. 1996. Two different areas within the primary motor cortex of man. *Nature*, 382, 805-807.
- GOOCH, C. L., DOHERTY, T. J., CHAN, K. M., BROMBERG, M. B., LEWIS, R. A., STASHUK, D. W., BERGER, M. J., ANDARY, M. T. & DAUBE, J. R. 2014. Motor Unit Number Estimation: A Technology and Literature Review. *Muscle & Nerve*, 50, 884-893.

- GRAY, S. J., NAGABHUSHAN KALBURGI, S., MCCOWN, T. J. & JUDE SAMULSKI, R. 2013. Global CNS gene delivery and evasion of anti-AAV-neutralizing antibodies by intrathecal AAV administration in non-human primates. *Gene Ther*, 20, 450-9.
- GREENMAN, R. L., KHAODHIAR, L., LIMA, C., DINH, T., GIURINI, J. M. & VEVES, A. 2005. Foot small muscle atrophy is present before the detection of clinical neuropathy. *Diabetes Care*, 28, 1425-1430.
- GREIG, J. A., PENG, H., OHLSTEIN, J., MEDINA-JASZEK, C. A., AHONKHAI, O., MENTZINGER, A., GRANT, R. L., ROY, S., CHEN, S. J., BELL, P., TRETIAKOVA, A. P. & WILSON, J. M. 2014. Intramuscular injection of AAV8 in mice and macaques is associated with substantial hepatic targeting and transgene expression. *PLoS One*, 9, e112268.
- GU, Z., KALAMBOGIAS, J., YOSHIOKA, S., HAN, W., LI, Z., KAWASAWA, Y. I., POCHAREDDY, S., LI, Z., LIU, F., XU, X., WIJERATNE, H. R. S., UENO, M., BLATZ, E., SALOMONE, J., KUMANOGOH, A., RASIN, M. R., GEBELEIN, B., WEIRAUCH, M. T., SESTAN, N., MARTIN, J. H. & YOSHIDA, Y. 2017. Control of species-dependent cortico-motoneuronal connections underlying manual dexterity. *Science*, 357, 400-404.
- GUNES, T., SIRIN, N. G., SAHIN, S., KOSE, E. & ISAK, B. 2021. Use of CMAP, MScan fit-MUNE, and MUNIX in understanding neurodegeneration pattern of ALS and detection of early motor neuron loss in daily practice. *Neuroscience Letters*, 741.
- GUSEL'NIKOVA, V. V. & KORZHEVSKIY, D. E. 2015. NeuN As a Neuronal Nuclear Antigen and Neuron Differentiation Marker. *Acta Naturae*, 7, 42-47.
- HANSEN, S. & BALLANTYNE, J. P. 1978. A quantitative electrophysiological study of motor neurone disease. *J Neurol Neurosurg Psychiatry*, 41, 773-83.
- HEFFNER, R. & MASTERTON, B. 1975. Variation in form of the pyramidal tract and its relationship to digital dexterity. *Brain Behav Evol*, 12, 161-200.
- HEGEDUS, J., PUTMAN, C. T. & GORDON, T. 2007. Time course of preferential motor unit loss in the SODIG93A mouse model of amyotrophic lateral sclerosis. *Neurobiology of Disease*, 28, 154-164.
- HENNEMAN, E. 1957. Relation between size of neurons and their susceptibility to discharge. *Science*, 126, 1345-7.
- HORN, A. K. & LEIGH, R. J. 2011. The anatomy and physiology of the ocular motor system. *Handb Clin Neurol*, 102, 21-69.
- HOSSAINI, M., CARDONA CANO, S., VAN DIS, V., HAASDIJK, E. D., HOOGENRAAD, C. C., HOLSTEGE, J. C. & JAARSMA, D. 2011. Spinal inhibitory interneuron pathology follows motor neuron degeneration independent of glial mutant superoxide dismutase 1 expression in SOD1-ALS mice. *J Neuropathol Exp Neurol*, 70, 662-77.
- HUNT, C. C. & KUFFLER, S. W. 1951. Further study of efferent small-nerve fibers to mammalian muscle spindles; multiple spindle innervation and activity during contraction. *J Physiol*, 113, 283-97.
- ILLERT, M., LUNDBERG, A. & TANAKA, R. 1976. Integration in Descending Motor Pathways Controlling Forelimb in Cat .2. Convergence on Neurons Mediating Disynaptic Cortico-Motoneuronal Excitation. *Experimental Brain Research*, 26, 521-540.
- INUKAI, Y., NONAKA, T., ARAI, T., YOSHIDA, M., HASHIZUME, Y., BEACH, T. G., BURATTI, E., BARALLE, F. E., AKIYAMA, H., HISANAGA, S. & HASEGAWA, M. 2008. Abnormal

- phosphorylation of Ser409/410 of TDP-43 in FTLD-U and ALS. *FEBS Lett*, 582, 2899-904.
- ISA, T., KINOSHITA, M. & NISHIMURA, Y. 2013. Role of direct vs. indirect pathways from the motor cortex to spinal motoneurons in the control of hand dexterity. *Frontiers in Neurology*, 4.
- ISA, T., OHKI, Y., ALSTERMARK, B., PETTERSSON, L. G. & SASAKI, S. 2007. Direct and indirect cortico-motoneuronal pathways and control of Hand/Arm movements. *Physiology*, 22, 145-152.
- IWATSUBO, T., KUZUHARA, S., KANEMITSU, A., SHIMADA, H. & TOYOKURA, Y. 1990. Corticofugal projections to the motor nuclei of the brainstem and spinal cord in humans. *Neurology*, 40, 309-12.
- JACKSON, K. L., DAYTON, R. D., FISHER-PERKINS, J. M., DIDIER, P. J., BAKER, K. C., WEIMER, M., GUTIERREZ, A., CAIN, C. D., MATHIS, J. M., GITCHO, M. A., BUNNELL, B. A. & KLEIN, R. L. 2015. Initial gene vector dosing for studying symptomatology of amyotrophic lateral sclerosis in non-human primates. *J Med Primatol*, 44, 66-75.
- JENKINS, T. M., ALIX, J. J. P., FINGRET, J., ESMAIL, T., HOGGARD, N., BASTER, K., MCDERMOTT, C. J., WILKINSON, I. D. & SHAW, P. J. 2020. Longitudinal multi-modal muscle-based biomarker assessment in motor neuron disease. *Journal of Neurology*, 267, 244-256.
- JENNY, A. B. & INUKAI, J. 1983. Principles of motor organization of the monkey cervical spinal cord. *J Neurosci*, 3, 567-75.
- JOYCE, N. C. & CARTER, G. T. 2013. Electrodiagnosis in persons with amyotrophic lateral sclerosis. *PM R*, 5, S89-95.
- KAMATH, S., VENKATANARASIMHA, N., WALSH, M. A. & HUGHES, P. M. 2008. MRI appearance of muscle denervation. *Skeletal Radiol*, 37, 397-404.
- KANOUCHI, T., OHKUBO, T. & YOKOTA, T. 2012. Can regional spreading of amyotrophic lateral sclerosis motor symptoms be explained by prion-like propagation? *J Neurol Neurosurg Psychiatry*, 83, 739-45.
- KHALAF, R., MARTIN, S., ELLIS, C., BURMAN, R., SREEDHARAN, J., SHAW, C., LEIGH, P. N., TURNER, M. R. & AL-CHALABI, A. 2019. Relative preservation of triceps over biceps strength in upper limb-onset ALS: the 'split elbow'. *Journal of Neurology Neurosurgery and Psychiatry*, 90, 730-733.
- KIERNAN, J. A. & HUDSON, A. J. 1991. Changes in Sizes of Cortical and Lower Motor Neurons in Amyotrophic-Lateral-Sclerosis. *Brain*, 114, 843-853.
- KIM, S. J., HONG, S. H., JUN, W. S., CHOI, J. Y., MYUNG, J. S., JACOBSON, J. A., LEE, J. W., CHOI, J. A. & KANG, H. S. 2011. MR Imaging Mapping of Skeletal Muscle Denervation in Entrapment and Compressive Neuropathies. *Radiographics*, 31, 319-U58.
- KINOSHITA, M., MATSUI, R., KATO, S., HASEGAWA, T., KASAHARA, H., ISA, K., WATAKABE, A., YAMAMORI, T., NISHIMURA, Y., ALSTERMARK, B., WATANABE, D., KOBAYASHI, K. & ISA, T. 2012. Genetic dissection of the circuit for hand dexterity in primates. *Nature*, 487, 235-8.
- KLEIBER, T., KUNZ, L. & DISSELHORST-KLUG, C. 2015. Muscular coordination of biceps brachii and brachioradialis in elbow flexion with respect to hand position. *Frontiers in Physiology*, 6.

- KRAEMER, B. C., SCHUCK, T., WHEELER, J. M., ROBINSON, L. C., TROJANOWSKI, J. Q., LEE, V. M. Y. & SCHELLENBERG, G. D. 2010. Loss of murine TDP-43 disrupts motor function and plays an essential role in embryogenesis. *Acta Neuropathologica*, 119, 409-419.
- KUFFLER, S. W., HUNT, C. C. & QUILLIAM, J. P. 1951. Function of medullated small-nerve fibers in mammalian ventral roots; efferent muscle spindle innervation. *J Neurophysiol*, 14, 29-54.
- KUGLER, S., KILIC, E. & BAHR, M. 2003. Human synapsin 1 gene promoter confers highly neuron-specific long-term transgene expression from an adenoviral vector in the adult rat brain depending on the transduced area. *Gene Therapy*, 10, 337-347.
- KULLMER, K., SIEVERS, K. W., REIMERS, C. D., ROMPE, J. D., MULLER-FELBER, W., NAGELE, M. & HARLAND, U. 1998. Changes of sonographic, magnetic resonance tomographic, electromyographic, and histopathologic findings within a 2-month period of examinations after experimental muscle denervation. *Archives of Orthopaedic and Trauma Surgery*, 117, 228-234.
- KUWABARA, S., SONOO, M., KOMORI, T., SHIMIZU, T., HIRASHIMA, F., INABA, A., MISAWA, S., HATANAKA, Y. & TOKYO METROPOLITAN NEUROMUSCULAR ELECTRODIAGNOSIS STUDY, G. 2008. Dissociated small hand muscle atrophy in amyotrophic lateral sclerosis: frequency, extent, and specificity. *Muscle Nerve*, 37, 426-30.
- KUYPERS, H. G. J. M. 1981. 'Anatomy of the descending pathways.' In: Brooks, V., Ed., *The Nervous System, Handbook of Physiology, Vol 2, Williams and Wilkins, Baltimore*, 597-666.
- KWIATKOWSKI, T. J., BOSCO, D. A., LECLERC, A. L., TAMRAZIAN, E., VANDERBURG, C. R., RUSS, C., DAVIS, A., GILCHRIST, J., KASARSKIS, E. J., MUNSAT, T., VALDMANIS, P., ROULEAU, G. A., HOSLER, B. A., CORTELLI, P., DE JONG, P. J., YOSHINAGA, Y., HAINES, J. L., PERICAK-VANCE, M. A., YAN, J., TICOZZI, N., SIDDIQUE, T., MCKENNA-YASEK, D., SAPP, P. C., HORVITZ, H. R., LANDERS, J. E. & BROWN, R. H. 2009. Mutations in the FUS/TLS Gene on Chromosome 16 Cause Familial Amyotrophic Lateral Sclerosis. *Science*, 323, 1205-1208.
- LALANCETTE-HEBERT, M., SHARMA, A., LYASHCHENKO, A. K. & SHNEIDER, N. A. 2016. Gamma motor neurons survive and exacerbate alpha motor neuron degeneration in ALS. *Proc Natl Acad Sci U S A*, 113, E8316-E8325.
- LATEVA, Z. C., MCGILL, K. C. & JOHANSON, M. E. 2010. The innervation and organization of motor units in a series-fibered human muscle: the brachioradialis. *Journal of Applied Physiology*, 108, 1530-1541.
- LAWYER, T., JR. & NETSKY, M. G. 1953. AMYOTROPHIC LATERAL SCLEROSIS: A Clinicoanatomic Study of Fifty-Three Cases. *A.M.A. Archives of Neurology & Psychiatry*, 69, 171-192.
- LE MASSON, G., PRZEDBORSKI, S. & ABBOTT, L. F. 2014. A computational model of motor neuron degeneration. *Neuron*, 83, 975-88.
- LEMON, R. N. 2008. Descending pathways in motor control. *Annual Review of Neuroscience*, 31, 195-218.
- LI, S. J., VAUGHAN, A., STURGILL, J. F. & KEPECS, A. 2018. A Viral Receptor Complementation Strategy to Overcome CAV-2 Tropism for Efficient Retrograde Targeting of Neurons. *Neuron*, 98, 905-+.

- LIGUORE, W. A., DOMIRE, J. S., BUTTON, D., WANG, Y., DUFOUR, B. D., SRINIVASAN, S. & MCBRIDE, J. L. 2019. AAV-PHP.B Administration Results in a Differential Pattern of CNS Biodistribution in Non-human Primates Compared with Mice. *Molecular Therapy*, 27, 2018-2037.
- LOMEN-HOERTH, C., ANDERSON, T. & MILLER, B. 2002. The overlap of amyotrophic lateral sclerosis and frontotemporal dementia. *Neurology*, 59, 1077-1079.
- LUDOLPH, A. C., EMILIAN, S., DREYHAUPT, J., ROSENBOHM, A., KRASKOV, A., LEMON, R. N., DEL TREDICI, K. & BRAAK, H. 2020. Pattern of paresis in ALS is consistent with the physiology of the corticomotoneuronal projections to different muscle groups. *Journal of Neurology Neurosurgery and Psychiatry*, 91, 991-998.
- MAATHUIS, E. M., DRENTHEIN, J., VAN DIJK, J. P., VISSER, G. H. & BLOK, J. H. 2008. Motor unit tracking with high-density surface EMG. *Journal of Electromyography and Kinesiology*, 18, 920-930.
- MAATHUIS, E. M., DRENTHEIN, J., VAN DOORN, P. A., VISSER, G. H. & BLOK, J. H. 2013. The CMAP scan as a tool to monitor disease progression in ALS and PMA. *Amyotrophic Lateral Sclerosis and Frontotemporal Degeneration*, 14, 217-223.
- MACKENZIE, I. R., BIGIO, E. H., INCE, P. G., GESER, F., NEUMANN, M., CAIRNS, N. J., KWONG, L. K., FORMAN, M. S., RAVITS, J., STEWART, H., EISEN, A., MCCLUSKY, L., KRETZSCHMAR, H. A., MONORANU, C. M., HIGHLEY, J. R., KIRBY, J., SIDDIQUE, T., SHAW, P. J., LEE, V. M. & TROJANOWSKI, J. Q. 2007. Pathological TDP-43 distinguishes sporadic amyotrophic lateral sclerosis from amyotrophic lateral sclerosis with SOD1 mutations. *Ann Neurol*, 61, 427-34.
- MAJOUNIE, E., RENTON, A. E., MOK, K., DOPPER, E. G. P., WAITE, A., ROLLINSON, S., CHIO, A., RESTAGNO, G., NICOLAOU, N., SIMON-SANCHEZ, J., VAN SWIETEN, J. C., ABRAMZON, Y., JOHNSON, J. O., SENDTNER, M., PAMPHLETT, R., ORRELL, R. W., MEAD, S., SIDLE, K. C., HOULDEN, H., ROHRER, J. D., MORRISON, K. E., PALL, H., TALBOT, K., ANSORGE, O., HERNANDEZ, D. G., AREPALLI, S., SABATELLI, M., MORA, G., CORBO, M., GIANNINI, F., CALVO, A., ENGLUND, E., BORGHERO, G., FORIS, G. L., REMES, A. M., LAAKSOVIRTA, H., MCCLUSKEY, L., TROJANOWSKI, J. Q., VAN DEERLIN, V. M., SCHELLENBERG, G. D., NALLS, M. A., DRORY, V. E., LU, C. S., YEH, T. H., ISHIURA, H., TAKAHASHI, Y., TSUJI, S., LE BER, I., BRICE, A., DREPPER, C., WILLIAMS, N., KIRBY, J., SHAW, P., HARDY, J., TIENARI, P. J., HEUTINK, P., MORRIS, H. R., PICKERING-BROWN, S., TRAYNOR, B. J., CONSORTIUM, C.-A. F., ALS, F. R. N. F. F. & CONSORTIUM, I. 2012. Frequency of the C9orf72 hexanucleotide repeat expansion in patients with amyotrophic lateral sclerosis and frontotemporal dementia: a cross-sectional study. *Lancet Neurology*, 11, 323-330.
- MARTINEAU, E., DI POLO, A., VANDE VELDE, C. & ROBITAILLE, R. 2018. Dynamic neuromuscular remodeling precedes motor-unit loss in a mouse model of ALS. *Elife*, 7.
- MATSUYAMA, K., KOBAYASHI, S. & AOKI, M. 2006. Projection patterns of lamina VIII commissural neurons in the lumbar spinal cord of the adult cat: an anterograde neural tracing study. *Neuroscience*, 140, 203-18.
- MATTHEWS, P. B. 1981. Evolving views on the internal operation and functional role of the muscle spindle. *J Physiol*, 320, 1-30.

- MCCOMAS, A. J., FAWCETT, P. R. W., CAMPBELL, M. J. & SICA, R. E. P. 1971. Electrophysiological Estimation of Number of Motor Units within a Human Muscle. *Journal of Neurology Neurosurgery and Psychiatry*, 34, 121-&.
- MCKIERNAN, B. J., MARCARIO, J. K., KARRER, J. H. & CHENEY, P. D. 1998. Corticomotoneuronal postspike effects in shoulder, elbow, wrist, digit, and intrinsic hand muscles during a reach and prehension task. *Journal of Neurophysiology*, 80, 1961-1980.
- MENON, P., GEEVASINGA, N., YIANNIKAS, C., HOWELL, J., KIERNAN, M. C. & VUTIC, S. 2015. Sensitivity and specificity of threshold tracking transcranial magnetic stimulation for diagnosis of amyotrophic lateral sclerosis: a prospective study. *Lancet Neurology*, 14, 478-484.
- MEYER, K., FERRAIUOLO, L., SCHMELZER, L., BRAUN, L., MCGOVERN, V., LIKHTE, S., MICHELS, O., GOVONI, A., FITZGERALD, J., MORALES, P., FOUST, K. D., MENDELL, J. R., BURGHEES, A. H. M. & KASPAR, B. K. 2015. Improving Single Injection CSF Delivery of AAV9-mediated Gene Therapy for SMA: A Dose-response Study in Mice and Nonhuman Primates. *Molecular Therapy*, 23, 477-487.
- MILLER, R. G., MITCHELL, J. D., LYON, M. & MOORE, D. H. 2007. Riluzole for amyotrophic lateral sclerosis (ALS)/motor neuron disease (MND). *Cochrane Database Syst Rev*, CD001447.
- MITCHELL, D. G., BURK, D. L., VINITSKI, S. & RIFKIN, M. D. 1987. The Biophysical Basis of Tissue Contrast in Extracranial Mr Imaging. *American Journal of Roentgenology*, 149, 831-837.
- MOGK, J. P. M. & KEIR, P. J. 2003. The effects of posture on forearm muscle loading during gripping. *Ergonomics*, 46, 956-975.
- MORENO-GARCIA, A., KUN, A., CALERO, O., MEDINA, M. & CALERO, M. 2018. An Overview of the Role of Lipofuscin in Age-Related Neurodegeneration. *Frontiers in Neuroscience*, 12.
- MORITANI, T. & MURO, M. 1987. Motor unit activity and surface electromyogram power spectrum during increasing force of contraction. *Eur J Appl Physiol Occup Physiol*, 56, 260-5.
- NAKAJIMA, K., MAIER, M. A., KIRKWOOD, P. A. & LEMON, R. N. 2000. Striking differences in transmission of corticospinal excitation to upper limb motoneurons in two primate species. *J Neurophysiol*, 84, 698-709.
- NANDEDKAR, S. D., BARKHAUS, P. E. & STALBERG, E. V. 2010. Motor Unit Number Index (Munix): Principle, Method, and Findings in Healthy Subjects and in Patients with Motor Neuron Disease. *Muscle & Nerve*, 42, 798-807.
- NANDEDKAR, S. D., BARKHAUS, P. E. & STALBERG, E. V. 2011. Reproducibility of Munix in Patients with Amyotrophic Lateral Sclerosis. *Muscle & Nerve*, 44, 919-922.
- NANDEDKAR, S. D., NANDEDKAR, D. S., BARKHAUS, P. E. & STALBERG, E. V. 2004. Motor unit number index (MUNIX). *Ieee Transactions on Biomedical Engineering*, 51, 2209-2211.
- NARICI, M. V., HOPPELER, H., KAYSER, B., LANDONI, L., CLAASSEN, H., GAVARDI, C., CONTI, M. & CERRETELLI, P. 1996. Human quadriceps cross-sectional area, torque and neural activation during 6 months strength training. *Acta Physiologica Scandinavica*, 157, 175-186.

- NEGRO, F., MUCELI, S., CASTRONOVO, A. M., HOLOBAR, A. & FARINA, D. 2016. Multi-channel intramuscular and surface EMG decomposition by convolutive blind source separation. *Journal of Neural Engineering*, 13.
- NEUMANN, M., KWONG, L. K., LEE, E. B., KREMMER, E., FLATLEY, A., XU, Y., FORMAN, M. S., TROOST, D., KRETZSCHMAR, H. A., TROJANOWSKI, J. Q. & LEE, V. M. 2009. Phosphorylation of S409/410 of TDP-43 is a consistent feature in all sporadic and familial forms of TDP-43 proteinopathies. *Acta Neuropathol*, 117, 137-49.
- NEUMANN, M., SAMPATHU, D. M., KWONG, L. K., TRUAX, A. C., MICSENYI, M. C., CHOU, T. T., BRUCE, J., SCHUCK, T., GROSSMAN, M., CLARK, C. M., MCCLUSKEY, L. F., MILLER, B. L., MASLIAH, E., MACKENZIE, I. R., FELDMAN, H., FEIDEN, W., KRETZSCHMAR, H. A., TROJANOWSKI, J. Q. & LEE, V. M. 2006. Ubiquitinated TDP-43 in frontotemporal lobar degeneration and amyotrophic lateral sclerosis. *Science*, 314, 130-3.
- NEUWIRTH, C., BARKHAUS, P. E., BURKHARDT, C., CASTRO, J., CZELL, D., DE CARVALHO, M., NANDEDKAR, S., STALBERG, E. & WEBER, M. 2015. Tracking motor neuron loss in a set of six muscles in amyotrophic lateral sclerosis using the Motor Unit Number Index (MUNIX): a 15-month longitudinal multicentre trial. *Journal of Neurology Neurosurgery and Psychiatry*, 86, 1172-1179.
- NEUWIRTH, C., NANDEDKAR, S., STALBERG, E., BARKHAUS, P. E., DE CARVALHO, M., FURTULA, J., VAN DIJK, J. P., BALDINGER, R., CASTRO, J., COSTA, J., OTTO, M., SANDBERG, A. & WEBER, M. 2011. Motor Unit Number Index (MUNIX): A novel neurophysiological marker for neuromuscular disorders; test-retest reliability in healthy volunteers. *Clinical Neurophysiology*, 122, 1867-1872.
- NIJSSEN, J., COMLEY, L. H. & HEDLUND, E. 2017. Motor neuron vulnerability and resistance in amyotrophic lateral sclerosis. *Acta Neuropathologica*, 133, 863-885.
- NONAKA, T., MASUDA-SUZUKAKE, M., ARAI, T., HASEGAWA, Y., AKATSU, H., OBI, T., YOSHIDA, M., MURAYAMA, S., MANN, D. M., AKIYAMA, H. & HASEGAWA, M. 2013. Prion-like properties of pathological TDP-43 aggregates from diseased brains. *Cell Rep*, 4, 124-34.
- NORRIS, D. G. 2007. Selective parity RARE imaging. *Magnetic Resonance in Medicine*, 58, 643-649.
- NUDO, R. J. & MASTERTON, R. B. 1988. Descending pathways to the spinal cord: a comparative study of 22 mammals. *J Comp Neurol*, 277, 53-79.
- O'BRIEN, J., HAYDER, H. & PENG, C. 2016. Automated Quantification and Analysis of Cell Counting Procedures Using ImageJ Plugins. *Jove-Journal of Visualized Experiments*.
- OYANAGI, K., IKUTA, F. & HORIKAWA, Y. 1989. Evidence for sequential degeneration of the neurons in the intermediate zone of the spinal cord in amyotrophic lateral sclerosis: a topographic and quantitative investigation. *Acta Neuropathol*, 77, 343-9.
- OZDINLER, P. H., BENN, S., YAMAMOTO, T. H., GUZEL, M., BROWN, R. H., JR. & MACKLIS, J. D. 2011. Corticospinal motor neurons and related subcerebral projection neurons undergo early and specific neurodegeneration in hSOD1G(9)(3)A transgenic ALS mice. *J Neurosci*, 31, 4166-77.
- PALMER, E. & ASHBY, P. 1992. Corticospinal projections to upper limb motoneurons in humans. *J Physiol*, 448, 397-412.

- PARK, J., WICKI, J., KNOBLAUGH, S. E., CHAMBERLAIN, J. S. & LEE, D. 2015. Multi-Parametric MRI at 14T for Muscular Dystrophy Mice Treated with AAV Vector-Mediated Gene Therapy. *Plos One*, 10.
- PARK, M. C., BELHAJ-SAIF, A. & CHENEY, P. D. 2004. Properties of primary motor cortex output to forelimb muscles in rhesus macaques. *Journal of Neurophysiology*, 92, 2968-2984.
- PENG, Y., HE, J. B., YAO, B., LI, S., ZHOU, P. & ZHANG, Y. C. 2016. Motor unit number estimation based on high-density surface electromyography decomposition. *Clinical Neurophysiology*, 127, 3059-3065.
- PHILLIPS, C. G. & PORTER, R. 1964. The Pyramidal Projection to Motoneurons of Some Muscle Groups of the Baboon's Forelimb. *Prog Brain Res*, 12, 222-45.
- POLAK, J. F., JOLESZ, F. A. & ADAMS, D. F. 1988. Magnetic-Resonance Imaging of Skeletal-Muscle - Prolongation of T1 and T2 Subsequent to Denervation. *Investigative Radiology*, 23, 365-369.
- RAGAGNIN, A. M. G., SHADFAR, S., VIDAL, M., JAMALI, M. S. & ATKIN, J. D. 2019. Motor Neuron Susceptibility in ALS/FTD. *Front Neurosci*, 13, 532.
- RATHELOT, J. A. & STRICK, P. L. 2006. Muscle representation in the macaque motor cortex: An anatomical perspective. *Proceedings of the National Academy of Sciences of the United States of America*, 103, 8257-8262.
- RATHELOT, J. A. & STRICK, P. L. 2009. Subdivisions of primary motor cortex based on cortico-motoneuronal cells. *Proceedings of the National Academy of Sciences of the United States of America*, 106, 918-923.
- RAVITS, J. M. & LA SPADA, A. R. 2009. ALS motor phenotype heterogeneity, focality, and spread: deconstructing motor neuron degeneration. *Neurology*, 73, 805-11.
- RENTON, A. E., CHIO, A. & TRAYNOR, B. J. 2014. State of play in amyotrophic lateral sclerosis genetics. *Nat Neurosci*, 17, 17-23.
- RENTON, A. E., MAJOUNIE, E., WAITE, A., SIMON-SANCHEZ, J., ROLLINSON, S., GIBBS, J. R., SCHYMICK, J. C., LAAKSOVIRTA, H., VAN SWIETEN, J. C., MYLLYKANGAS, L., KALIMO, H., PAETAU, A., ABRAMZON, Y., REMES, A. M., KAGANOVICH, A., SCHOLZ, S. W., DUCKWORTH, J., DING, J. H., HARMER, D. W., HERNANDEZ, D. G., JOHNSON, J. O., MOK, K., RYTEN, M., TRABZUNI, D., GUERREIRO, R. J., ORRELL, R. W., NEAL, J., MURRAY, A., PEARSON, J., JANSEN, I. E., SONDERVAN, D., SEELAAR, H., BLAKE, D., YOUNG, K., HALLIWELL, N., CALLISTER, J. B., TOULSON, G., RICHARDSON, A., GERHARD, A., SNOWDEN, J., MANN, D., NEARY, D., NALLS, M. A., PEURALINNA, T., JANSSON, L., ISOVIITA, V. M., KAIVORINNE, A. L., HOLTTA-VUORI, M., IKONEN, E., SULKAVA, R., BENATAR, M., WUU, J., CHIO, A., RESTAGNO, G., BORGHERO, G., SABATELLI, M., HECKERMAN, D., ROGAEVA, E., ZINMAN, L., ROTHSTEIN, J. D., SENDTNER, M., DREPPER, C., EICHLER, E. E., ALKAN, C., ABDULLAEV, Z., PACK, S. D., DUTRA, A., PAK, E., HARDY, J., SINGLETON, A., WILLIAMS, N. M., HEUTINK, P., PICKERING-BROWN, S., MORRIS, H. R., TIENARI, P. J., TRAYNOR, B. J. & CONSORTIUM, I. 2011. A Hexanucleotide Repeat Expansion in C9ORF72 Is the Cause of Chromosome 9p21-Linked ALS-FTD. *Neuron*, 72, 257-268.
- RIVARA, C. B., SHERWOOD, C. C., BOURAS, C. & HOF, P. R. 2003. Stereologic characterization and spatial distribution patterns of Betz cells in the human primary motor cortex. *Anatomical Record Part a-Discoveries in Molecular Cellular and Evolutionary Biology*, 270a, 137-151.

- ROCCATAGLIATA, L., BONZANO, L., MANCARDI, G., CANEPA, C. & CAPONNETTO, C. 2009. Detection of motor cortex thinning and corticospinal tract involvement by quantitative MRI in amyotrophic lateral sclerosis. *Amyotrophic Lateral Sclerosis*, 10, 47-52.
- ROMAN-LIU, D. & BARTUZI, P. 2013. The influence of wrist posture on the time and frequency EMG signal measures of forearm muscles. *Gait & Posture*, 37, 340-344.
- ROSEN, D. R., SIDDIQUE, T., PATTERSON, D., FIGLEWICZ, D. A., SAPP, P., HENTATI, A., DONALDSON, D., GOTO, J., OREGAN, J. P., DENG, H. X., RAHMANI, Z., KRIZUS, A., MCKENNAYASEK, D., CAYABYAB, A., GASTON, S. M., BERGER, R., TANZI, R. E., HALPERIN, J. J., HERZFELDT, B., VANDENBERGH, R., HUNG, W. Y., BIRD, T., DENG, G., MULDER, D. W., SMYTH, C., LAING, N. G., SORIANO, E., PERICAKVANCE, M. A., HAINES, J., ROULEAU, G. A., GUSELLA, J. S., HORVITZ, H. R. & BROWN, R. H. 1993. Mutations in Cu/Zn Superoxide-Dismutase Gene Are Associated with Familial Amyotrophic-Lateral-Sclerosis. *Nature*, 362, 59-62.
- ROWLAND, L. P. & SHNEIDER, N. A. 2001. Amyotrophic lateral sclerosis. *N Engl J Med*, 344, 1688-700.
- SALEGIO, E. A., SAMARANCH, L., KELLS, A. P., MITTERMAYER, G., SAN SEBASTIAN, W., ZHOU, S., BEYER, J., FORSAYETH, J. & BANKIEWICZ, K. S. 2013. Axonal transport of adeno-associated viral vectors is serotype-dependent. *Gene Therapy*, 20, 348-352.
- SAMARANCH, L., SALEGIO, E. A., SAN SEBASTIAN, W., KELLS, A. P., FOUST, K. D., BRINGAS, J. R., LAMARRE, C., FORSAYETH, J., KASPAR, B. K. & BANKIEWICZ, K. S. 2012. Adeno-associated virus serotype 9 transduction in the central nervous system of nonhuman primates. *Hum Gene Ther*, 23, 382-9.
- SAN SEBASTIAN, W., SAMARANCH, L., HELLER, G., KELLS, A. P., BRINGAS, J., PIVIROTTI, P., FORSAYETH, J. & BANKIEWICZ, K. S. 2013. Adeno-associated virus type 6 is retrogradely transported in the non-human primate brain. *Gene Therapy*, 20, 1178-1183.
- SAUNDERS, A., JOHNSON, C. A. & SABATINI, B. L. 2012. Novel recombinant adeno-associated viruses for Cre activated and inactivated transgene expression in neurons. *Front Neural Circuits*, 6, 47.
- SCHMIDLIN, E., KAESER, M., GINDRAT, A. D., SAVIDAN, J., CHATAGNY, P., BADOUD, S., HAMADJIDA, A., BEAUD, M. L., WANNIER, T., BELHAJ-SAIF, A. & ROUILLER, E. M. 2011. Behavioral assessment of manual dexterity in non-human primates. *J Vis Exp*.
- SCHNELL, S. A., STAINES, W. A. & WESSENDORF, M. W. 1999. Reduction of lipofuscin-like autofluorescence in fluorescently labeled tissue. *Journal of Histochemistry & Cytochemistry*, 47, 719-730.
- SHAW, C. E., ENAYAT, Z. E., POWELL, J. F., ANDERSON, V. E. R., RADUNOVIC, A., AL-SARRAJ, S. & LEIGH, P. N. 1997. Familial amyotrophic lateral sclerosis - Molecular pathology of a patient with a SOD1 mutation. *Neurology*, 49, 1612-1616.
- SHEFNER, J. M., AL-CHALABI, A., BAKER, M. R., CUI, L. Y., DE CARVALHO, M., EISEN, A., GROSSKREUTZ, J., HARDIMAN, O., HENDERSON, R., MATAMALA, J. M., MITSUMOTO, H., PAULUS, W., SIMON, N., SWASH, M., TALBOT, K., TURNER, M. R., UGAWA, Y., VAN DEN BERG, L. H., VERDUGO, R., VUCIC, S., KAJI, R., BURKE, D. & KIERNAN, M. C. 2020. A proposal for new diagnostic criteria for ALS. *Clin Neurophysiol*, 131, 1975-1978.

- SHEFNER, J. M., CUDKOWICZ, M. & BROWN, R. H. 2006. Motor unit number estimation predicts disease onset and survival in a transgenic mouse model of amyotrophic lateral sclerosis. *Muscle & Nerve*, 34, 603-607.
- SHEFNER, J. M., REAUME, A. G., FLOOD, D. G., SCOTT, R. W., KOWALL, N. W., FERRANTE, R. J., SIWEK, D. F., UPTON-RICE, M. & BROWN, R. H. 1999. Mice lacking cytosolic copper/zinc superoxide dismutase display a distinctive motor axonopathy. *Neurology*, 53, 1239-1246.
- SHNEIDER, N. A., BROWN, M. N., SMITH, C. A., PICKEL, J. & ALVAREZ, F. J. 2009. Gamma motor neurons express distinct genetic markers at birth and require muscle spindle-derived GDNF for postnatal survival. *Neural Dev*, 4, 42.
- SONG, S., SCOTT-JORGENSEN, M., WANG, J., POIRIER, A., CRAWFORD, J., CAMPBELL-THOMPSON, M. & FLOTTE, T. R. 2002. Intramuscular administration of recombinant adeno-associated virus 2 alpha-1 antitrypsin (rAAV-SERPINA1) vectors in a nonhuman primate model: safety and immunologic aspects. *Mol Ther*, 6, 329-35.
- SPILLER, K. J., CHEUNG, C. J., RESTREPO, C. R., KWONG, L. K., STIEBER, A. M., TROJANOWSKI, J. Q. & LEE, V. M. 2016. Selective Motor Neuron Resistance and Recovery in a New Inducible Mouse Model of TDP-43 Proteinopathy. *J Neurosci*, 36, 7707-17.
- SREEDHARAN, J., BLAIR, I. P., TRIPATHI, V. B., HU, X., VANCE, C., ROGELJ, B., ACKERLEY, S., DURRALL, J. C., WILLIAMS, K. L., BURATTI, E., BARALLE, F., DE BELLEROCHE, J., MITCHELL, J. D., LEIGH, P. N., AL-CHALABI, A., MILLER, C. C., NICHOLSON, G. & SHAW, C. E. 2008. TDP-43 mutations in familial and sporadic amyotrophic lateral sclerosis. *Science*, 319, 1668-1672.
- STEPHENS, B., GUILOFF, R. J., NAVARRETE, R., NEWMAN, P., NIKHAR, N. & LEWIS, P. 2006. Widespread loss of neuronal populations in the spinal ventral horn in sporadic motor neuron disease. A morphometric study. *Journal of the Neurological Sciences*, 244, 41-58.
- STRONG, M. J., ABRAHAMS, S., GOLDSTEIN, L. H., WOOLLEY, S., MCLAUGHLIN, P., SNOWDEN, J., MIOSHI, E., ROBERTS-SOUTH, A., BENATAR, M., HORTOBAGYI, T., ROSENFELD, J., SILANI, V., INCE, P. G. & TURNER, M. R. 2017. Amyotrophic lateral sclerosis - frontotemporal spectrum disorder (ALS-FTSD): Revised diagnostic criteria. *Amyotrophic Lateral Sclerosis and Frontotemporal Degeneration*, 18, 153-174.
- TERVO, D. G. R., HWANG, B. Y., VISWANATHAN, S., GAJ, T., LAVZIN, M., RITOLA, K. D., LINDO, S., MICHAEL, S., KULESHOVA, E., OJALA, D., HUANG, C. C., GERFEN, C. R., SCHILLER, J., DUDMAN, J. T., HANTMAN, A. W., LOOGER, L. L., SCHAFFER, D. V. & KARPOVA, A. Y. 2016. A Designer AAV Variant Permits Efficient Retrograde Access to Projection Neurons. *Neuron*, 92, 372-382.
- TOHYAMA, T., KINOSHITA, M., KOBAYASHI, K., ISA, K., WATANABE, D., KOBAYASHI, K., LIU, M. G. & ISA, T. 2017. Contribution of propriospinal neurons to recovery of hand dexterity after corticospinal tract lesions in monkeys. *Proceedings of the National Academy of Sciences of the United States of America*, 114, 604-609.
- TOROMANOFF, A., CHEREL, Y., GUILBAUD, M., PENAUD-BUDLOO, M., SNYDER, R. O., HASKINS, M. E., DESCHAMPS, J. Y., GUIGAND, L., PODEVIN, G., ARRUDA, V. R., HIGH, K. A., STEDMAN, H. H., ROLLING, F., ANEGON, I., MOULLIER, P. & LE GUINER, C. 2008. Safety and Efficacy of Regional Intravenous (RI) Versus

- Intramuscular (IM) Delivery of rAAV1 and rAAV8 to Nonhuman Primate Skeletal Muscle. *Mol Ther*, 16, 1291-1299.
- TOSOLINI, A. P. & MORRIS, R. 2016. Targeting Motor End Plates for Delivery of Adenoviruses: An Approach to Maximize Uptake and Transduction of Spinal Cord Motor Neurons. *Sci Rep*, 6, 33058.
- TOURNIER, J. D., SMITH, R., RAFFELT, D., TABBARA, R., DHOLLANDER, T., PIETSCH, M., CHRISTIAENS, D., JEURISSEN, B., YEH, C. H. & CONNELLY, A. 2019. MRtrix3: A fast, flexible and open software framework for medical image processing and visualisation. *Neuroimage*, 202.
- TOWNE, C., SCHNEIDER, B. L., KIERAN, D., REDMOND, D. E., JR. & AEBISCHER, P. 2010. Efficient transduction of non-human primate motor neurons after intramuscular delivery of recombinant AAV serotype 6. *Gene Ther*, 17, 141-6.
- TSUGAWA, J., DHARMADASA, T., MA, Y., HUYNH, W., VUCIC, S. & KIERNAN, M. C. 2018. Fasciculation intensity and disease progression in amyotrophic lateral sclerosis. *Clinical Neurophysiology*, 129, 2149-2154.
- UCHIDA, A., SASAGURI, H., KIMURA, N., TAJIRI, M., OHKUBO, T., ONO, F., SAKAUE, F., KANAI, K., HIRAI, T., SANO, T., SHIBUYA, K., KOBAYASHI, M., YAMAMOTO, M., YOKOTA, S., KUBODERA, T., TOMORI, M., SAKAKI, K., ENOMOTO, M., HIRAI, Y., KUMAGAI, J., YASUTOMI, Y., MOCHIZUKI, H., KUWABARA, S., UCHIHARA, T., MIZUSAWA, H. & YOKOTA, T. 2012. Non-human primate model of amyotrophic lateral sclerosis with cytoplasmic mislocalization of TDP-43. *Brain*, 135, 833-46.
- VAN DIJK, J. P., BLOK, J. H., LAPATKI, B. G., VAN SCHAİK, I. N., ZWARTS, M. J. & STEGEMAN, D. F. 2008. Motor unit number estimation using high-density surface electromyography. *Clinical Neurophysiology*, 119, 33-42.
- VANCE, C., ROGELJ, B., HORTOBAGYI, T., DE VOS, K. J., NISHIMURA, A. L., SREEDHARAN, J., HU, X., SMITH, B., RUDDY, D., WRIGHT, P., GANESALINGAM, J., WILLIAMS, K. L., TRIPATHI, V., AL-SARAJ, S., AL-CHALABI, A., LEIGH, P. N., BLAIR, I. P., NICHOLSON, G., DE BELLEROCHE, J., GALLO, J. M., MILLER, C. C. & SHAW, C. E. 2009. Mutations in FUS, an RNA Processing Protein, Cause Familial Amyotrophic Lateral Sclerosis Type 6. *Science*, 323, 1208-1211.
- VIDDELEER, A. R., SIJENS, P. E., VAN OOIJEN, P. M., KUYPERS, P. D., HOVIUS, S. E., DE DEYN, P. P. & OUDKERK, M. 2016. Quantitative STIR of muscle for monitoring nerve regeneration. *J Magn Reson Imaging*, 44, 401-10.
- VIGANO, L., FORNIA, L., ROSSI, M., HOWELLS, H., LEONETTI, A., PUGLISI, G., NIBALI, M. C., BELLACICCA, A., GRIMALDI, M., BELLO, L. & CERRI, G. 2019. Anatomic-functional characterisation of the human "hand-knob": A direct electrophysiological study. *Cortex*, 113, 239-254.
- VUCIC, S. 2019. Split elbow sign: more evidence for the importance of cortical dysfunction in ALS. *J Neurol Neurosurg Psychiatry*, 90, 729.
- VUCIC, S., ZIEMANN, U., EISEN, A., HALLETT, M. & KIERNAN, M. C. 2013. Transcranial magnetic stimulation and amyotrophic lateral sclerosis: pathophysiological insights. *Journal of Neurology Neurosurgery and Psychiatry*, 84, 1161-1170.
- WANG, D. B., DAYTON, R. D., HENNING, P. P., CAIN, C. D., ZHAO, L. R., SCHROTT, L. M., ORCHARD, E. A., KNIGHT, D. S. & KLEIN, R. L. 2010. Expansive Gene Transfer in the Rat CNS Rapidly Produces Amyotrophic Lateral Sclerosis Relevant Sequelae When TDP-43 is Overexpressed. *Molecular Therapy*, 18, 2064-2074.

- WEBER, M., EISEN, A., STEWART, H. & HIROTA, N. 2000. The split hand in ALS has a cortical basis. *Journal of the Neurological Sciences*, 180, 66-70.
- WEGORZEWSKA, I., BELL, S., CAIRNS, N. J., MILLER, T. M. & BALOH, R. H. 2009. TDP-43 mutant transgenic mice develop features of ALS and frontotemporal lobar degeneration. *Proceedings of the National Academy of Sciences of the United States of America*, 106, 18809-18814.
- WESSIG, C., KOLTZENBURG, M., REINERS, K., SOLYMOSI, L. & BENDSZUS, M. 2004. Muscle magnetic resonance imaging of denervation and reinnervation: correlation with electrophysiology and histology. *Exp Neurol*, 185, 254-61.
- WEST, G. A., HAYNOR, D. R., GOODKIN, R., TSURUDA, J. S., BRONSTEIN, A. D., KRAFT, G., WINTER, T. & KLIOT, M. 1994. Magnetic-Resonance-Imaging Signal Changes in Denervated Muscles after Peripheral-Nerve Injury. *Neurosurgery*, 35, 1077-1085.
- WIDENER, G. L. & CHENEY, P. D. 1997. Effects on muscle activity from microstimuli applied to somatosensory and motor cortex during voluntary movement in the monkey. *Journal of Neurophysiology*, 77, 2446-2465.
- WILBOURN, A. J. 2000. The "split hand syndrome". *Muscle Nerve*, 23, 138.
- WILS, H., KLEINBERGER, G., JANSSENS, J., PERESON, S., JORIS, G., CUIJT, I., SMITS, V., CEUTERICK-DE GROOTE, C., VAN BROECKHOVEN, C. & KUMAR-SINGH, S. 2010. TDP-43 transgenic mice develop spastic paralysis and neuronal inclusions characteristic of ALS and frontotemporal lobar degeneration. *Proceedings of the National Academy of Sciences of the United States of America*, 107, 3858-3863.
- WITHAM, C. L., FISHER, K. M., EDGLEY, S. A. & BAKER, S. N. 2016. Corticospinal Inputs to Primate Motoneurons Innervating the Forelimb from Two Divisions of Primary Motor Cortex and Area 3a. *Journal of Neuroscience*, 36, 2605-2616.
- XU, Y. F., GENDRON, T. F., ZHANG, Y. J., LIN, W. L., D'ALTON, S., SHENG, H., CASEY, M. C., TONG, J. M., KNIGHT, J., YU, X., RADEMAKERS, R., BOYLAN, K., HUTTON, M., MCGOWAN, E., DICKSON, D. W., LEWIS, J. & PETRUCELLI, L. 2010. Wild-Type Human TDP-43 Expression Causes TDP-43 Phosphorylation, Mitochondrial Aggregation, Motor Deficits, and Early Mortality in Transgenic Mice. *Journal of Neuroscience*, 30, 10851-10859.
- YANG, B., WENDLAND, M. F. & O'CONNELL, G. D. 2020. Direct Quantification of Intervertebral Disc Water Content Using MRI. *Journal of Magnetic Resonance Imaging*, 52, 1152-1162.
- YANG, S. B., HU, S. Y., LI, B. G. & LI, X. M. 2017. Localization of nerve entry point and intramuscular nerve-dense regions as targets to block brachioradialis muscle spasticity. *International Journal of Clinical and Experimental Medicine*, 10, 11912-11920.
- YOKOSEKI, A., SHIGA, A., TAN, C. F., TAGAWA, A., KANEKO, H., KOYAMA, A., EGUCHI, H., TSUJINO, A., IKEUCHI, T., KAKITA, A., OKAMOTO, K., NISHIZAVA, M., TAKAHASHI, H. & ONODERA, O. 2008. TDP-43 mutation in familial amyotrophic lateral sclerosis. *Annals of Neurology*, 63, 538-542.